1-1-2017

Nanostructured Lithium Iron Silicate/carbon Composites As Cathode Material For Next Generation Of Lithium-Ion Batteries

Ajay Kumar
Wayne State University,

NANOSTRUCTURED LITHIUM IRON SILICATE/CARBON COMPOSITES AS CATHODE MATERIAL FOR NEXT GENERATION OF LITHIUM-ION BATTERIES

by

AJAY KUMAR

DISSERTATION

Submitted to the Graduate School

of Wayne State University,

Detroit, Michigan

in partial fulfilment of the requirements

for the degree of

DOCTOR OF PHILOSOPHY

2017

MAJOR: PHYSICS

Approved By:

…….

Advisor Date

…….……...……..

…….

…….

…….

DEDICATION

“To my loving family for their continuous support, unconditional love and care”

ACKNOWLEGEMENTS

It gives me immense pleasure to thank my advisor Dr. Ratna Naik for her guidance, supervision, encouragement, and continuous support throughout my research period leading to Ph.D degree. In addition to research, she was always with me in my good and bad times and I learned a great deal about life from her. I hope that I would be as enthusiastic and energetic as Dr. Naik. I consider myself very fortunate to have her as my advisor and this research work would not have been possible without her guidance and support. I would like to thank Dr. Gholam Abbas Nazri for his colossal help in experiment design, teaching the physics and chemistry of lithium ion batteries and other energy storage systems. I would like to take this opportunity to thank Dr. O.D. Jayakumar at Bhabha atomic research centre in India, who visited Wayne State University in 2014 and spent couple of months with us in lab. I learned many useful material synthesis techniques from him and he helped me in various aspects of experimental and data analysis. I am very grateful for his collaboration and this work would not have been possible to complete without his help.

I would like to thank Dr. Vaman M. Naik for his generous time, meaningful discussions, invaluable advice, support, helping me to learn the Rietveld analysis of XRD data and Mathcad program and also for serving as my committee member. I would like to thank Dr. Zhixian Zhou and Dr. Simon Ng for serving as committee member. My sincere thanks go to former and present labmates; Dr. Balaji Mandal, Dr. Kulwinder S. Dhindsa, Dr. Khadije Bazzi, Dr. Mariam Nazri, Wissam Fawaz, Dr. Prasad T. Rao, and Parisa Bashiri for their assistance in lab. I would like to thank Da Li from Dr. Brock's group (Chemistry Department) for giving me access to BET surface area measurement instrument and helping me to use it. I received a remarkable amount of co-operation from him.

Additionally, I greatly appreciate the professors at Wayne State University and other institute I attended for strengthening my knowledge in area of Physics, Material Science and Renewable Energy. I also thank the professors with whom I taught Quiz sections for their useful discussions and advice. I am thankful to Dr. Payson for helping in the lab setup and providing a friendly work environment during my time as a teaching assistant. I also thank Dr. Jogindra Wadehra for advising me on all the paper work related to graduate school throughout the Ph.D Program from the beginning of my first day at Wayne State University.

Ph.D is a long journey with challenges and wonderful learning opportunities and it is very difficult to survive without a good social support system. I would like to thank Dr. Suvra laha, Dr. Maheshika Arachcheige, Dr. Ehab Abdelhamid, Dr. Rupam Mukherjee, Dr. Humeshkar Nemala, Dr. Prabhat Pujahari, Dr. sidharth Prasand, Dr. Sumit Basu, Amit kumar, Joydeep Roy and including my labmates for their support and social interaction within and outside the department. However, the list is long and impossible to mention it here. I would like to thank everyone who have helped me directly/indirectly in achieving my goal.

I would like to give a very especial thank to Dr. Vivek K. Malik (Assistant Professor, IIT Roorkee) and Dr. Pramod Kumar (Universite d'Evry-Val d'Essonne, France) for their financial help in paying first semester tuition fees and having confidence in my abilities. I would not have continued Ph.D. program without their help. I also thank my friend Dr. Pradeep Kumar and Dr. Ambesh Dixit for suggesting me this group to pursue my Ph.D. at Wayne State University. I also thank Pradeep for his continuous moral support, help and care in every way during the initial period of my Ph.D program. I would like to thank my friends form IIT Rookee for their unconditional support and they have stood by in good and bad times. I feel lucky to have such good friends around me.

I am very thankful to my parents, in-laws, younger sister and brothers for their unconditional love and support throughout the years of my study. The final words of appreciations go to my wife Pratibha for taking my side in ups and downs in life. I am grateful to GOD who gifted us with a little princess, my daughter Anaya, a source of bundle of love and joy. I forget every tension/stress of life when I see her smiling face.

TABLE OF CONTENTS

Dedication……...ii

Acknowledgements……iii

List of Tables……..x

List of Figures……xi

Chapter 1: Lithium ion batteries-Introduction and background…….1

1.1 Energy storage and batteries…….…….1

1.2 Lithium ion batteries: operation principle……..4

1.3 Components of Lithium ion batteries…..……..7

1.3.1 Anode……...……...7

1.3.2 Electrolyte……9

1.3.3 Separator……11

1.3.4 Cathode……..11

1.4 Types of cathode materials…..……...……..12

1.4.1 Layered oxide materials……..……...……...…….....13

1.4.2 Spinel oxide materials...…….14

1.4.3 Polyanion materials....……16

1.4.3.1 Phosphates……..…….……..17

1.4.3.2 Silicates…….....…….…….……..18

1.5 Crystal structure and phase stabilities of silicates……20

1.6 Methods for enhancing the electrochemical performance of Li_2FeSiO_4…….……21

1.6.1 Carbon coating……...22

1.6.2 Nano-engineering of particles……23

1.6.3 Metal doping/lattice engineering……...24

1.7 Motivation and scope of thesis……26

Chapter 2: Synthesis and characterization Techniques……..28

2.1 Synthesis of silicates……28

2.1.1 Sol-gel method……...29

2.1.2 Hydrothermal/solvothermal method……..29

2.2 Structural and surface characterization techniques…….30

2.2.1 X-ray diffraction (XRD)……30

2.2.2 Rietveld Refinement……..32

2.2.3 Electrical conductivity measurement…….34

2.2.4 Scanning electron microscope (SEM)……...34

2.2.5 Energy dispersive X-ray analysis (EDXA)-Elemental composition…….36

2.2.6 Transmission electron Microscope (TEM)……36

2.2.7 X-ray photoelectron spectroscopy (XPS)……..37

2.2.8 Surface area and porosimetry……..38

2.3 Electrochemical Characterizations……...40

2.3.1 Electrode and coin cell fabrication……40

2.3.2 Electrochemical impedance spectroscopy (EIS)……42

2.3.3 Cyclic voltammetry (CV)……..44

2.3.4 Galvanostatic charge/discharge…….46

Chapter 3: Improved electrochemical properties of solvothermally synthesized Li_2FeSiO_4/C nanocomposites: a comparison between solvothermal and sol-gel methods…….47

3.1 Introduction……..47

3.2 Materials and methods…….49

3.3 Results and discussions……50

3.3.1 Structural analysis (XRD)……..50

3.3.2 Carbon determination and conductivity measurements…….51

3.3.3 Morphology and microstructure……51

3.3.4 Specific surface area and pore-size……52

3.4 Electrochemical measurements……53

3.4.1 Galvanostatic charge/discharge…….53

3.4.2 Cyclic voltammetry……56

3.4.3 Electrochemical impedance spectroscopy…….58

3.5 Conclusions……..60

Chapter 4: Mg doped Li_2FeSiO_4/C nano-composites synthesized by solvothermal method for lithium ion batteries……...61

4.1 Introduction……..61

4.2 Material synthesis……62

4.3 Results and discussions……63

4.3.1 XRD analysis and carbon determination……..…….....63

4.3.2 XPS analysis and conductivity measurement……..……...……65

4.3.3 Morphology and microstructure……..……...……67

4.3.4 Surface area and porosity…..……...……...69

4.4 Electrochemical measurements……69

4.4.1 Galvanostatic charge/discharge……...……..69

4.4.2 Cyclic voltammetry……...……..……...……....72

4.4.3 Electrochemical impedance spectroscopy……...……..…...…….73

4.5 Conclusions……..76

Chapter 5: Improved electrochemical performance of Li_2FeSiO_4/CNF/rGO nano composite for advanced lithium ion batteries……...77

5.1 Introduction……..77

5.2 Material synthesis……79

5.2.1 Reduction of GO...……...……..……....79

5.2.2 Li_2FeSiO_4/CNF/rGO synthesis...……..……...……..79

5.3 Results and discussions……80

5.3.1 Structural analysis (XRD)...……..…….80

5.3.2 Carbon determination and conductivity measurement...……..……..……..82

5.3.3 Specific surface area and pore size...…….....82

5.3.4 Morphology and microstructure...…….…….……...83

5.4 Electrochemical characterizations……...84

5.4.1 Galvanostatic charge/discharge...……..……84

5.4.2 Electrochemical impedance spectroscopy……..……...…87

5.5 Conclusions……..89

Chapter 6: Summary and future direction…..……90

6.1 Future directions……..92

Appendix Rietveld refinement procedure for GSAS…….……...…….95

References……....101

Abstract……114

Autobiographical statement…….116

LIST OF TABLES

Table 4.1 Lattice parameters of $Li_2Fe_{1-x}Mg_xSiO_4/C$ (x = 0, 0.01, 0.02, 0.04) samples……65

Table 4.2 Electrochemical impedance parameters and the exchange current density of the $Li_2Fe_{1-x}Mg_xSiO_4/C$ (x = 0, 0.01, 0.02, 0.04) samples……74

Table 5.1 Calculated lattice parameters for LFS/CNF and LFS/CNF/rGO nano-composites……82

Table 5.2 Electrochemical impedance parameters of the LFS/CNF and LFS/CNF/rGO nano-composites…..……88

LIST OF FIGURES

Figure 1.1 Specific energy density and volumetric energy density of different rechargeable battery technologies…….2

Figure 1.2 Hybrid electric vehicle (HEV) market evolution……...3

Figure 1.3 Recharging/discharging intercalation mechanisms of Li ion batteries. (Positive electrode-cathode and negative electrode-anode)……5

Figure 1.4 The relative energies of electrolytes window and electrode chemical potential with no electrode and electrolyte reaction (a) liquid electrolyte with solid electrode (anode and cathode) (b) solid electrolyte with liquid or gases reactants……...6

Figure 1.5 The schematic open circuit energy of an aqueous electrolyte system. HOMO and LUMO are highest occupied molecular orbit and lowest unoccupied molecular orbit respectively. The μ_C and μ_A are the chemical potentials for cathode and anode respectively……..7

Figure 1.6 Capacity versus potential curve of different electrode of Lithium ion batteries……..12

Figure 1.7 the crystal structure of layered $LiMO_2$ (red: Lithium ions and blue: the MO_2 slab)…13

Figure 1.8 Voltage composition curve for $LiCoO_2$……....13

Figure 1.9 The crystal structure of layered LiM_2O_4 (red: Lithium ions and blue: transition metal ion)…….15

Figure 1.10 Voltage-composition curve for layered LiM_2O4……...15

Figure 1.11 Crystal structure of polyanion cathode (yellow: transition metal ion, green: Li ion and red: X ion depending upon the P, V, etc)……16

Figure 1.12 Voltage-composition curve for Li_xFePO_4……..18

Figure 1.13 The calculated lithium de-insertion voltage at different oxidation for Li_2MSiO_4…..19

Figure 1.14 The crystal structure of Li_2FeSiO_4 polymorphs: (a) $P2_1$, (b) Pmnb, (c) $P2_1/n$, and (d) $Pmn2_1$. The color codes are as follows; Li: green, Si: gray, and Fe: brown……. ……21

Figure 1.15 Schematic showing the lithium ion and electron transport in carbon coated active electrode material with low conductivity……...22

Figure 2.1 Schematic representation of Bragg's law…….30

Figure 2.2 Geometry of X-ray diffraction machine……...32

Figure 2.3 Reitveld refinement model to minimize difference between calculated and observed pattern by least squares method…….33

Figure 2.4 Van de Pauw's Resistivity measurement…….34

Figure 2.5 Schematic diagram of electron beam interaction with material……...35

Figure 2.6 Schematic diagram of the XPS process, showing photoionization of an atom by the ejection of a 1s electron…….38

Figure 2.7 The Schematic diagram of Li ion coin cell assembly (top) and Image of the glove box (bottom)……..41

Figure 2.8 (a) Nyquist plot and (b) plot of Z' versus $\omega^{-1/2}$ in low frequency range for a coin cell of Li_2FeSiO_4/C-SG-600 sample…..43

Figure 2.9 CV plot at different scan rates for a coin cell of Li_2FeSiO_4/C-SG-600 sample. The inset shows a plot of the peak current versus square root of scan rate...……...45

Figure 3.1 XRD patterns of (a) Li_2FeSiO_4/C (Sol-gel, SG), and (b) Li_2FeSiO_4/C (Solvothermal, ST) annealed for 9 hours at different temperatures……...50

Figure 3.2 SEM images of (a) Li_2FeSiO_4/C-SG-600, (b) Li_2FeSiO_4/C-ST-600, and TEM images of (c) Li_2FeSiO_4/C-SG-600 and (d) Li_2FeSiO_4/C-ST-600 samples……...51

Figure 3.3 N_2 adsorption/desorption isotherms of Li_2FeSiO_4/C-SG-600 and Li_2FeSiO_4/C-ST-600 composites……..52

Figure 3.4 A typical charge/discharge profile of Li_2FeSiO_4/C-ST-600 at C/30 rate…….53

Figure 3.5 The second cycle of charge/discharge profiles of (a) Li_2FeSiO_4/C-ST annealed at 600 ^oC and 650 ^oC, and (b) Li_2FeSiO_4/C-SG annealed at 600 ^oC and 650 ^oC……..54

Figure 3.6 (a) The rate capability of Li_2FeSiO_4/C-ST-600 and Li_2FeSiO_4/C-SG-600 samples and (b) Stability curve of Li_2FeSiO_4/C-SG-600 and Li_2FeSiO_4/C-ST-600 samples at 1C rate……...55

Figure 3.7 I-V plots of (a) Li_2FeSiO_4/C (ST-600^{o}C-9h), (b) Li_2FeSiO_4/C (SG-600^{o}C-9h) at different scan rates, (c) A comparison of I-V plots of Li_2FeSiO_4/C-ST-600 and Li_2FeSiO_4/C-SG-600 samples at 0.1 mV/s scan rate. The arrow points to the second oxidation peak corresponding to the second electron transfer, and (d) Randles-sevcik plots of the normalized peak current (I_p) as a function of square root of scan rate……57

Figure 3.8 (a) Nyquist plots and (b) graph of Z' v. $\omega^{-1/2}$ in the low frequency range for the coin cell of $Li_2FeSiO4$/C-ST-600 and Li_2FeSiO_4/C-SG-600 samples……...58

Figure 4.1 XRD patterns and Rietveld refinement profiles of (a) LFS/C, (b) 1Mg-LFS/C, (c) 2Mg- LFS/C and (d) 4Mg-LFS/C. In (a) the α-Fe_2O_3 and FeO impurity peaks marked with symbols # and *. The inset shows the enlarged region of $2\theta = 20^o$ to $2\theta = 40^o$ emphasizing the peak shifts and line narrowing upon Mg doping……...…64

Figure 4.2 XPS spectrum of (a) 1Mg-LFS/C, and (b) 1Mg-LFS/C enlarged to show Fe2p region. The inset (b) shows Mg2p peak in 1Mg-LFS/C……66

Figure 4.3 SEM images of (a) LFS/C, (b) 1Mg-LFS/C, (c) 2Mg-LFS/C, and (d) 4Mg-LFS/C…67

Figure 4.4 (a) SEM image of 1Mg-LFS/C, and its elemental mapping showing uniform distribution of (b) Fe, (c) Si, and (d) Mg……68

Figure 4.5 TEM image of (a) LFS/C, (b) 1Mg-LFS/C, and HRTEM image of (c) 1Mg-LFS/C (d) EDS spectrum of 1Mg-LFS/C, (e) TEM image of 2Mg-LFS/C and (f) TEM image of 4Mg-LFS/C and the inset shows a carbon coated particle……..68

Figure 4.6 N_2 adsorption/desorption isotherms of LFS/C, 1Mg-LFS/C, 2Mg-LFS/C and 4Mg-LFS/C. The inset shows their pore size distributions……69

Figure 4.7 Charge discharge profile of 1Mg-LFS/C (a) for the first 5 cycles, and (b) comparison of 2^{nd} cycle of charge discharge profiles of LFS/C and 1Mg-LFS/C at C/30……70

Figure 4.8 (a) Rate capability of LFS/C and Mg doped LFS/C at different rates. The inset in (a) shows the Cyclic stability curves for LFS/C and 1Mg-LFS/C at 1C and (b) Charge/discharge profiles of LFS/C and Mg doped LFS/C at C/8 rate……..71

Figure 4.9 I-V plots of LFS/C and 1Mg-LFS/C at a scan rate of 0.1 $mV.s^{-1}$……73

Figure 4.10 (a) Nyquist plots of LFS/C, 1Mg-LFS/C, 2Mg-LFS/C and 4Mg-LFS/C samples, (b) plots of Z' vs. $\omega^{-1/2}$ in the low frequency region……...74

Figure 5.1 XRD pattern of LFS/CNF and LFS/CNF/rGO nano-composites. The carbon peak in LFS/CNF and LFS/CNF/rGO is marked with asterisk…….……81

Figure 5.2 Rietveld refinement patterns of XRD data for LFS/CNF and LFS/CNF/rGO Composites…….81

Figure 5.3 N_2 adsorption/desorption isotherms of LFS/CNF and LFS/CNF/rGO. The inset shows their pore size distributions ……83

Figure 5.4 SEM images of (a) LFS/CNF, (b) LFS/rGO nano-composites, and TEM image of (c) LFS/CNF/rGO nano-composite..……...84

Figure 5.5 Charge/discharge curves of (a) LFS/CNF and (b) LFS/CNF/rGO……...85

Figure 5.6 (a) Rate capability of LFS/CNF and LFS/CNF/rGO at different rates, (b) Cyclic stability curves for LFS/CNF and LFS/CNF/rGO at 1C, Charge/discharge profiles of (c) LFS/CNF, and (d) LFS/CNF/rGO at different rates ….……86

Figure 5.7 (a) Nyquist plots and (b) graph of Z' v.$\omega^{-1/2}$ in the low frequency range for the coin cell of LFS/CNF and LFS/CNF/rGO…….87

CHAPTER 1 LITHIUM ION BATTERIES-INTRODUCTION AND BACKGROUND

1.1 Energy storage and batteries

Most of the transport vehicles are powered by fossil fuels and are the major source of CO_2 emission. Such vehicles have increased exponentially in last 50 years, and only recently we have become more aware of greenhouse emission gases' detrimental effect on health and environment [1]. In addition to carbonaceous emission, the dependence of import of crude oil makes the modern nations vulnerable, which leads to endanger the world peace [2]. The CO_2 issues and its consequent air pollution could be solved by replacing the internal combustion engines car with zero emission vehicles (*i.e.* electric vehicles) in large urban areas [3] and hence, the energy storage systems are critical part of any energy scenario in the present and future. The electrochemical energy storage systems, such as batteries and super-capacitors are the most efficient devices for storing electrical energy. It appears that renewable and green energy related industries will be the main-stream supplier of the future energy demand in the coming decades. However, intermittent renewable energies such as solar and wind will not have the anticipated impact unless we find an efficient way to store and use the electricity produced by these sources, and batteries are an attractive option for this [4]. In other words, batteries or electrical energy storage devices can play an important role in managing the gap between the energy conversion and demand, especially for producing electricity from renewable and sustainable sources [5].

The batteries are electrochemical devices that convert the chemical energy into electrical energy through Faradaic reaction without the Carnot limitation. The batteries are classified as primary and secondary batteries. The primary batteries cannot be recharged and are single use devices. The secondary batteries can be recharged many times [6]. Various types of rechargeable batteries have been developed for personal and commercial use. However, some of them are still

in the experimental stage. In order to meet the demands of energy storage for portable devices, hybrid electric vehicle, and stationary reserves, significant improvements in current battery technology are needed. In addition, batteries with high energy density, improved safety, and low cost, are essential. Among various battery types, lithium ion based batteries have attracted the most attention because of their high theoretical energy density and high power capability for fast charging and low rate of self-discharge [5]. A comparison of volumetric and gravimetric energy densities of the different current battery technologies are shown in the Fig. 1.1. It is clear from

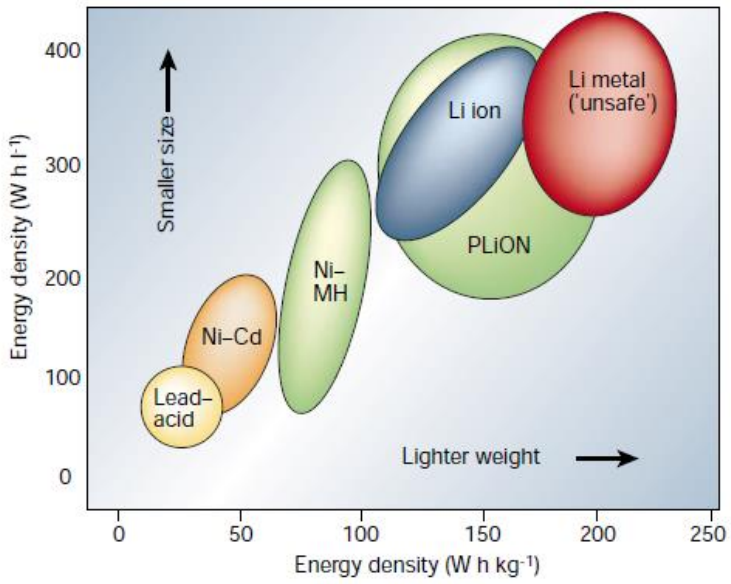

Fig. 1.1 Specific energy density and volumetric energy density of different rechargeable battery technologies [7].

Ragone plot (Fig. 1.1) that lithium ion batteries are superior among the available battery technologies, and share about 63 % of worldwide sales compared to 23% and 14% of the market for Ni-Cd and Ni-MH, respectively [7]. Although, lithium metal batteries have a higher energy density compared to lithium ion batteries but their poor recharge ability and susceptibility for misuse leads to fire or explosions making them unsafe for use. However, lithium metal batteries

based on solid electrolyte with enhanced safety will likely be commercialized in next decade [8]. The lead acid batteries are used in automobile for starting, lighting, and ignition or standby applications. Ni-Cd batteries are more suitable for applications in power tools. Ni-MH and lithium ion batteries are used for small scale applications in portable electronics (mobile phones, laptop and tablet computers, digital cameras, etc.) to large scale applications in automobiles (hybrid electric vehicles, plug in hybrid electric vehicles, and full electric vehicles).

The lithium ion batteries having high power, high capacity, high charging rate, long life but also improved safety and low cost have received most attention at both fundamental and applied levels [7, 8]. The automobile industry is the most expanding market for lithium ion batteries. Figure 1.2 shows the HEV market evolution. The synergic combination of

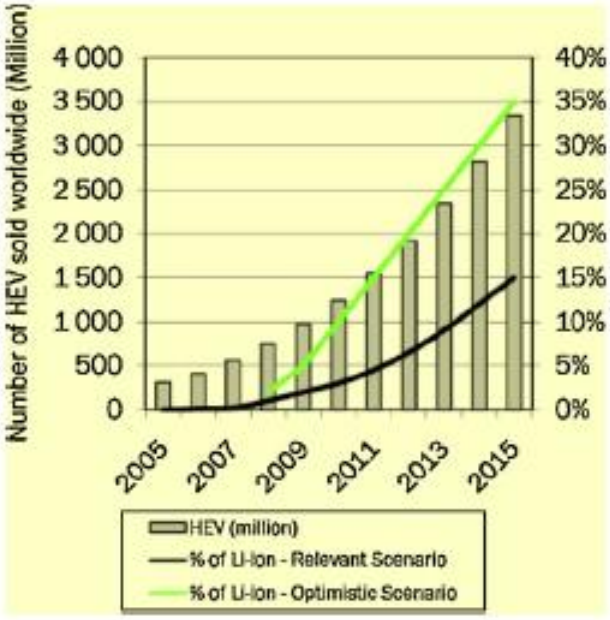

Fig. 1.2 Hybrid electric vehicle (HEV) market evolution [3].

electrochemical batteries with internal combustion engine provides high fuel utilization with proven benefit for fuel economy and for pollution emission control, as well as driving force similar to pure gasoline car if not superior [3]. Much efforts have been made to improve the

lithium ion battery performance, but intense research is still required for developing next generation lithium ion batteries with drastically improved properties in order to meet the demand [8].

1.2 Lithium Ion Batteries: operation principle

Lithium ion batteries are rechargeable electrochemical devices with highest energy density [9]. A Li-ion battery consists of three major components; namely, anode (negative), cathode (positive) and electrolyte. Anode is the source of lithium ions, cathode is the sink for lithium ions, and electrolyte is a medium for ion transport between the positive and negative electrodes, and also serves as a barrier to prevent electrical short circuit between the electrodes. Lithium ion battery is dual intercalation system in which the structure of cathode and anode allows the insertion/extraction of lithium ions. The chemistry of the lithium ion batteries is not unique because there are numerous available materials which show reversible intercalation and served as electrodes [10].

During the recharging, the lithium ions are extracted from the cathode, pass through the electrolyte and then intercalate in the anode. During the discharge, the process is reversed and the electrons pass through the external circuit [11]. The basic working principle of Li ion batteries is shown in the Fig. 1.3. Typical chemical reactions taking place (during the charging), in a Li ion battery are as follows [12],

Cathode: $$LiCoO_2 \leftrightarrow Li_{1-x}CoO_2 + xLi^+ + xe^- \quad (1.1)$$

Anode: $$6C + xLi^+ + xe^- \leftrightarrow Li_xC_6 \quad (1.2)$$

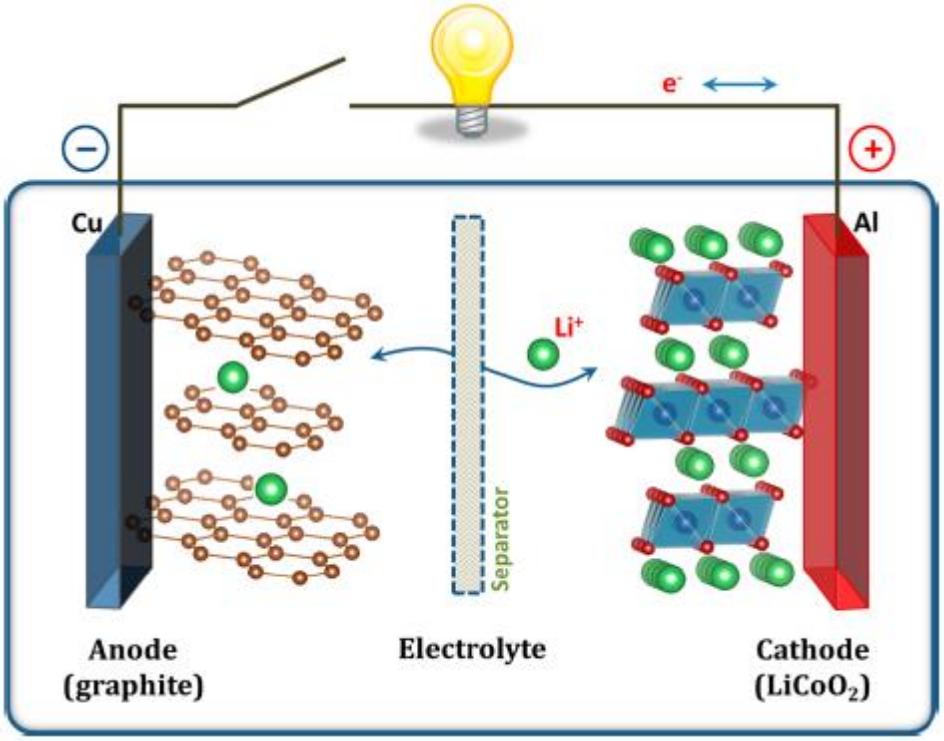

Fig. 1.3 Recharging/discharging intercalation mechanism of Li-ion batteries (cathode is the positive electrode and anode is the negative electrode). Figure is adopted from [2].

The lithium ions flow from anode where they are at high chemical potential to the cathode at low chemical potential during the discharge process in rechargeable Li-ion batteries [13], and the open circuit voltage of an electrochemical cell is determined by the difference between the chemical potential of the cathode and anode

$$V_{oc} = (\mu_A - \mu_C)/e \tag{1.3}$$

where, V_{oc} is the open circuit voltage of the cell, μ_A and μ_C are chemical potentials of the anode and cathode respectively, and e is the fundamental charge.

Figure 1.4 shows a schematic energy diagram of electrode and electrolyte of a Li-ion battery. The "window" of the electrolyte or top of anion-*p* bands of cathodes limits the open circuit voltage V_{oc} and stability window of the electrolyte is defined by the energy gap (E_g) between the

lowest unoccupied molecular orbital (LUMO) and highest occupied molecular orbital (HOMO) of liquid electrolyte or between the conduction band and valence band in the solid electrolyte, shown in Fig. 1.4. The redox or Fermi energy of the cathode (μ_C) or anode (μ_A) should lie within the energy gap (E_g) of electrolyte for the thermodynamic stability of the cell. The chemical

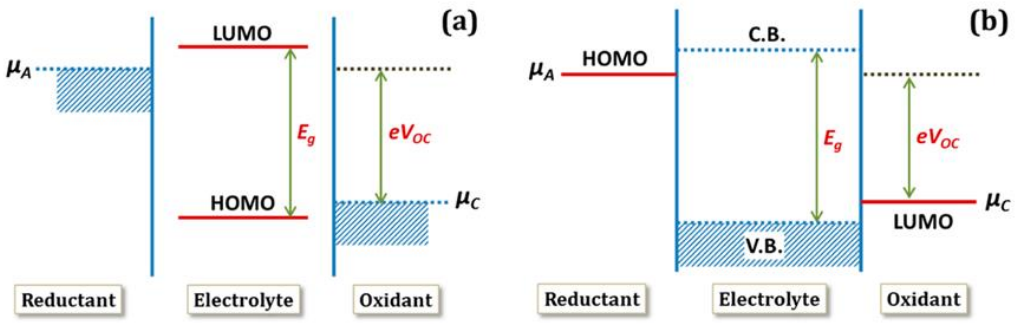

Fig. 1.4 The relative energies of electrolytes window and electrode chemical potential with no electrode and electrolyte reaction (a) liquid electrolyte with solid electrode (anode and cathode) (b) solid electrolyte with liquid or gases reactants. Figure adopted from [2].

potential of anode above the LUMO will reduce the electrode and chemical potential of cathode below the HOMO will oxidize the electrode until a passivation solid electrolyte interface (SEI) layer is formed to block the reactions [2], shown in Fig. 1.5. Thus, this electrochemical stability imposes the limitation of open circuit voltage of cell [14],

$$V_{OC} \leq E_g/e \tag{1.4}$$

The average potential of the cell is also related to the Gibbs free energy of the chemical reaction in the cell [15],

$$\Delta G = nF\Delta E \tag{1.5}$$

where, ΔG is the Gibbs free energy, n is the number of electrons that participate in the redox reaction, F is the Faraday's constant, and ΔE is the redox potential difference between the anode and the cathode reactions.

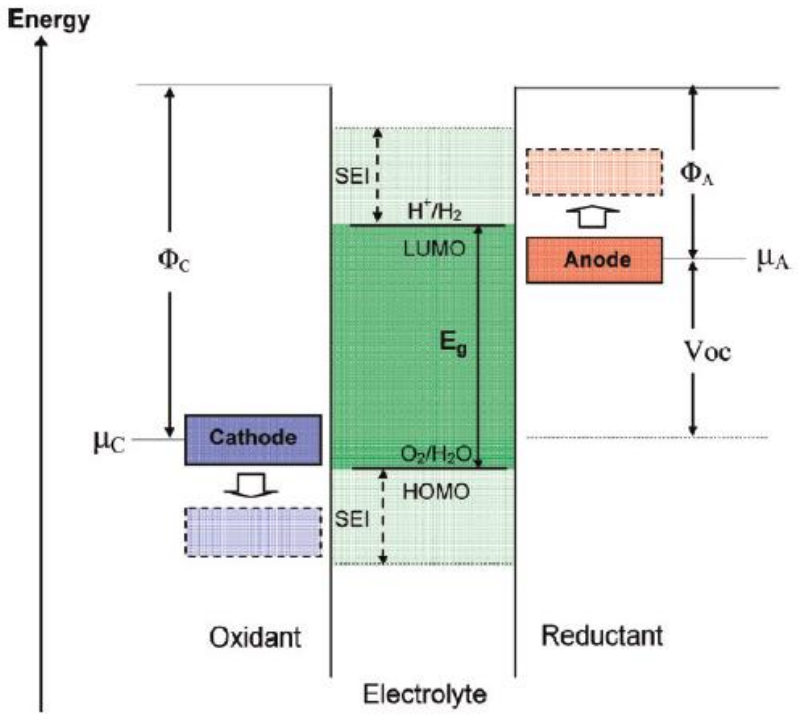

Fig. 1.5 The schematic open circuit energy of an aqueous electrolyte system. HOMO and LUMO are highest occupied molecular orbit and lowest unoccupied molecular orbit respectively. The μ_C and μ_A are the chemical potentials for cathode and anode respectively. Figure adopted from [14].

1.3 Components of Li-ion batteries

The lithium ion batteries contain anode and cathode as electrode and electrolyte as the medium of lithium ion transport and a separator is used for physically isolate the electrodes to avoid short-circuiting. In this section, details of the components of the lithium ion batteries are presented.

1.3.1 Anode

The anode in a rechargeable battery is the negative electrode from which electrons flow out (oxidation process, $Li \rightarrow Li^+ + e^-$) towards the external circuit during discharge. The anode materials are easily oxidized and have low ionization energy to release electrons. The lithium metal (theoretical capacity~3862 $mAh \cdot g^{-1}$) was considered a potential candidate as negative

electrode used first in 1972 for TiS_2, best available intercalation compound at that time [7]. However, dendritic growth of lithium metal affects the cycle-ability [16, 17] and shorts the cell between cathode and anode which eventually leads to explosion [7]. The safety issue with lithium metal has led to search for new anode materials for Li-ion batteries, even though, it has very high capacity among the anode materials. The most common active material for anode is the lithiated graphite (LiC_6) which is a layered compound formed by the graphene sheets, where, lithium ions reside between the graphene sheets, used in commercial batteries. The graphite owns excellent features such as low cost and good cyclic life, low and flat working potential vs lithium. However, the lithiated graphite, LiC_6 has a maximum theoretical capacity ~372 $mAh \cdot g^{-1}$. The low energy density and safety issues due to lithium depositions pose disadvantages for graphite as anode [18], and thus one and two dimensional nanostructures and porous carbon based anodes have been developed to create more active sites in order to increase the energy and power densities [12]. Carbon nanotubes (CNT), nanofibers, and nanowires (1D) structures have high surface to volume ratio and show excellent surface activities. The CNT made anodes exhibit a reversible capacity of 460 $mAh \cdot g^{-1}$ and have reached up to 1116 $mAh \cdot g^{-1}$ with various post treatments (ball milling, acid oxidation, and metal oxide cutting etc.). Recently, Carbon nano-fiber based anodes prepared by low cost electro-spinning techniques, delivered a reversible capacity of about ~ 450 $mAh \cdot g^{-1}$ [19]. Graphene, a 2-D novel carbon material with monoatomic layer with a honeycomb lattice structure has also been used as an anode material. The theoretical capacity calculations for graphene are quite controversial: as single layer, graphene delivers a capacity of 372 $mAh \cdot g^{-1}$, which is comparable to graphite. The capacity values of graphene increase to 780 $mAh \cdot g^{-1}$ or 1116 $mAh \cdot g^{-1}$ depending on the number of graphene sheets in the layer. This difference in the observed capacity is due to the interaction between the lithium and

graphene. In the case of low capacity, the assumption is lithium ions are absorbed at both the faces of graphene (Li_2C_6 stoichiometric) and in the other the assumption is lithium ions are absorbed at the benzene ring in a covalent bond (LiC_2 Stoichiometric) [19]. However, these types of carbonaceous materials are not stable during charge-discharge cycles. Apart from the carbon materials, various alloys of lithium with metal or semimetal elements of groups IV and V, such as, Si, Sn, Ge, Pb, P, As, Sb, Bi, and others, such as, Al, Au, In, Ga, Zn, Cd, Ag, and Mg have been explored as the active anode materials. Si is the most studied anode material and has the highest theoretical capacity of 4200 $mAh \cdot g^{-1}$. Ge and Sn are also promising anode materials with relatively high capacities of 1600 and 992 $mAh \cdot g^{-1}$. Various metal oxides are also widely investigated as possible active materials for anode due to their diverse physical and chemical properties with capacities in between 500 to 1000 $mAh \cdot g^{-1}$ [12].

1.3.2 Electrolyte

The electrolytes are the ionic conducting media through which Li ions move between electrodes during the charging/discharging process. The main requirement for an electrolyte is the non-flammability with a large window between HOMO and LUMO and capability for developing a solid electrolyte interface layer rapidly to block the lithium plating on the carbon anode during the fast charging of the battery [14]. As the water based electrolytes have a limited of voltage window ~1.23 V, non-aqueous electrolytes are used in the lithium ion batteries. A further requirement for electrolytes used in lithium ion batteries is it should have a good lithium ionic conductivity ($>10^{-4}$ $S \cdot cm^{-1}$) but electronically insulating ($<10^{-10}$ $S \cdot cm^{-1}$). Otherwise, it will cause the internal short-circuiting. They should also have high thermal and chemical stability, low cost, non-toxic, and non-flammable [20]. The commercial lithium ion batteries use organic liquid electrolytes, which consist of some lithium salt dissolved in the mixture of liquid organic

carbonates. Ethylene carbonate (EC), diethyl carbonate (DEC), dimethyl carbonate (DMC) and propylene carbonate (PC) are commonly used organic carbonates and lithium hexafluorophosphate ($LiPF_6$) and lithium bis (trifluoromethanesulfonyl) imide (LiTFSI) are used as lithium salts [21]. The electrolyte for Li-ion batteries is optimized for high ionic conductivity and chemical stability [22]. The organic liquid electrolytes used in the present commercial lithium ion batteries have the ionic conductivity of the order of 10^{-2} $S{\cdot}cm^{-1}$, high voltage window (~5V [23]), excellent energy density, and electro-chemical stability. However, organic electrolytes are flammable and easily catch fire which limits their use in large scale lithium ion batteries due to safety concerns [24]. Thus, alternate electrolytes, such as, ionic liquids, polymer, gel, and solid electrolytes are proposed and studied due to this reason. The salts with low melting point that are liquid at room temperature or below, are called the room temperature ionic liquid (RTIL), which, form a new class of electrolytes [25], and are promising candidates, owing to their desirable properties over carbonate electrolytes. They are non-flammable with high boiling point, low vapor pressure, better thermal stability, high lithium solubility, and above all high potential (~5.3 V vs Li^+/Li). However, ionic liquids have high viscosity and poor stability at voltages below 1.1 V [14].

The polymer electrolyte is considered as one of the safe electrolytes due to low volatility and can eliminate the need for the separator in rechargeable lithium ion batteries, and the other advantage is the flexibility in design and can be fabricated in different configurations such as cylindrical, prismatic, coin, and flat cells. The polymers electrolytes are based on high molecular weight polymers dissolved lithium salt and are solvent free. Polyethylene oxide (PEO) containing lithium salts is the most widely investigated polymer. However, polymer electrolytes exhibit very low lithium ion conductivity (~10^{-5} to ~10^{-8} $S{\cdot}cm^{-1}$) at room temperature, which is

too low for large-scale applications in power systems. The gel based electrolytes containing both lithium salts and polar solvent dissolved in inactive polymer network show drastically increased ionic conductivity [8, 14].

The solid electrolytes based on inorganic ceramics are the safest electrolytes and have been used in thin film battery applications [14]. The garnet structure, cubic phase $Li_7La_3Zr_2O_{12}$ (LLZO) has attracted the most attention due to its high chemical stability, ionic conductivity ($>10^{-4}$ $S \cdot cm^{-1}$), and wide potential window (>5 V vs Li/Li^+) [26, 27].

1.3.3 Separator

The cathode and anode should be electrically isolated to prevent short-circuiting in the cell. A separator material is used to physically isolate the cathode and anode in the lithium ion battery design. The separator is critical determinant of the battery safety. It is an electrically insulating polymer film, impregnated in electrolyte between anode and cathode, to prevent electron flow to avoid the shorting of cathode and anode. The separators should be porous to allow the movement of Li ions through electrolyte. Polypropylene or polyethylene separators are commonly used in most of commercial lithium ion batteries.

1.3.4 Cathode

The cathode is the positive electrode, where the electrochemical reduction takes place during discharge reaction. Generally, cathode materials are prepared in the lithiated state, so that they can pair with delithiated anode. During the discharge in Li ion batteries, a cathode gains electrons from the external circuit and hence reduction takes place at the metal center in the cathode reducing it to a lower oxidation state (i.e. Fe^{III}/Fe^{II}). Commonly used cathode materials are transition metal oxides. The cathode plays the most crucial role in determining the energy

density of the Li ion batteries. The ideal cathode materials have the following important desirable characteristics:

- High Gibbs free energy to provide high energy density
- Fast lithium diffusion rate to provide high rate capability
- Made from abundant materials to provide low cost
- High chemical and electrochemical stability for improved safety
- Structural and chemical stabilities to provide high cycle life

1.4 Types of cathode materials

The cathode plays an important role in determining the performance of lithium ion batteries and has been the object of comprehensive study in developing the desired properties listed above. At present, there are various classes of cathode materials available. These materials are

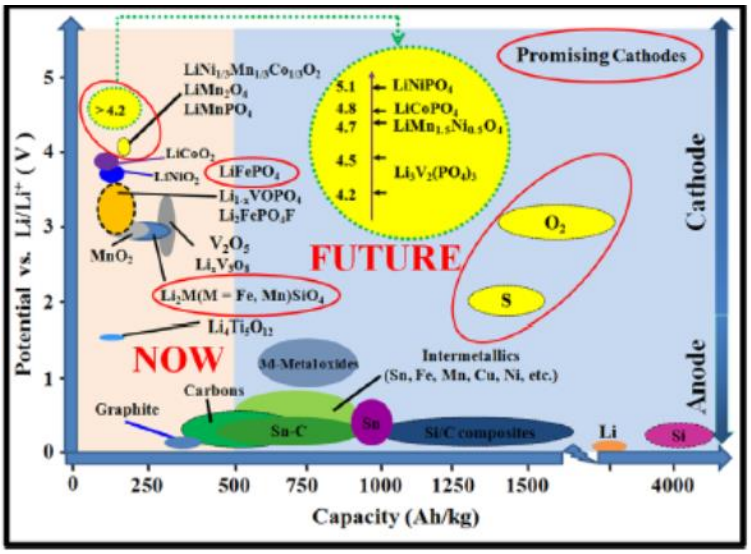

Fig.1.6 Capacity versus potential curve of different electrode of Lithium ion batteries (adopted from [1]).

classified based on their structure; layered mixed oxides ($LiCoO_2$, $LiNiO_2$, $LiNi_{1/3}Co_{1/3}Mn_{1/3}O_2$, $LiNi_{1-x}Co_yO_2$, $LiNi_{0.05}Mn_{0.5}O_2$, and $Li_{1.2}Cr_{0.4}Mn_{0.4}O_2$), Zigzag ($LiMnO_2$), 3-dimensional spinel ($LiMn_2O_4$, $LiCoMnO_4$, $LiNi_{0.5}Mn_{1.5}O_4$, and $LiCoVO_4$), and 1-dimentional tunnel type olivine

structure ($LiFePO_4$, $LiMnPO_4$, Li_2FeSiO_4, Li_2MnSiO_4, Li_2NiSiO_4, and Li_2CoSiO_4). These are the three major types of cathode materials for the lithium ion batteries. The other types of cathode materials are proposed and under investigation include organic, sulfur, air, and conversion cathodes. A plot of capacity versus potential of cathode and anode materials used in lithium ion batteries is shown in the Fig. 1.6. In the following section, cathode materials will be reviewed in detail on the basis of their structure with a focus on olivine compounds.

1.4.1 Layered oxide materials

The layered oxides have general formula $LiMO_2$, where M= Co, Ni, V, and Mn etc [28]. The structure of layered compound is shown in Fig. 1.7, and the voltage as a function of *x* for Li_xCoO_2 is shown in the Fig. 1.8. The octahedral connected slabs of MO_6 and Li layers are stacked alternately to prevent electrostatic repulsion. The $LiCoO_2$ is the first cathode which is commercialized by Sony Corporation in lithium ion battery and now dominates the market [15] and is used in most of high performance portable electronic devices [7].

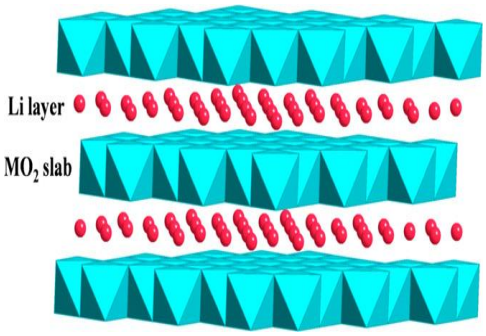

Fig. 1.7 The crystal structure of layered $LiMO_2$ (red: Lithium ions and blue: the MO_2 slab). Adopted from [29].

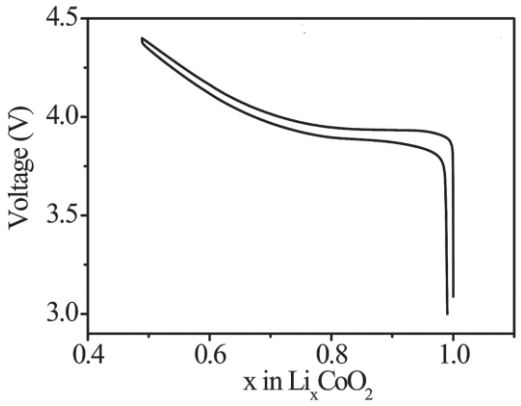

Fig. 1.8 Voltage composition curve for $LiCoO_2$. Adopted from [30].

The $LiCoO_2$ is the favored material due to their high energy density, excellent cyclability, and high operating cell voltage. However, high cost, poor stability at high state of charge, and

toxicity has limited their applications. The theoretical capacity of $LiCoO_2$ is 274 $mAh \cdot g^{-1}$ if one Li ion extracted from the $LiCoO_2$ lattice. However, the useful capacity of $LiCoO_2$ is only about ~140 $mAh \cdot g^{-1}$, which is about ~50% of theoretical capacity, due to the intrinsic structural instability of the material when more than half of the Li ions are removed [31, 32]. The cyclability of the $LiCoO_2$ cathodes could be improved by modifying the surface with electrochemically inactive oxide such as Al_2O_3, ZrO_2, and TiO_2, delivering the reversible capacities close to 200 $mAh \cdot g^{-1}$ [33]. The second drawback of this material is the presence of toxic and expensive Co ion in $LiCoO_2$ which introduces environmental problems and raises the cost of the battery. The research has moved from using $LiCoO_2$ to its derivatives in which Co ions are either partially or fully substituted by more abundant and environment friendly transition metal ions such as Ni and Mn. However, $LiNiO_2$ cathodes have the advantages such as low cost and less toxic compared to $LiCoO_2$, also provide the cell potential ~4.0 V but it suffered from few problems; (a) difficult to synthesize, (b) Jahn-Teller distortion associated with low spin Ni^{3+} ions, (c) irreversible phase transition during charge/discharge process, and (d) release of oxygen at elevated temperature and safety concern in the charged state. Thus, $LiNiO_2$ is not considered as the potential candidate for lithium ion batteries [33]. Another approach has led to mixing the $LiNiO_2$ and $LiMnO_2$ in 1:1 ratio, forming the $LiNi_{05}Mn_{0.5}O_2$, and the formation of Li-$Co_{1/3}$–$Ni_{1/3}$–$Mn_{1/3}$–O_2 layered compound which is called NMC cathode to improve the electrochemical properties [29].

1.4.2 Spinel oxide materials

The main reason for using $[B_2]X_4$ framework of $A[B_2]X_4$ spinel for cathode or anode as a stable host structure for lithium ion batteries is its demonstrated high cell voltage. Spinel anode and cathode materials should provide low and high cell voltage against lithium metal. Many

spinel materials have been evaluated as cathode for lithium ion batteries with lithium at A site and (Co, Ni, Ti, V, and Mn) at B site [34]. The cubic spinel $LiMn_2O_4$ is one of alternative and promising material for cathode, which has a theoretical charge storage capacity ~148 $mAh{\cdot}g^{1}$ [33, 35], corresponding to one lithium ion extraction from $LiMn_2O_4$ due to oxidation of Mn^{3+} to Mn^{4+}. The structure of LiM_2O_4 spinel is shown in Fig. 1.9, and the voltage profile with composition for $Li_2Mn_2O_4$ is shown in the Fig. 1.10. The M cations occupy the octahedral site, however, 1/4 of them are situated in the Li layer and this leads to 1/4 vacant sites in the transition metal layer. Li ions occupy the tetrahedral sites in Li layer that share faces with the empty octahedral sites in the transition metal layer. The structure is based on a three-dimensional MO_6 and MO_4 hosts and the vacancies in transition metal layer that ensures the 3-D Li diffusion pathways [29].

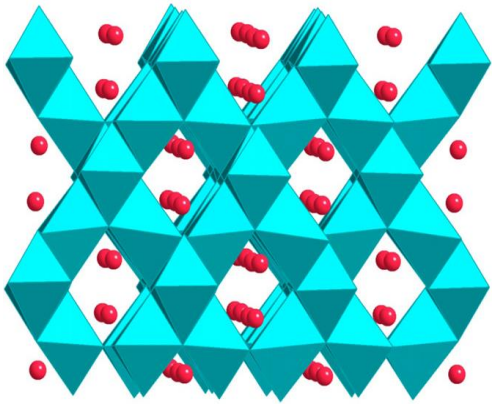

Fig. 1.9 The crystal structure of layered LiM_2O_4(red: Lithium ions and blue: transition metal ion) adopted from [29].

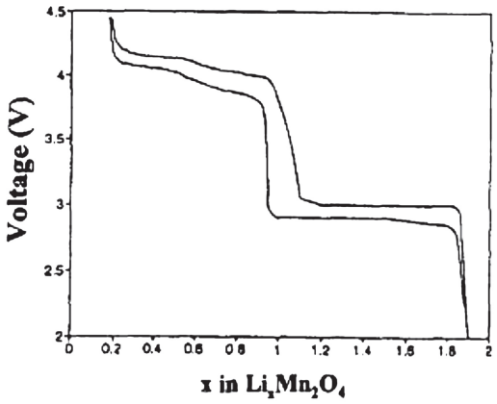

Fig. 1.10 Voltage-composition curve for layered LiM_2O_4. adopted from [30].

The spinel $LiMn_2O_4$ was proposed as a cathode for the Li ion battery by Thackeray *et. al.* in 1983 [15, 36, 37]. The spinel possesses about 10% less capacity than $LiCoO_2$, have the advantages of low cost and nontoxic it suffers with severe capacity fading problem during charge-discharge cycles at elevated temperature [7, 38]. There are two main reasons for the

decline in capacity: First, dissolution of Mn^{2+}into the electrolyte generated by the disproportional reaction $2Mn^{3+} \rightarrow Mn^{4+} + Mn^{2+}$ that is being promoted by the Jahn-Teller distortion caused by Mn^{3+} and the second, evolution a new structural phases during cycling. The cycling performance of the spinel materials has been improved by partial substitution of Mn with Ni, leading to $LiNi_{0.5}Mn_{1.5}O_4$ which shows the best overall electrochemical performance among the spinel materials [29].

1.4.3 Polyanion materials

The polyanion cathode materials have a tetrahedral structural unit $(XO_4)^{n-}$and their derivatives $(X_mO_{3m+1})^{n-}$, where, X = B, P, V, S, As, Mo, Si, and W, are combined with the MO_x polyhedra with strong covalent bonding. For example, MO_6 octahedral for the olivine structure and MO_4 tetrahedral for silicate based cathodes [9, 30] as shown in Fig. 1.11. They exhibit two-three phase system during charge-discharge processes: $Li_{(1-2)}\ MXO_4 \Leftrightarrow LiMXO_4 \Leftrightarrow MXO_4$.

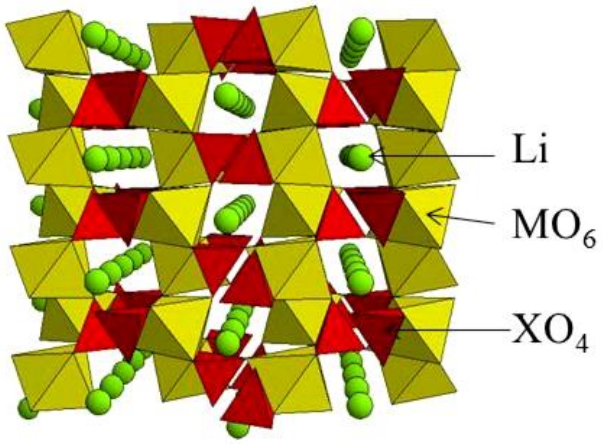

Fig. 1.11 The olivine crystal structure of polyanion cathodes (yellow: transition metal ion, green: Li ion and red: X ion depending upon the P, V, etc).

These materials have a high thermal and chemical stability due to strong X-O covalent bonding. Thus, the advantage of polyanion cathode is that the binding energy of oxygen

enhances the stability and safety of the battery, making them more suitable for large scale lithium ion batteries [9]. Various class of polyanion compounds; Phosphates ($LiMPO_4$), Borates ($LiMBO_3$), Pyrophosphates ($Li_2MP_2O_7$), and Silicates (Li_2MSiO_4) have been investigated as cathode for lithium ion batteries due to their inherent properties. The theoretical capacity of polyanion cathodes is very high compared to conventional layered oxides and spinels, (170-330 mAh·g). The phosphates have a theoretical capacity ~170 $mAh \cdot g^{-1}$ and borates with lightest polyanion unit (BO_3) have the theoretical capacity ~200 $mAh \cdot g^{-1}$. Pyrophosphates and silicates offer the theoretical capacity ~ 220 and 330 $mAh \cdot g^{-1}$ respectively due to the possibility of two lithium ion insertion/extraction per transition metal in the material [39]. However, these materials have poor electronic conductivity. The optimization for impurity free synthesis of polyanion compounds is very complex and requires in-situ carbon coating, and doping to enhance their conductivity for facilitating the electron mobility. These materials provide high voltage cell, and are environmentally friendly. These materials are ideal cathodes for large scale Li-ion batteries due to their structural and chemical stability providing high safety margin.

1.4.3.1 Phosphates

The lithium metal phosphates ($LiMPO_4$, where, M = Fe, Mn, Ni, or Co) are the most intensely studied materials among the polyanion cathodes for Li ion batteries. The crystal structure of phosphates is olivine which is described as a slightly distorted hexagonal closed packed oxygen array resulting in an orthorhombic structure with space group Pmnb [10]. Among all the olivine phosphates, $LiFePO_4$ is extensively studied and developed material, and it is considered as the most promising cathode material for hybrid electric vehicle/electric vehicle. $LiFePO_4$ as a positive electrode was first proposed by A.K. Padhi *et. al.* [40]. Iron phosphate has various advantages; low cost due to abundantly available raw materials, high thermal stability

and is environmentally friendly [41, 42]. The voltage profile with lithium concentration for $LiFePO_4$ is shown in Fig. 1.12. $LiFePO_4$ shows a wide flat plateau compared to $LiCoO_2$ and $LiMn_2O_4$.

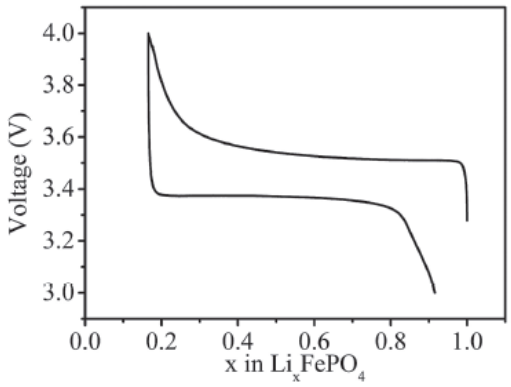

Fig. 1.12 Voltage-composition curve for Li_xFePO_4 (adopted from [30]).

1.4.3.2 Silicates

Lithium metal ortho-silicates are also a class of the polyanion cathodes and have gained considerable interest in the past few years. The silicate cathodes were first proposed by M. Armand [43, 44]. The silicate compounds Li_2MSiO_4; where, M = Ni, Mn, Fe, and Co are potential cathode materials in Li-ion batteries due to their superior properties, like, high theoretical capacity (>330mAh·g^{-1}), great thermal stability due to Si-O covalent bonds, environmental friendliness, and low cost [45, 46]. The capacity of cathode for Li-ion batteries could be increased if the materials could be made to release more than one electron during charging process. The lithium transition metal silicates with 3*d* metals change oxidation states from +2 to +3 and +3 to +4 providing two lithium ion extraction per formula unit during de-intercalation/intercalation process. However, very limited success has been attained in extracting two lithium reactions in Li_2MSiO_4 till now [9].

Silicate materials have very low electronic conductivity (~$5x10^{-16}$ S·cm^{-1} for Li_2MnSiO_4 and ~6×10^{-14} S·cm^{-1} for Li_2FeSiO_4 [46]) compared to other cathode materials (~10^{-4} S·cm^{-1} for $LiCoO_2$, ~10^{-3} S·cm^{-1} for $LiNiO_2$, 10^{-6} S·cm^{-1} for $LiMn_2O_4$, ~10^{-9} S·cm^{-1} for $LiFePO_4$ and ~10^{-10} S·cm^{-1} [47]). The research challenges that remain to be addressed are: synthesis of pure phase, coating of silicate materials with highly conducting carbon materials such as carbon black or graphene, cation doping to increase electronic conductivity, and reducing the particle size to the range of a few nanometers for reducing the diffusion length of lithium ions.

The calculated average de-insertion lithium voltage for Li_2MSiO_4 system is shown in Fig. 1.13 [43]. In principle, it is possible to extract lithium ions fully and provide two electrons per formula unit due to two oxidation couples (M^{2+}/M^{3+} and M^{3+}/M^{4+}). The extraction of second lithium ion in silicate system occurs at a very high voltage (>4.5 V), which is the stability limit

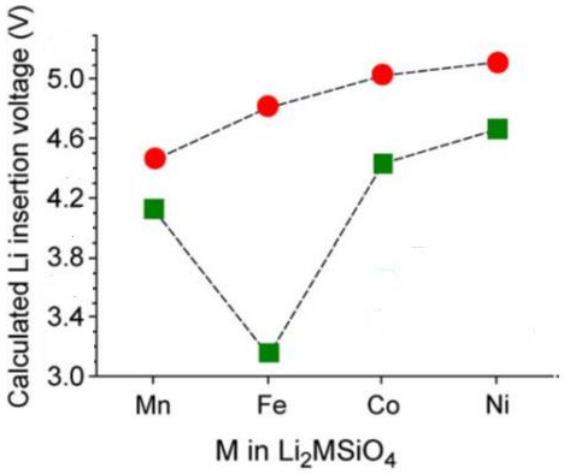

Fig. 1.13 The calculated lithium de-insertion voltage at different oxidation for Li_2MSiO_4 (adopted from [43]).

for most of the current electrolytes used in Li-ion batteries. The Li_2FeSiO_4 shows a two-step voltage plateaus, one at 3.2 V and the other at 4.8 V. The second lithium ion de-intercalation

voltage plateaus of Li_2CoSiO_4 and Li_2NiSiO_4 are above 5.0 V, which makes their use in Li-ion battery applications very difficult. Furthermore, Co is expensive and toxic [46].

In the case of Li_2FeSiO_4, The reversible reaction of more than one lithium ion extraction/insertion form Li_2FeSiO_4 is given by the following reaction,

$$Li_2Fe^{2+}SiO_4 \leftrightarrow LiFe^{3+}SiO_4 + Li^+ + e^- \leftrightarrow Li_{1-x}Fe^{4+}SiO_4 + (1+x)Li^+ + (1+x)e^- \quad (1.6)$$

In the first part of Eq. (1.6), Li_2FeSiO_4 gives rise to a reversible one lithium ion extraction/insertion. The second part of equation describes the extraction/insertion more than one lithium in Li_2FeSiO_4 during the charge/discharge process.

1.5 Crystal structure and phase stabilities of silicates

The crystal structure of Li_2MSiO_4 is categorized as LISICON (lithium super ionic conductor), which allows a wide range of solid solutions with various composition. However, their crystal structure is not fully understood [48]. These materials belong to a tetrahedral structure, which has a large variety of polymorphs. The crystal structure of these compounds is related to the Li_3PO_4 structure. This type of crystal structure has approximately hexagonal closed packed anions with cations residing in the half of the tetrahedral sites avoiding the pairing between the tetrahedral sites. There are two main classes of polymorphs in the silicates namely, β and γ, based on the distribution of the cations over the available tetrahedral sites. The β and γ polymorphs are formed at low and high temperatures. During the synthesis of Li_2MSiO_4, a mixture of different polymorphs is obtained because of small difference in the formation energy of these polymorphs. However, by controlling the temperature and pressure during synthesis and post heat treatment of the materials, the different polymorphs can be separated [9].

In the γ polymorph, both corner and edge sharing tetrahedra exist with half of them pointing along one direction of the c-axis. The γ polymorph crystallizes in three different space groups

$P2_1$, $Pn2_1$ and Pmnb. The β polymorph has only corner sharing tetrahedra with all of them pointing in the same direction, parallel to the *c*-axis. The most common space group of Li_2MSiO_4 family is $Pmn2_1$ [49]. The crystal structure of the different polymorphs is shown in the Fig. 1.14.

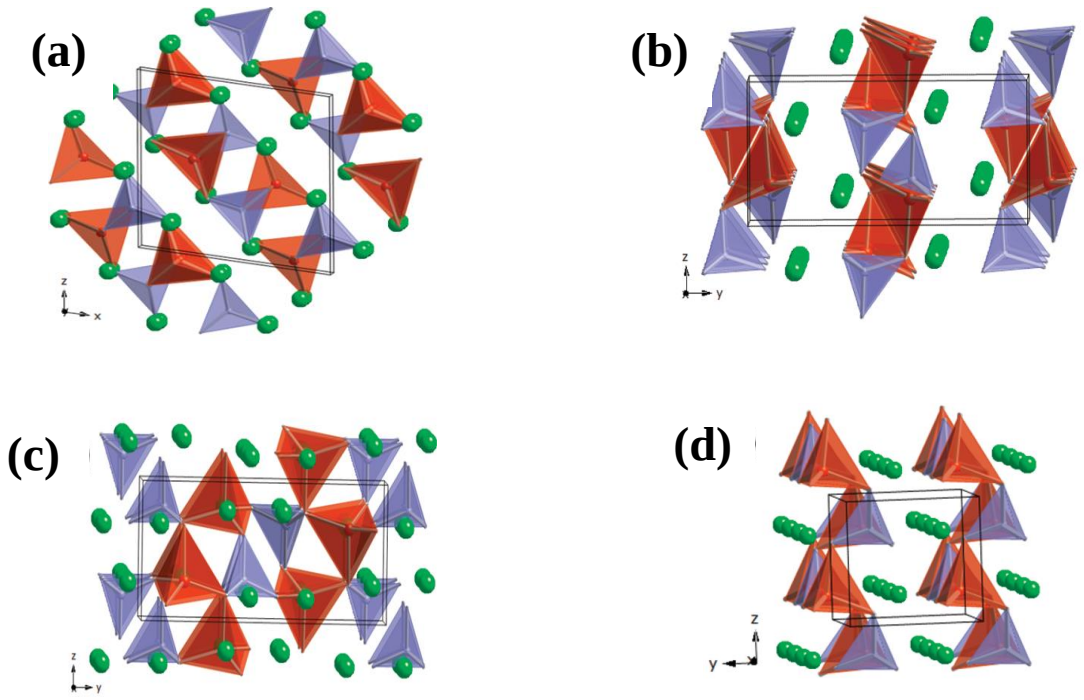

Fig. 1.14 The crystal structure of Li_2FeSiO_4 polymorphs: (a) $P2_1$, (b) Pmnb, (c) $P2_1/n$, and (d) $Pmn2_1$. The figure is adopted from [49]. The color codes are as follows; green: Li, gray: Si and brown: Fe

1.6 Methods for enhancing the electrochemical performance of Li_2FeSiO_4

The capacity of cathode or anode can be improved by enhancing the electronic conductivity and ionic diffusivity [50]. The polyanion cathode materials exhibit extremely low electronic conductivity (~10^{-9} to 10^{-16} $S{\cdot}cm^{-1}$) and low Li^+ ion diffusion coefficient. In order to improve the electrochemical performance, various processing approaches (*i.e.* carbon coating and nano-engineering of materials, and doping with metal) are developed. In the following section, we will describe the methods used for enhancing the electrochemical performance of Li_2FeSiO_4.

1.6.1 Carbon coating

The coating of conducting carbon around the individual particles is supposed to be a very effective way of improving the electronic mobility in polyanion cathodes. At the same time, it acts as buffer layer preventing the particle growth and reduces the agglomeration during the high temperature calcination. There are two ways of carbon coating: (a) *in-situ* and (b) *ex situ*. In the *in-situ* method the carbon source are mixed with the precursors initially and then annealed at high temperature, which forms a thin and homogenous carbon layer on the surface of particles. However, this method is prone to formation of impurities in the final product. In the *ex-situ* method, conducting carbon precursor is mixed with pure materials by ball-milling/grinding and subsequent annealing. This method of coating has very little effect on morphology and the impurity formation in the pure material [45].

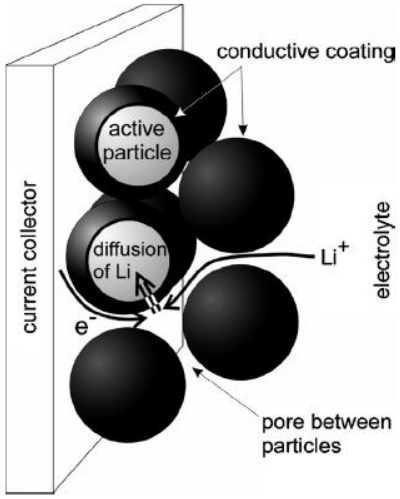

Fig. 1.15 Schematic showing the lithium ion and electron transport in carbon coated active electrode material with low conductivity (adopted from [51]).

The carbon coating also hinders the particle growth of active materials during the heat treatment and shortens the lithium diffusion path length [45, 52, 53], improves the specific

capacity, rate capability by providing the fast lithium ion diffusion and transport. The lithium ion and electron transport in carbon coated active materials is shown in Fig. 1.15.

So far, various surfactant and carbon sources have been used to synthesize the Li_2FeSiO_4/C composites cathode materials. Some of the surfactants used as carbon source include, sucrose [54-56], polyethylene glycol (PEG) [57-59], P123 [60-65], ascorbic acid [66, 67], citric acid [68-71], CNF/CNT [64, 72-77], carbon nanosphere [78], rGO/Graphene [65, 79-82], among others.

1.6.2 Nano-engineering of particles

The morphology and particle size of the electrode materials play an important role in determining the electrochemical performance. The electrochemical performance can be improved by reducing the particle size or designing the architecture of the electrode materials to nano-scale [83]. The Li^+ ion diffusion coefficient is related to the diffusion path length and characteristic time/rate of charging and discharging is given by [84],

$$\tau = \frac{L^2}{4\pi D} \tag{1.7}$$

where, L is the particle size, D is diffusion coefficient of Li^+ ion in the host lattice, and τ is the characteristic time. It is clear that reducing the particle size of electrode materials, the rate performance of Li-ion batteries can be improved by tailoring the size from micron to nano-scale. The nano-electrode could offer stable cycling, high power density and fast kinetic reaction. The advantages and disadvantages of nano-electrodes for lithium batteries are [32, 85, 86],

Advantages

- Small particles reduce the path length for electrons and Li+ ions within the particles, improving the rate capability.
- Small particles increases the surface to volume ratio, and the high surface area leads to better utilization of the active material, thus improving capacity and rate capability.

- The smaller particles enhance the accommodation of the strain during lithium insertion/extraction, leading to improvement in cycle life.

Disadvantages

- The packing density or volumetric energy density of the battery decrease due to small size particles and high surface to volume ratio.
- Nano-size particles enhance the reactivity of electrodes and lead to side reactions with electrolyte causing self-discharge, poor cycling, and capacity fading.
- Complex methods required to synthesis of nano-size particles increase the cost of process.

The porous structure reduces the Li^+ diffusion path length and shortens the Li^+ diffusion time in Li_2FeSiO_4. The meso-porous and macro-porous structure containing a large number of pores significantly influences the electrochemical performance [45]. 3-D macroporous graphene-Li_2FeSiO_4 composites delivered a discharge capacity of ~315 $mAh{\cdot}g^{-1}$ at 0.1C rate and showed an excellent stability for 1000 cycles at 20, 30, and 50C rates [65]. Li_2FeSiO_4 nanorods bonded with graphene delivered the discharge capacity of ~300 $mAh{\cdot}g^{-1}$ and improved stability and rate capability [81]. D. Rangappa, *et. al.* [76] achieved theoretical capacity at 45^o C at 0.02C rate for nanosheets of Li_2FeSiO_4 with MWCNT (5%) composite. The morphology and porosity plays an important role in designing the electrode for Li^+- ion batteries.

1.6.3 Metal doping/lattice engineering

Carbon coating does not increase the lattice electronic conductivity or lithium diffusion coefficient within the crystal but only improves the surface conductivity of cathode materials. The supervalent cations doping is an effective way to improve the lattice conductivity and hence the electrochemical performance of cathode material. The lattice electronic conductivity of

$LiFePO_4$ was increased by more than 10^8 using doping [41]. Up to now, various metal ion doping are investigated to improve the electrochemical performance in Li_2FeSiO_4, for example, Magnesium [87, 88], Yttrium [89], Chromium [90], Cadmium [91], Manganese [92, 93], Nickel [94, 95], Zinc [94], Copper [94], and Vanadium [96] etc., have been reported in the literature. Zhang *et. al.* [91] showed that Cd incorporates into the lattice of Li_2FeSiO_4 increasing the defect concentration and electronic conductivity, thus improving the lithium diffusion process, confirmed by positron annihilation lifetime spectroscopy and Doppler broadening spectroscopy. Y-doped Li_2FeSiO_4/C composite showed an enhanced electrochemical performance, attributed to its improved electronic conductivity, lithium ion diffusion coefficient and structural stability due to proper amount of Y doping in Fe sites. The bandgap energy of Li_2FeSiO_4 decreases with increasing Y concentration, as confirmed by UV-Vis spectroscopy. The decrease in bandgap is attributed to the insertion of Y^{3+} to Fe^{2+}, which introduces the some impurity levels in bandgap of Li_2FeSiO_4, thus enhancing the electronic conductivity and reducing the lattice vibration, which stabilize the crystal structure [89]. The decrease in bandgap is also confirmed by density functional theory calculations on V doped Li_2FeSiO_4 with increasing the V concentration and enhances electronic conductivity and electrochemical performance [96]. Recently, Qu *et. al.* [88] claimed that Mg-doping could help decrease the charge-transfer resistance and increase the Li^+ ion diffusion.

The doping can improve the electrochemical performance but the interpretation of doping effect is complicated because of the interrelation between the morphology, microstructure and doping as dopant additions can affect the microstructure [97].

1.8 Motivation and scope of thesis

Li_2FeSiO_4 is considered as potential candidate for LIB technology and has gained most attention among the polyanion cathode materials due to its intrinsic properties; low cost, higher chemical and thermal stability due to Si-O covalent bond, better safety, and high specific capacity (330 $mAh \cdot g^{-1}$), as mentioned earlier. However, its very low electronic conductivity and slow lithium diffusion significantly limit its use in large format cell for industrial applications. As discuss earlier, various techniques are developed to overcome these limitations. The objective of this thesis is to investigate the combined effect of in-situ carbon coating and metal (Mg) doping to improve electrochemical performance of nanocomposites of Li_2FeSiO_4/Carbon. We used sol-gel and solvothermal methods to synthesize nanostructured Li_2FeSO_4/carbon composites.

The scope of the thesis is described below.

1. Carbon coating is a most common and simple approach to enhance the electronic conductivity of the cathode materials and hence, the electrochemical properties. In the first project, we used P123 as carbon source and structure directing agent (SDA) in order to coat Li_2FeSiO_4 particles with conducting carbon. We have synthesized Li_2FeSiO_4/C by sol-gel (SG) and solvo-thermal (ST) methods, followed by annealing at different temperatures and a comparative study on their structural and electrochemical is conducted and also studied the effect of annealing temperature on the electrochemical properties. We found that ST synthesized Li_2FeSiO_4/C show improved electrochemical performance at all the temperature and Li_2FeSiO_4/C (ST) annealed at 600 ^oC for 9 hours delivers a discharge capacity of ~276 $mAh \cdot g^{-1}$ at C/30 rate, which is about ~84% of

theoretical capacity. This sample showed the best electrochemical results among all other samples.

2. In the second project, we investigated the effect of Mg^{2+} doping on electrochemical properties of Li_2FeSiO_4/C and found that 1% Mg doped Li_2FeSiO_4/C shows improved electrochemical performance and further increase in Mg^{2+} concentration, degrades the performance of Li_2FeSiO_4/C. A detailed study of the structural, morphology, and electrochemical of Mg doped Li_2FeSiO_4/C is presented.
3. Carbon nanofibers/carbon nanotubes (CNF/CNT) and reduced grapheme oxide (rGO) are known for their high surface area and electronic mobility. Carbon nanofibers and rGO might act as substrates for the deposition of Li_2FeSiO_4 nanoparticles on their surfaces during the in-situ synthesis process and thus enhance their electronic conductivity. Further, rGO having more surface area compared to CNF might provide more contact area enhancing the Li^+ ion diffusion. In this work, we have synthesized the ternary nano-composite of Li_2FeSiO_4/CNF/rGO and compared their structural, microstructure and electrochemical properties with corresponding Li_2FeSiO_4/CNF nano-composite. Both the composites show very stable cycle performance at 1C rate for 200 cycles with 90% retention of their initial discharge capacities, showing the excellent stability. However, Li_2FeSiO_4/CNF/rGO shows better electrochemical performance at higher rates.

CHAPTER 2 SYNTHESIS AND CHARACTERIZATION TECHNIQUES

This chapter describes the synthesis methods of Li_2FeSiO_4 and various analytical techniques (X-ray diffraction, Scanning electron microscopy (SEM), Transmission electron microscopy (TEM), Electrical conductivity measurement, surface area and porosity, etc.) used to characterize the nano-composites of Li_2FeSiO_4/Carbon. This chapter also gives a brief description of electrode and coin-cell fabrication to test the electrochemical performance of cathode material in lithium-ion batteries. The techniques of electrochemical impedance spectroscopy (EIS), cyclic voltammetry (CV), and galvanostatic charge/discharge cycles to measure the electrochemical properties of the electrode materials are described.

2.1 Synthesis of silicates

Li_2MSiO_4 exhibits different polymorphs which are obtained from different synthesis methods by varying the temperature and pressure conditions. The lithium intercalation behavior greatly depends on the types of polymorphs. The Li_2MSiO_4 with $P2_1$ symmetry has higher electronic conductivity among all polymorphs. However, both low and high temperatures orthorhombic are more stable [45]. It is very critical to optimize the synthesis conditions to obtain desirable polymorph for gaining improved electrochemical performance with low cost. The optimization methods have mainly focused on synthesis conditions to prepare controllable shape and size with thin uniform layer of carbon coating [9]. A number of methods have been developed and optimize to synthesize Li_2FeSiO_4, namely, solid state reaction [98-100], sol-gel [73, 79, 87, 96, 101, 102], and solvo-thermal/hydrothermal [54, 71, 103-105], supercritical [66, 76], microwave [106, 107], spray pyrolysis [108], combustion [109, 110], and hydrochemical [78]. In our work, we have synthesized Li_2FeSiO_4/C by sol-gel and solvothermal methods. The annealing at high temperatures is used in both of these methods of preparation to obtain the final product. The

details of synthesis methods for samples prepared for this study will be given in respective Chapters in this thesis. However, a brief and general description of the sol-gel and hydrothermal/solvothermal techniques is described here.

2.1.1 Sol Gel method

The sol–gel synthesis method is widely used in material science and ceramic engineering. It is a wet chemical technique, and produces high purity, homogenous and small particle size due to better mixing of the precursors. In this method, the staring materials are dissolved in proper solvents and let to form sol that finally leads to formation of a gel containing a liquid phase and a solid phase. Then the gel is dried and heat treated at temperature ranging from 500 ^{o}C to 700 ^{o}C. Different precursors and solvents are used to obtain the desired materials. This method has the advantage that it produces a uniform carbon coating in situ, when organic solvent/chelating agents or other carbon-based compounds are used during the synthesis. The sol–gel process is considered as one of the best methods for preparing silicate based cathode materials with small particle size [9].

2.1.2 Hydrothermal/Solvothermal method

This method uses relatively low temperature for the synthesis and allows control of morphology with different shape, such as, spherical, cubic, fibrous, and plate-like and fine crystals particles with varying size from nano-meters to tens of microns. In this method, the precursors are dissolved in water or a solvent and then sealed in an autoclave. The sealed autoclave is kept at above the boiling temperature of the solvent at high pressure for a desired reaction time. The heating process could be conventional or microwave assisted.

Furthermore, by changing the thermodynamic variables such as reaction temperature, pH of the solution, and concentrations of the precursors along with changing the kinetic parameters such as stirring speed, the particle size and morphology of the final product can be varied [9].

2.2 Structural and surface characterization techniques

2.2.1 X-ray diffraction (XRD)

X-ray diffraction (XRD) is a most powerful and commonly used technique in the science and engineering to investigate the phase purity, phase composition, crystalline nature of material, grain size, lattice constants and geometry, identification of unknown materials, preferred orientation of polycrystals, orientation of single crystals, stress, internal lattice strain, and defect, etc [111] . The XRD pattern of a material depends on the atomic positions in the unit cell of the crystalline materials and thus, it is like the finger print of the material [112]. XRD does not require a complex sample preparation and is a nondestructive technique [113]. In this work, x-ray diffraction has been used to investigate the phase of materials, impurities, and grain size calculation. A collimated beam of X-ray with wavelength typically ranging from 0.7 to 2 Å is used in recording XRD patterns. When the sample is exposed to this collimated beam of x-rays, (Fig. 2.1) each atom in the lattice planes become the source of a coherently scattered wave that

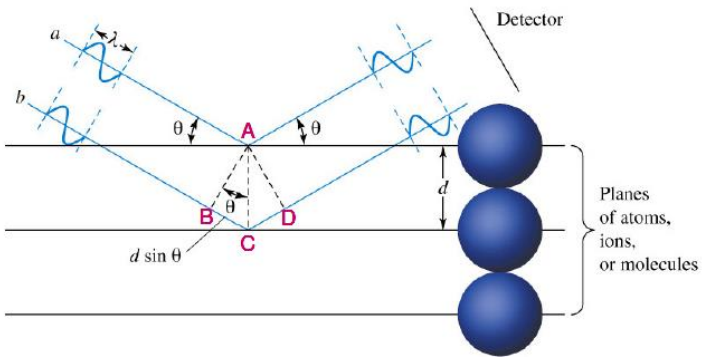

Fig. 2.1 Schematic representation of Bragg's law.

will interfere in a constructive or destructive way with the waves from other surrounding atoms. A diffraction peak is obtained, if the condition of constructive interference from the scattered x-rays by the parallel planes of atoms statifying the Bragg's law which is given by

$$2d_{(hkl)} \sin\theta = n\lambda \tag{2.1}$$

where, $d_{(hkl)}$ is the distance between atomic planes in the crystalline phase, θ is the angle of incidence, λ is the wavelength of the x-ray, and n is the order of the diffraction. The Bragg law is a consequence of the periodicity of the space lattice. This law does not refer to the arrangement or basis of atoms associated with each lattice point. The composition of the basis determines the relative intensity of the various orders "n" of diffraction from given set of parallel planes [114] . Bragg reflection can occur only for wavelengths $\lambda \leq 2d$, since $(n\lambda/2d) \leq 1$ [115].

The Scherrer's formula is commonly used to determine the average crystallite size, D, which is estimated from the peak width [115],

$$D = \frac{K\lambda}{\beta \cos\theta} \tag{2.2}$$

where, D is the average crystallite size, β is the full width of height maxima (FWHM) of a diffraction peak, λ is the wave length of x-ray, θ is the diffraction angle, and K is the Scherrer's constant which is generally equal to unity for usual crystal. In the present work, the value of K is used as 0.94 assuming spherical crystallites.

We used a Rigaku MiniFlex 600 diffractometer for recording the XRD patterns and investigate the crystalline phase/s in the samples. The XRD patterns were collected in the θ-2θ scanning mode (i.e., stationary source, rotating stage, and rotating detector) with CuK_α radiation (λ=1.54 Å) operated at 40 kV and 15 mA. An x-ray beam is incident at an angle θ with respect to the lattice plane of sample and diffracted at an angle 2θ to the incident beam in a typical θ-2θ

scan. The diffracted x-ray intensity is recorded as a function of 2θ. The θ-2θ geometry used in the XRD instrument is shown in the Fig. 2.2.

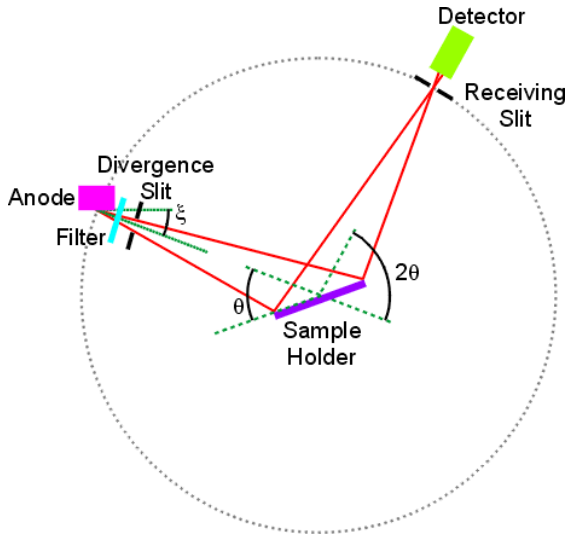

Fig. 2.2 Geometry of x-ray diffraction.

2.2.2 Rietveld Refinement

The powder XRD patterns have severe problem of overlapping peaks arising from different phases and thus need to be fitted with possible phases present in the polycrystalline material to determine the crystal structure, kind and amount of phases. Rietveld analysis was developed to analyze the powder diffraction pattern of the complex compound and of lower symmetry. Hugo Rietveld gave the idea to refine the crystal structure by using the least squares procedure to minimize the difference between the observed and calculated diffraction pattern. Rietveld method is a complex minimization procedure for the structure refinement. A simple representation of the least squares method is shown in Fig. 2.3. The basis of the refinement method are numerical intensities values y_i(obs) at each of several thousand equal steps along the scattering angle 2θ, with the increment $\Delta(2\theta)$, is sought to best least square fit for all the

thousands of y_i(calc) simultaneously. The general form of the quantity to be minimize is given by [116],

$$S = \sum_i w_i (y_i\,(obs) - y_i(calc)^2 = Minimum \tag{2.3}$$

where, w_i is the weight factor, and $y_i(obs)$ and $y_i(calc)$ are the observed and the calculated intensities from the model/s being fitted to the data. The summation index *i* is over all data points and the background is assumed to be subtracted.

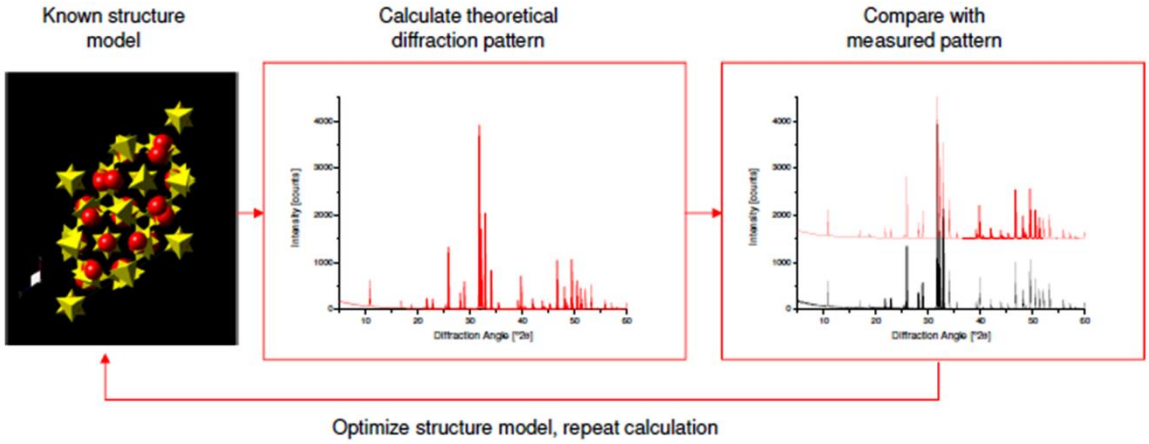

Fig. 2.3 Rietveld refinement method of minimizing the difference between calculated and observed pattern by least squares method.

The lattice parameters and space group can be deduced and refined from the peak positions of reflections. The amorphous fractions in the sample or local order and disorder can be deduced from the background. The particle size, strain/stress and domain size of the sample form analyzing the broadening of the peaks, FWHM, and in the recent development qualitative and quantitative phase analysis [117]. There is a variety of software available for Rietveld structure refinement, such as GSAS, FullProf, Rietica, Reflex, and WinCSD. In present work, the Rietveld refinement of XRD data was performed using GSAS software implemented with EXPGUI interface. The instructions for using GSAS are given in Appendix A.

2.2.3 Electrical conductivity measurement

Van der Pauw technique [118] is a general four point resistivity measurement technique that allows measurements on the samples of arbitrary shape as depicted in Fig. 2.4, as compare to the four-point measurement technique which requires sample of a definite shape. There is no need to

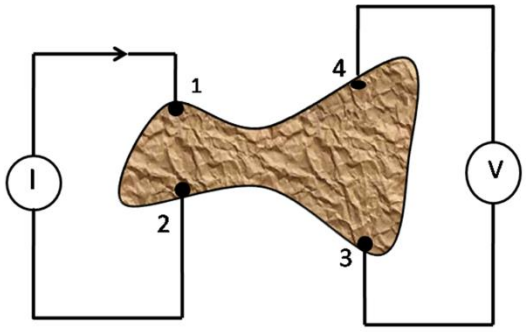

Fig. 2.4 Van der Pauw's method.

measure all the physical dimensions of the sample in van der Pauw technique. However, the contact area of any individual contact should be at least an order of magnitude smaller than the area of the entire sample. In addition to this condition on contact area, there are four general requirements that a sample meet for using this technique: (a) flat shape with uniform thickness, (b) no isolated holes, (c) homogeneous and isotropic, and (d) all four contacts must be located at the edges of the sample.

2.2.4 Scanning electron microscopy (SEM)

The scanning electron microscopy (SEM) uses an electron beam which is generated by either thermionic emission (hot cathode) or field emission (cold cathode) accelerated by a positive voltage of 1 to 30 kV, to generate the image. The use of electron beam allows us to achieve a combination of higher magnification, large depth of focus, and greater resolution. The resolving power of the instrument is given by [113],

$$R = \frac{\lambda}{2NA} \tag{2.4}$$

where, λ is the wavelength of the electron beam and NA is the numerical aperture. Thus, the theoretical limit of resolving power is determined by the wavelength of electron beam used.

The simplicity of examining sample with SEM makes it one of the most widely used instrument for characterization of nanomaterials and nanostructures. The SEM not only produces the topographical information like optical microscope but can also provide the chemical composition information near the surface of the sample.

In an SEM, an electron beam, accelerated toward the sample through evacuated column, is collimated by a condenser lens and focused by an objective lens on the sample. The scan coils are energized by varying voltage produced by the scan generator for creating a magnetic field, which deflect the electron beam back and forth in a controlled manner for raster scanning. Different kinds of signals (i.e. secondary electrons, back scattered electrons, x-ray, and Auger electrons; as shown in Fig. 2.5) are generated, when the beam of electrons interacts with the surface of the sample. These signals are collected and analyzed using different kind of detectors.

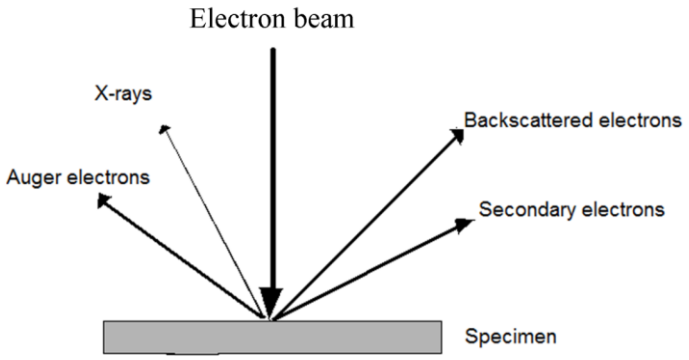

Fig. 2.5 Schematic diagram of electron beam interaction with specimen.

The secondary electrons and the back scattered electrons are used for imaging and x-ray are used for elemental analysis. Typical energy of the secondary electrons is less than 50 eV and can carry

the information to only few angstroms deep in the sample. A scintillator-photomultiplier detector is used to collect these electrons and form the digital image on a computer monitor. These images are commonly used to interpret the morphology of the sample in SEM. In this work, we used a JSM-6610-LV-LGS SEM, operating 15-30 kV, to investigate the morphology and elemental mapping.

2.2.5 Energy dispersive x-ray analysis (EDAX)-elemental composition

EDAX provides a means of identifying the various elements present in the specimen. In this method, when a beam of electron with suitable energy is bombarded on the sample surface, x-rays having characteristic energies of the different elements will be emitted from the sample. Thus, the elemental composition can be determined from the peaks of the corresponding x-ray emission. The x-ray intensity will be compared with the intensities from known samples and quantitative estimation of the composition will be determined with the ratio of the sample x-ray intensity to the x-ray intensity of a sample with known composition. In the present work, an EDAX spectrometer attached to the SEM is used for elemental analysis and mapping.

2.2.5 Transmission electron microscopy (TEM)

The transmission electron microscope is the key tool for imaging the microstructure of the nanoparticles and ultra-thin specimens. The working principle of TEM is very similar to an optical microscope, uses an electron beam instead of light and the wavelength of the electron, according to de Broglie relation, is given by,

$$\lambda = \frac{h}{\sqrt{2meV}} \tag{2.5}$$

where, h is the plank constant, m is the mass of electron, e is the charge of electron and V is the accelerating voltage. Eq. (2.5) is a non-relativistic expression that holds for low accelerating voltages, and the relativistic corrections are made for electrons with energy more than about 100

eV. The accelerating voltage is typically 100-400kV, although a number of specialty TEMs are designed to operate at high voltages ~1 MV. The benefits of higher voltage include increased image resolution, due to decreased electron wavelength and increased penetration depth and thus, study the thicker samples. The electron gun is usually thermionic tungsten or LaB6. However, field emission guns (FEGs) are being used more commonly. There are a number of ways to form the images in TEM: bright field, dark field and high resolution. The bright field image is obtained by using central beam through while blocking the all the diffraction beams. In a similar way, the dark field image is formed by using a single diffracted beam chosen by an aperture that blocks the central beam and other diffracted beams. The high resolution lattice image is formed when primary transmitted beam and one and more diffracted beams are recombined, while keeping both their amplitudes and phase constant, allowing the diffraction planes and arrays of individual atoms to be distinguished [111].

In our study, JEOL 200 TEM (operating at 200 kV) was used to investigate the microstructure of the Li_2FeSiO_4/C nanocomposites.

2.2.7 X-ray photoelectron spectroscopy (XPS)

X-ray photoelectron spectroscopy, also known as electron spectroscopy for chemical analysis (ESCA) is widely-used technique to find the electronic state of atoms as well as ionization energy of atoms. In XPS, when x-rays of known energy strike a solid surface, the electrons are ejected from the atom with kinetic energy via the photoelectric effect. These photoelectrons originate form discrete electronic states of atoms in the analysis volume. The kinetic energy of the emitted photoelectrons is measured by the energy analyzer. The basic process of XPS is shown in Fig. 2.6. According to law of conservation of energy,

$$E_B = hv - E_K - W \tag{2.6}$$

where, E_B is the binding energy of electron, hv is the photon energy, E_K is the kinetic energy of the electron, and W is the spectrometer work function. The binding energy can be calculated from the incident x-ray energy and the kinetic energy E_K of the ejected electron. The value of binding energy of the electron E_B is element specific and corresponds to the oxidation state of that element.

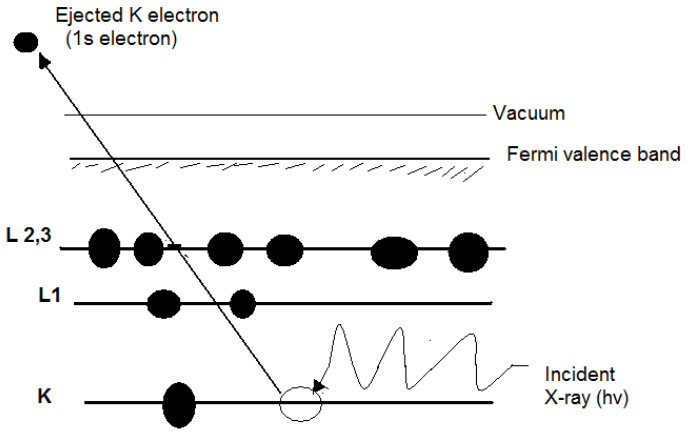

Fig. 2.6 Schematic diagram of the XPS process, showing photoionization of an atom by the ejection of a 1s electron.

In present study, we have used XPS (VG Microtech electron spectrometer equipped with M_g-K_α X-rays as primary source of radiation) to determine the oxidation state of iron and magnesium in Mg doped Li_2FeSiO_4/C samples. The samples were pressed in compact pallets (using a 5 MPa pressure)

2.2.8 Surface area and porosity measurements

In the lithium ion batteries, the mesoporous structure of electrode with large surface area provide large contact area with electrolyte and improves the insertion/extraction process of Li^+ ion during charging and discharge process. The electrochemical properties of the cathode materials depend on the surface area and porosity.

The surface area and characteristic sizes of particles and pore structures are determined by physical and chemical adsorption isotherms, regardless their chemical composition and crystal structure. The gas molecules adsorb onto solid surface to reduce the surface energy under suitable temperature and pressure. The adsorption is either physical or chemical in nature. Physically adsorbed gases can be removed easily by decreasing the partial pressure, however to removal of chemically adsorbed gases requires heating at high temperatures. Physical adsorption is useful to determine the specific area and pore volume for micropores (<2 nm) or mesopores (2 to 50 nm) materials. The amount of gas adsorbed as a function of pressure at certain temperature is called an isotherm. The specific surface area can be evaluated from the monolayer adsorption, if the area of each adsorbed gas molecule is known [113]. The theory to evaluate the surface area of materials was developed by Irving Langmuir, assuming that adsorption gas molecules form a monolayer onto solid surface and gas molecules collides with solid surface inelastically [119]. Braunauer, Emmett, and Teller further developed the Langmuir theory by incorporating the multilayer adsorption of gas, known as BET method. The quantity of gas adsorbed at pressure P is given by

$$V_a = \frac{V_m c P}{(P_o - P)[1+(c-1)\frac{P}{P_o}]} \tag{2.7}$$

where, V_a is quantity of gas adsorbed at pressure P, V_m is quantity of gas adsorbed to form a monolayer, c is a constant and P_o is the saturation pressure of gas. A plot between $P/[V_a(P_o-P)]$ vs P/P_o, yields the straight line and V_m and c are obtained from the intercept and slope. The specific surface area ($m^2 \cdot g^{-1}$) is calculated from the equation given below,

$$S = \frac{4.35\, V_m}{m} \tag{2.8}$$

where, m is the mass of the sample.

BJH method for pore size distributions was developed by Barrett, Joyner, and Halenda on the basis of Kalvin eq. (2.9), which considers pore as cylinders and assume pore filling and evacuating in a stepwise manner[120].

$$In\left(\frac{P}{P_o}\right) = \frac{-2\Upsilon V}{rR_gT} \tag{2.9}$$

where, P is equilibrium vapor pressure, r is the pore radius, P_o is the standard equilibrium pressure, Y, V, R_g, and T are surface tension, molar volume of adsorbate, gas constant, and absolute temperature respectively.

The surface area and pore size distributions for our samples were collected using a Micromeritics Tristar II. The samples are degassed for 10 hours at 150 ^oC under N_2 flow to remove the moisture and other impurities on the surface before the analysis. The isotherms are collected at liquid N_2 temperature (77K). The Brunauer-Emmett-Teller (BET) and Barrett-Joyner-Halenda (BJH) methods were used to calculate the surface area and pore size distribution respectively.

2.3 Electrochemical characterization

2.3.1 Electrode and coin cell fabrication

Electrochemical characterization of the active material in Li-ion battery is crucial to understand its properties and performance of any electrode. The electrochemical characterization of samples was carried out using standard coin cell geometry with lithium metal as an active anode using an MTI Electrochemical Analyzer instrument. The coin cells were prepared by powder method. In the powder method, the active cathode material and Super P as a conducting diluent are mixed in 80:20 ratio and ground for 20 minutes. The homogenous mixture was put on an Al mesh and pressed between two steel cylinders to provide the good adhesion of mixture to Al mesh which acts as current collector. This method of fabrication of electrode has an

advantage for measuring the intrinsic properties of electrode materials without interference from the binder (most often polyvinylidene fluoride (PVDF)), and the effect of binder on the electrochemical properties of active electrode material is eliminated [121]. There are many fundamental studies, such as solid state pellets for in-situ work [122, 123], single particle electrochemistry [124], and thin film produced by sputtering [125] on cathode materials without binder use.

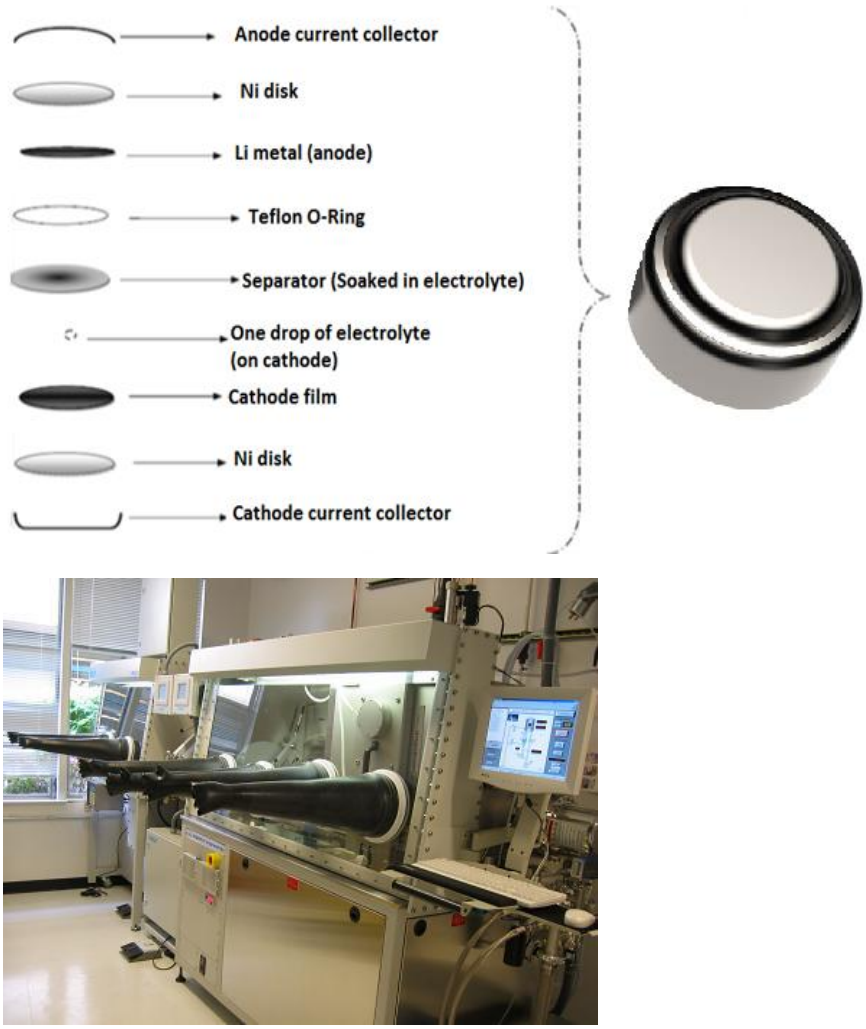

Fig. 2.7 The Schematic diagram of Li-ion coin cell assembly (top) and image of the glove box (bottom).

The cathodes are cycled against Li metal electrode that serves as a counter/reference electrode separated by a polymeric separator (celgard 2400) soaked in binary electrolyte consisting of ethylene carbonate (EC) and dimethyl carbonate (DMC), (50:50) containing 1M $LiPF_6$. Lithium metal is very sensitive to oxygen and moisture and catches fire easily and hence the coin cells are assembled in argon gas filled glove box with oxygen and moisture levels <10.00 ppm and <1.00 ppm. A schematic of coin cell assembly and image of the glove box are shown in Fig. 2.7.

3.2 Electrochemical impedance spectroscopy (EIS)

The electrochemical impedance spectroscopy (EIS) is a powerful technique for investigating the mechanism of electrochemical reactions, measuring the dielectric and transport properties of materials, exploring the properties of porous electrode, and investigating the passive surfaces [126]. This technique is useful in studying the electrochemical system which is in equilibrium or under steady state conditions and is commonly used to study the electrode kinetics and cell resistance. The EIS is based on the application of a sinusoidal voltage (or current) signal to an electrochemical cell. The response of the cell to the sinusoidal perturbation is a sinusoidal current (or voltage), which has the same frequency as the perturbation and is normally shifted in phase. The complex impedance is measured as a function of frequency. EIS measurements were carried out using a Gamry Electrochemical Measurement System (EIS 300) in the frequency range of 0.1-100 kHZ with an AC amplitude of 10 mV. The sweeping frequency in wide range from high to low, allows the reaction steps with different rate constants, such as electrolyte and charge transfer resistances and mass transport (Warburg behavior which is related to diffusion coefficient), to be determined [127]. The impedance values of the cells are influenced by the cycle numbers, cell voltage and cell aging [128, 129].

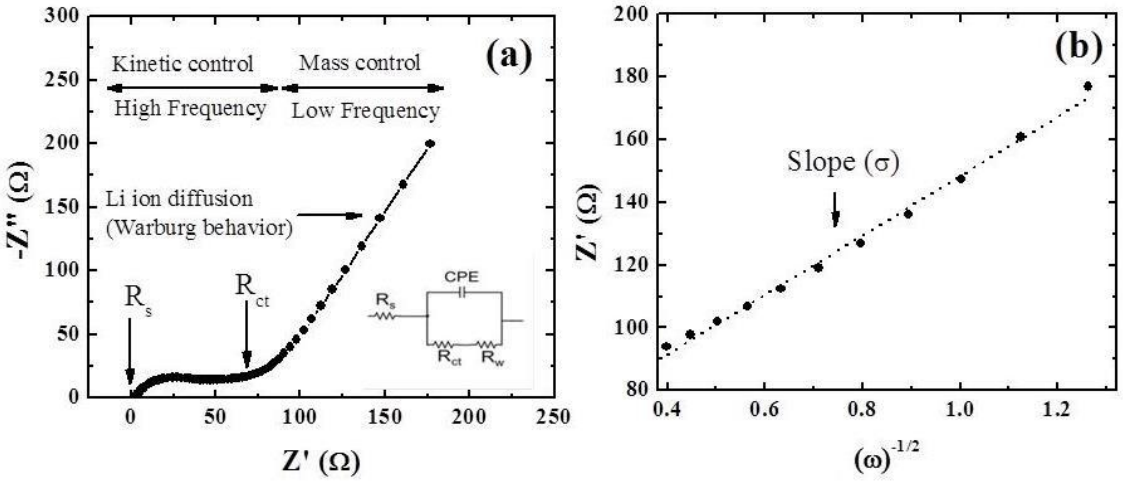

Fig. 2.8 (a) Nyquist plot and (b) plot of Z' versus $\omega^{-1/2}$ in low frequency range for a coin cell of Li_2FeSiO_4/C-SG-600 sample.

Figure 2.8 shows the impedance spectrum (Nyquist plot), a depressed semicircle in the high frequency region and a straight line in the low frequency region for lithium ion battery. In the Nyquist plot, the intercept on the Z′ axis in high frequency region corresponds to the ohmic resistance (R_s) which is the solution resistance, mainly the electrolyte resistance, the semicircle in the middle frequency range is corresponds to the charge transfer resistance, R_{ct} (equivalent to whole diameter of semicircle on the real axis) and the inclined line in the low frequency line is related to the lithium ion diffusion in the cathode materials which is a typical of Warburg behavior [79, 130]. The electrochemical cell impedance spectra can be fitted using Randles equivalent circuit shown as an inset in Fig. 2.8 (a), consisting of a constant phase element representing the double layer and passivation film capacitance [131].

Warburg Analysis

In the low frequency region the frequency dependence of the real part of the impedance (Z') is given by,

$$Z' = R_s + R_{ct} + \sigma\omega^{-1/2} \tag{2.10}$$

where, ω is the angular frequency, R_s is the ohmic resistance, R_{ct} is the charge transfer resistance which is a kinetics parameters and independent of frequency. σ is the Warburg factor which is related to the diffusion coefficient of lithium ion by the following relationship,

$$D = \frac{R^2T^2}{2n^4A^2F^4C^2\sigma^2} \tag{2.11}$$

where, R is the gas constant, T is the absolute temperature, A is the surface area of the cathode, n is the number of electrons per molecule during oxidization, F is the Faraday constant, C is the concentration of lithium ion for an active electrode materials. A plot of Z' versus $\omega^{-1/2}$ (Fig.2.8b), yields a slope σ and the lithium ion diffusion coefficient can be calculated using the Eq. (2.11) [79, 130].

The exchange current density (I_o), which measures the kinetics of electrochemical reaction, can be calculated using [79],

$$I_o = \frac{RT}{nFR_{ct}} \tag{2.12}$$

Cyclic Voltametry

In cyclic voltammetry the applied potential difference is varied linearly with a fixed sweep rate. The sweep rate is reversed once the pre-set values of maximum or the minimum potential difference is reached. During such experiments, the current intensity is registered as function of the potential. Gamry electrochemical system (PHE 200) is used to carry out the CV measurements in our work.

Cyclic voltammetry is a common technique to study the electrochemical system and gives the information about the kinetics and thermodynamics of electrode redox reactions, including the Faradaic insertion and extraction reactions [127, 132].

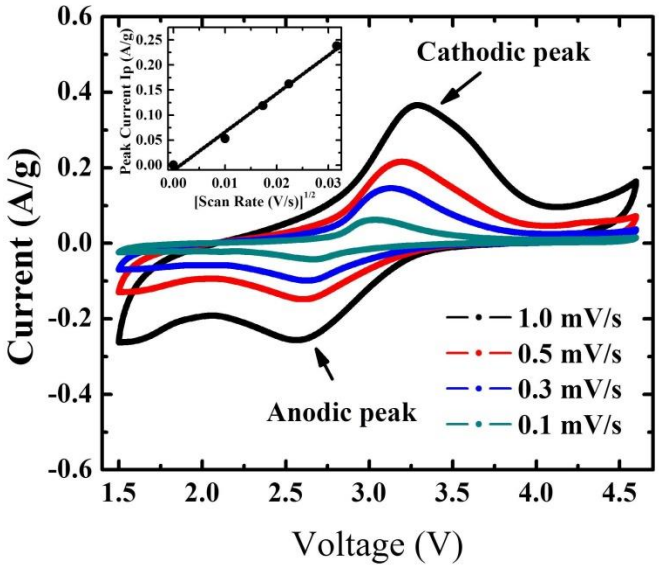

Fig. 2.9 CV plot at different scan rates for a coin cell of Li_2FeSiO_4/C-SG-600 sample. The inset shows a plot of the peak current versus square root of scan rate.

A cyclic voltammogram at different scan rates for a coin cell is shown in the Fig. 2.9, indicating the cathodic and anodic peak currents and voltages. The Li diffusion coefficients for an electrode are calculated using the Randles Sevcik equation, which describes the effect of scan rate on the peak current. In a linear potential sweep voltammogram, the relation between the peak current and the scan rate (for low scan rates) is given by,

$$i_p = 0.4463F\left(\frac{F}{RT}\right)^{\frac{1}{2}} C^* v^{\frac{1}{2}} AD^{\frac{1}{2}} \qquad (2.13)$$

where, i_p is the peak current, F is the Faraday's constant (96500 C·mol^{-1}), R is the gas constant (8.32 J K^{-1}·mol^{-1}), T is the temperature (298.15 K), C^* is the initial Li ion concentration for active electrode material, A is the electrode area, v is the scan rate, and D is the lithium diffusion coefficient. A plot of the peak current versus square root of scan rate for a coin cell is shown in the inset of Fig. 2.9.

2.3.3 Galvanostatic charge/discharge cycles

Galvanostatic charge/discharge or chronopotentiometry is widely used technique to test the electrochemical cell. In this technique, a constant current is applied to the working electrode (cathode) during charging and the potential is registered against the reference electrode (lithium metal) as function of the time or total charge passing through the system. The direction of current is reversed during discharging once the pre-set maximum potential difference is reached. The shape of such curves is related to the reaction mechanism, transport of the reactants from the bulk phase to the interface, and transport of the product in the opposite direction. In a battery system nC is the charge/discharge rate at which battery is fully charge/discharge for 1/n hour. The specific capacity per unit mass can be determined at a specific C rate from the charge transfer during discharging or charging process in term of $C \cdot g^{-1}$ or $mAh \cdot g^{-1}$. The specific capacity is measured at different C rates to evaluate the rate capability of the cell [127].

In present work, room temperature galvanostatic charge/discharge measurements were performed using an MTI Electrochemical Analyzer System at different current densities within the voltage range of 1.5 to 4.5 V versus lithium reference electrode.

CHAPTER 3 IMPROVED ELECTROCHEMICAL PROPERTIES OF SOLVOTHERMALLY SYNTHESIZED Li_2FeSiO_4/C NANOCOMPOSITES: A COMPARISON BETWEEN SOLVOTHERMAL AND SOL-GEL METHODS

In this chapter, we describe the synthesis of porous Li_2FeSiO_4/C nanocomposites by two different routes such as sol-gel (SG) and solvothermal (ST) using block copolymer pluronic (P123) and present their electrochemical properties. A comparative study of their structural, electrical and electrochemical properties was studied and the effect of annealing temperture on electrochemical performances was also invetigated. The present study shows that solvothermal synthesis of Li_2FeSiO_4/C nanocomposites using P123 as a carbon source is an effective method for improving its electrochemical properties.

3.1 Introduction

As discussed in Chapter 1, rechargeable lithium ion batteries (LIBs) are a key technology in the present energy scenario in addressing the global energy requirements. Apart from small scale applications in portable electronics, LIBs have the potential for applications in hybrid electric vehicles and renewable power stations as intermediate energy storage devices. For LIBs, cathode materials with large energy density, high safety and low cost are highly desired. Even though Li-based oxide materials such as $LiCoO_2$, $LiNiO_2$ and $LiMn_2O_4$ are currently used as cathode materials, there is a great demand for safe and low-cost alternatives to these conventional materials as they pose safety risks due to the release of activated oxygen or structural instability when they are heavily charged [2, 38, 106]. New compounds containing $(XO_4)^{n-}$ polyanions [133], like, $LiMPO_4$ and Li_2MSiO_4 (M = Mn, Fe) are being studied and proposed as cathode materials due to their high thermal stability owing to their strong X-O covalent bond and also due to less release of activated oxygen. Though Li_2FeSiO_4 has been considered as a cathode material with great potential for use in the next generation LIBs by virtue of its high specific

theoretical capacity (330 $mAh \cdot g^{-1}$), low cost, good cycle performance and eco-friendliness [61, 100, 106, 134, 135], its application is still plagued by its poor electronic and ionic conductivities and low lithium ion diffusion coefficient [98, 104, 136]. Some of the strategies proposed to overcome these limitations are: coating the material with carbon [70, 101], doping with hetero-atoms [88, 91, 94, 137-139], and scaling of Li_2FeSiO_4 particle size to nanoregime [54, 70, 140].

The carbon coating using surfactants or polymers is one of the most simple and common methods to enhance electronic conductivity and hence the electrochemical performance of Li_2FeSiO_4 [60-65]. Nanostructured Li_2FeSiO_4/C cathode material was successfully synthesized by Du *et. al. [141]* by co-precipitation method using Fe^{3+} salt as iron source and polyethylene glycol as surfactant. The improved electrochemical performance has been attributed to fast transport of electron and lithium ion due to the formation of nanocrystals of Li_2FeSiO_4 with in-situ formed carbon network. Reducing the cathode material to nanoscale with large surface area is known to decrease the Li ion diffusion path length [142]. Preparation of hierarchically structured morphologies, such as mesoporous structure, is another effective approach for improving the electrochemical properties [142, 143]. It is known that solvothermal treatment plays a key role in controlling the crystallite size of the Li_2FeSiO_4 particles and to form the porous structure [138].

The Poly(ethylene glycol)-block-poly(propylene glycol)-block-poly(ethylene glycol) tri-block copolymer P123 ($EO_{20}PO_{70}EO_{20}$) is used to provide the carbon coating and also to make meso-porous structures of Li_2FeSiO_4 [60-65]. In the work, we have synthesized the porous Li_2FeSiO_4/C nanocomposites by sol-gel and solvothermal methods with tri-block copolymer P123 as an *in situ* carbon source and a structure directing agent, and compare their structural and electrochemical properties. The composites synthesized by solvothermal method (Li_2FeSiO_4/C-

ST) show better electrochemical performance compared to the sol-gel prepared composites (Li_2FeSiO_4/C-SG). We believe that uniform carbon coating of particles, formed by the *in situ* combustion of the surfactant during the heating process, increases the electronic conductivity, and limits the particle growth leading to production of porous Li_2FeSiO_4/C nanoparticles. Further, the reduction of particle size to nanometers (~15 nm) shortens the lithium ion diffusion length and thereby improves the electrochemical performance of the material. Cyclic voltammetry and electrochemical impedance spectroscopy are used to understand the lithium diffusion process.

3.2 Materials and methods

Li_2FeSiO_4/C was synthesized by two different methods: sol-gel and solvothermal. All chemicals used in the synthesis were procured from Sigma-Aldrich and were used without further purification. In a typical synthesis of Li_2FeSiO_4/C by the sol-gel method, lithium acetate (1.0202 g), ferric nitrate (2.02 g), silicon acetate (1.32 g), and P123 (1 g) were dissolved separately in ~20 ml of absolute ethanol and then transferred to a three neck flask to form precursor solution. The whole precursor solution was stirred overnight under nitrogen gas flow to form a gel which was subsequently dried by heating at 100 ^oC for 24 hours. The dried powder was ground well with a mortar and pestle and heated at 600 ^oC for 9 hour under argon flow. Samples heated to 650 ^oC and 700 ^oC were also prepared in a similar way. In the solvothermal method of synthesis, the precursor solution was obtained by using similar method followed for sol-gel process. The precursor solution was sealed in Teflon lined stainless steel autoclave and heated at 140 ^oC for 24 hour after which it was cooled to room temperature, and the product was poured into a beaker and excess solvent was evaporated by heating at 100 ^oC on a hot plate to

obtain the dried powder. The powder was finely ground and heated in argon flow at the same temperature and duration used in preparing the sol-gel samples.

3.3 Results and discussion

3.3.1 Structural Analysis (XRD)

The XRD patterns of Li_2FeSiO_4/C nanocomposites studied in this work are shown in Fig. 3.1. No evidence of any secondary phase is observed in samples heated at 600 and 650 ^oC for 9 h. However, a weak diffraction peak at ~44.8^o due to the presence of small amount of Fe metal is observed in the XRD pattern of 700 ^oC (9h) annealed samples, synthesized by both sol-gel and solvothermal methods. This may be due to reducing nature of polymer P123 at high temperature. XRD profiles of all heated samples are in full accord with the Li_2FeSiO_4 structure indexed to monoclinic $P2_1/n$ phase in agreement with previous reports [48, 144].

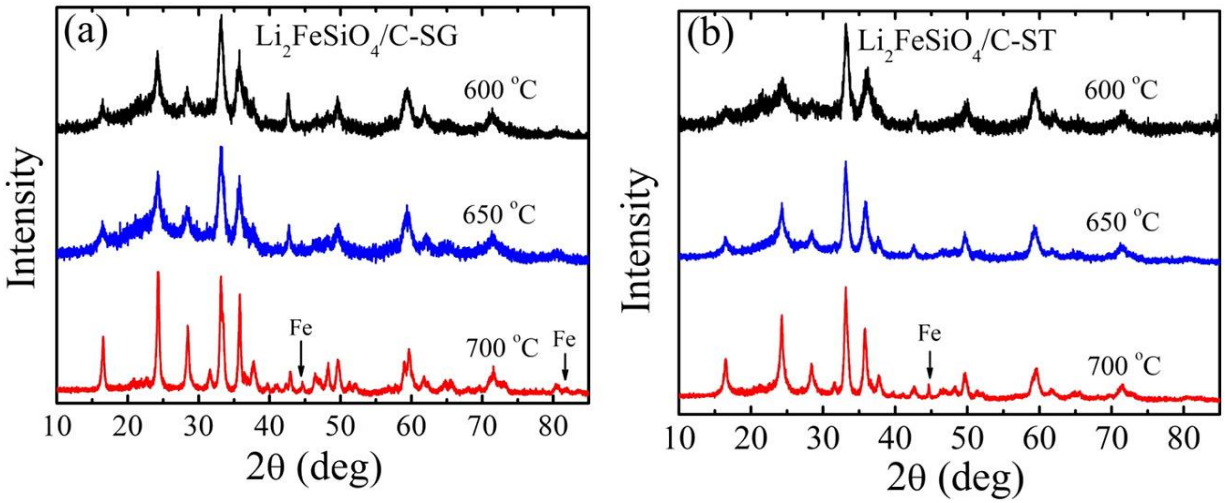

Fig. 3.1 XRD patterns of (a) Li_2FeSiO_4/C (Sol-gel, SG), and (b) Li_2FeSiO_4/C (Solvothermal, ST) annealed for 9 hours at different temperatures.

The broad XRD peaks clearly indicate that the samples are nanocrystalline in nature. The average crystallite size was calculated using Scherer equation $D = \kappa\lambda / \beta\cos\theta$. The Li_2FeSiO_4/C samples synthesized by sol-gel and solvothermal methods, after heating at 600 ^oC for 9 h

(henceforth written as Li_2FeSiO_4/C-SG-600 and Li_2FeSiO_4/C-ST-600) showed average crystallite size of ~ 20 and 15 nm, respectively, which increased on heating at 650 and 700 ^oC for 9 h. While the 650 and 700 ^oC heated samples synthesized by sol-gel method showed 24 and 28 nm in size, the solvothermally synthesized samples heated at the same temperature showed 18 and 23 nm, respectively.

3.3.2 Carbon content determination and conductivity measurements

The average carbon content, determined by CHN analysis, was found to be ~15 wt% in all the samples. It is interesting to note that the room temperature electrical conductivity measured on the pressed pellets of the above samples showed very similar value ~ low 10^{-4} $S{\cdot}cm^{-1}$, which is several orders of magnitude higher than that of bulk Li_2FeSiO_4 [145], due to the presence of interconnected residual carbon.

3.3.3 Morphology and Microstructure

Figure 3.2 shows the SEM and TEM images of the composite samples. The SEM images

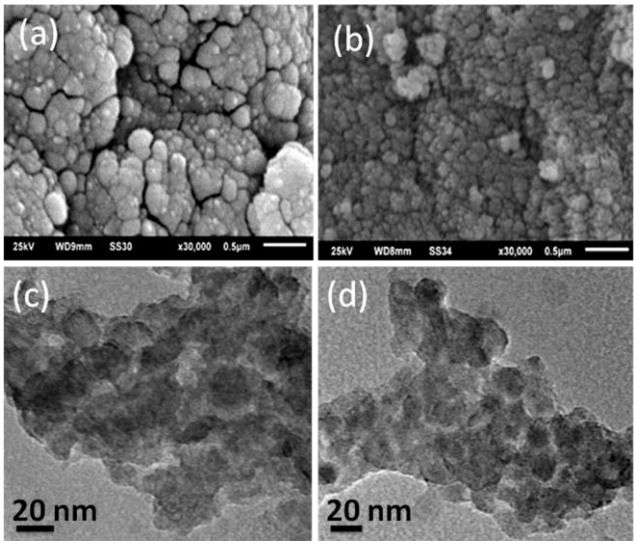

Fig. 3.2 SEM images of (a) Li_2FeSiO_4/C-SG-600, (b) Li_2FeSiO_4/C-ST-600, and TEM images of (c) Li_2FeSiO_4/C-SG-600 and (d) Li_2FeSiO_4/C-ST-600 samples.

show that Li_2FeSiO_4/C-SG-600 sample has large agglomerations of nanoparticles with irregular shaped grains compared to nearly uniform spherical grains in Li_2FeSiO_4/C-ST-600 sample. The microstructures of the composites studied by TEM images, displayed in the Figs. 3.2(c) and (d) show nanosized particles (consistent with XRD results) in intimate contact with each other and embedded in carbon matrix.

3.3.4 Specific surface area and pore size

To study the porous nature of samples, N_2 adsorption–desorption isotherms were recorded at liquid nitrogen temperature (77 K) which are shown in Fig. 3.3. The measured BET surface areas for Li_2FeSiO_4/C-SG-600 and Li_2FeSiO_4/C-ST-600 samples are 56 $m^2 \cdot g^{-1}$ and 99 $m^2 \cdot g^{-1}$, and the corresponding average pore size was 5.9 nm and 6.3 nm, respectively. Clearly, the solvothermal synthesis of Li_2FeSiO_4/C nanocomposites, using P123 as a carbon source, produces highly porous material with a large surface area.

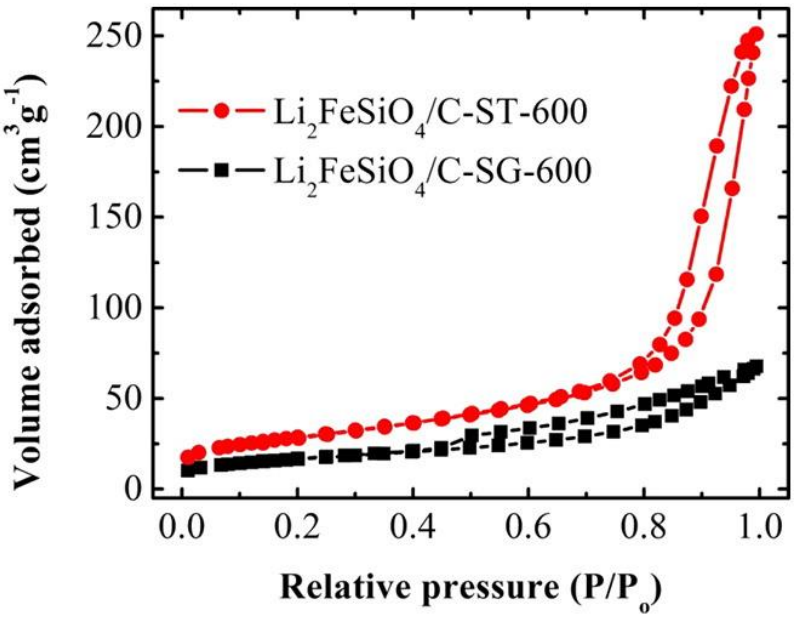

Fig. 3.3 N_2 adsorption/desorption isotherms of Li_2FeSiO_4/C-SG-600 and Li_2FeSiO_4/C-ST-600 composites.

3.4 Electrochemical Measurements

3.4.1 Glavanostatic Charge/discharge

As the XRD patterns of 700 ^{o}C heated samples, synthesized by both the methods, showed the presence of a small amount of iron impurities, we studied the electrochemical properties of 600 ^{o}C and 650 ^{o}C annealed samples only. A typical charge/discharge profile obtained for Li_2FeSiO_4/C-ST-600 is shown in Fig. 3.4. The charge/discharge profiles are investigated in the potential window of 1.5-4.6 V vs. Li/Li^+ at a rate of C/30. The charge profile of first cycle exhibits two voltage plateaus; the first one appearing at ~3.2 V, which corresponds to the Fe^{2+}/Fe^{3+} redox couple and the second one at ~4.3 V, which is attributed to the combined

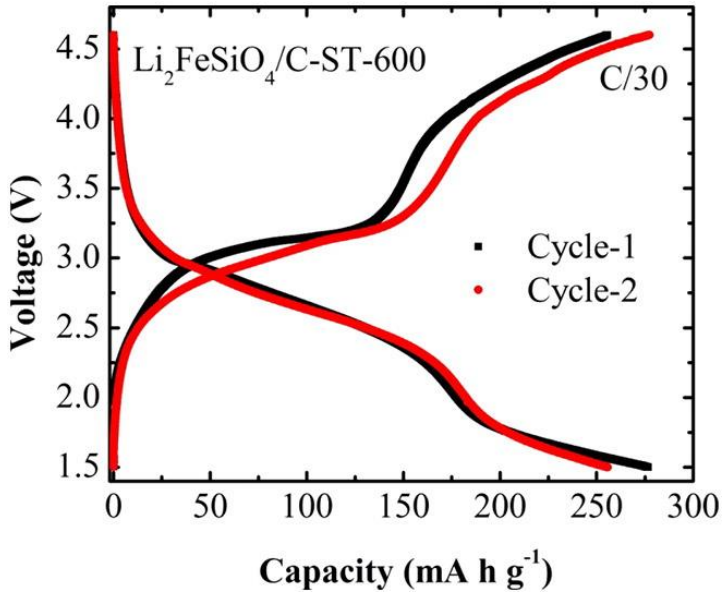

Fig. 3.4 A typical charge/discharge profile of Li_2FeSiO_4/C-ST-600 at C/30 rate.

capacitive effect of nano size material and the charge storage due to oxo-peroxo behavior of the metal-oxygen ligand, as a large hysteresis is observed in corresponding discharge profile at low voltage. Participation of the lattice oxygen in charge storage has also been predicted by the first principle calculation for some cathode materials [146, 147]. The contribution of lattice oxygen in redox process has been clearly identified recently using electron paramagnetic resonance

measurements [148, 149]. The reversible oxo-peroxo redox process may have oxidation potential above 4.3 V with a wide hysteresis for its reduction process. The contribution of lattice oxygen in charge storage and its effect on voltage and capacity of cathode materials has been introduced by Rouxel's novel concept of "ligand-hole-chemistry" [150] similar to Goodenough's idea of inductive ligand effect for polyanion cathodes [40]. The degree of covalency of the metal-ligand due to repulsion of d-d and the group electronegativity of the oxo-anion contribute to the participation of oxo (O^{2-})-peroxo $(O\text{-}O)^{-}$ in the charge storage during oxidation (charging). The upper charge plateau around 4.3 V could be the direct result of the oxo-peroxo oxidation process, which is caused by the mixing of the empty d- band of the Fe^{3+} and filled valence band of the oxygen O^{2-}. This excess capacity due to anion redox mechanism has provided the initial discharge capacity of ~276 mAh·g^{-1} for Li_2FeSiO_4/C-ST-600 in the first cycle which is about 84% of the theoretical capacity.

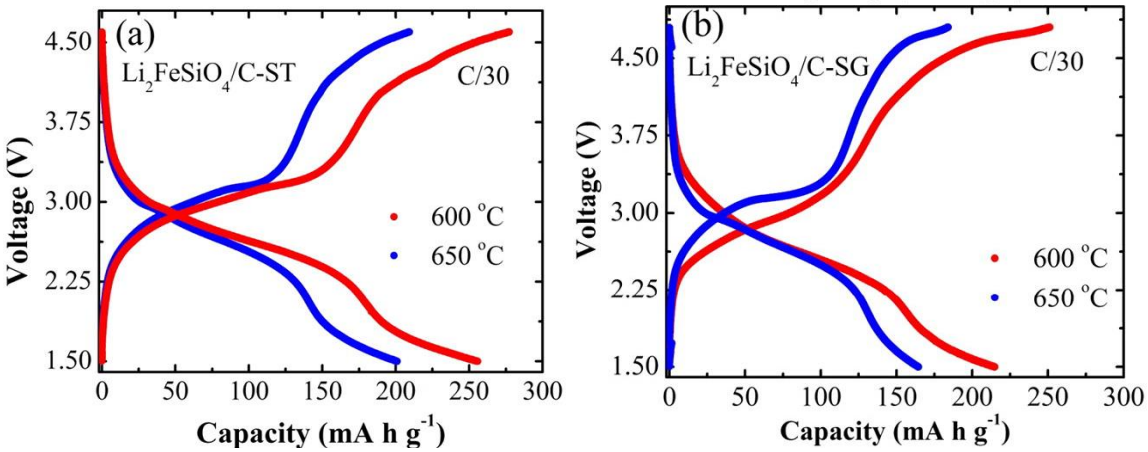

Fig. 3.5 The second cycle of charge/discharge profiles of (a) Li_2FeSiO_4/C-ST annealed at 600 °C and 650 °C, and (b) Li_2FeSiO_4/C-SG annealed at 600 °C and 650 °C.

In the second cycle, the discharge capacity is reduced by 20 mAh·g^{-1} from the first cycle and reached ~256 mAh·g^{-1}. In addition, it is clear from the charge/discharge curves that the first and second plateaus in the second cycle appear at a lower voltage compared to the plateaus observed

in the first charge/discharge cycle. This observation can be attributed to a Li/Fe antisite exchange process during the initial charging [144].

The Li_2FeSiO_4/C-SG-600 sample showed a discharge capacity of ~235 mAh·g^{-1} in its first cycle (figure not shown). Figures 3.5(a) and (b) compare the charge/discharge profiles for the second cycle of Li_2FeSiO_4/C, prepared by both solvothermal and sol-gel methods and annealed at 600 ^oC and 650 ^oC. The discharge capacities for solvothermally prepared Li_2FeSiO_4/C-ST composites are ~256 and ~200 mAh·g^{-1}, respectively, at C/30 and the corresponding values for the sol-gel prepared Li_2FeSiO_4/C-SG composites are ~215 and ~164 mAh·g^{-1}. The Li_2FeSiO_4/C-ST-600 showed better electrochemical performance among all the composites studied in this work, which we attribute to its smaller crystallite size and higher porosity.

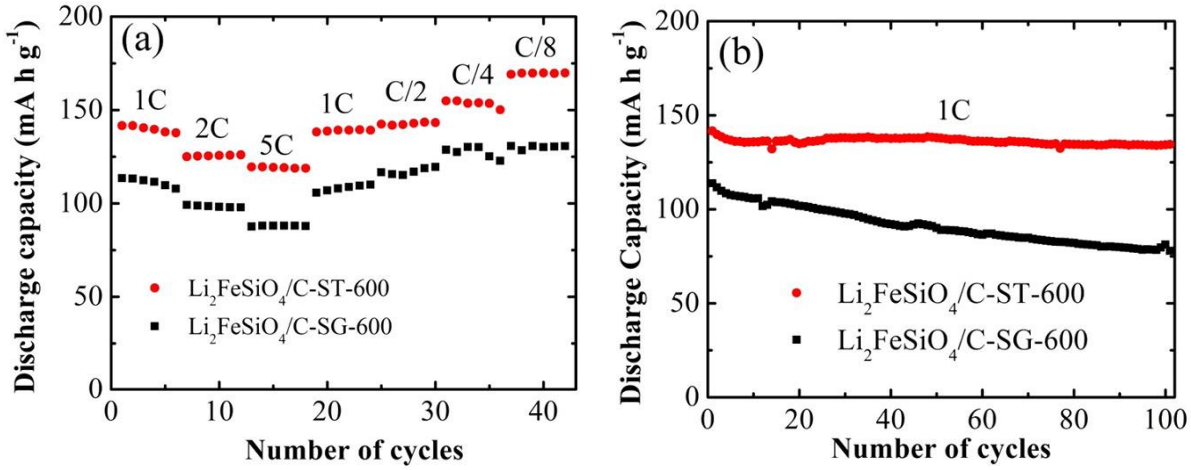

Fig. 3.6 (a) The rate capability of Li_2FeSiO_4/C-ST-600 and Li_2FeSiO_4/C-SG-600 samples and (b) Stability curve of Li_2FeSiO_4/C-SG-600 and Li_2FeSiO_4/C-ST-600 samples at 1C rate.

The cycling performance of Li_2FeSiO_4/C-ST-600 and Li_2FeSiO_4/C-SG-600 at different rates is shown in Fig. 3.6(a). The Li_2FeSiO_4/C-ST-600 sample delivered an average discharge capacity of 141, 125, 120, 139, 143, 154, and 170 mA h·g^{-1} at 1C, 2C, 5C, 1C, C/2, C/4, and C/8, respectively, whereas the Li_2FeSiO_4/C-SG-600 sample delivered a decreased average discharge

capacity of 112, 99, 90, 108, 116, 128, and 130 $mAh \cdot g^{-1}$ at the same rates. The cycling stability curves measured at 1C are shown in Fig. 3.6(b) for the above two samples. It is clearly seen that the Li_2FeSiO_4/C-ST-600 exhibits stable cycle life, retaining 95% of its initial discharge capacity after 100 cycles, compared to Li_2FeSiO_4/C-SG-600 with only 68% of its initial discharge capacity after the same number of cycles. It is interesting to note that the discharge capacities observed for Li_2FeSiO_4/C-ST-600 sample at various rates are comparable to the recently published data on Mg-doped Li_2FeSiO_4/C composites by Qu *et. al.* [88], where the authors have clearly demonstrated that Mg-doping can further help to decrease the charge-transfer resistance and increase Li-ion diffusion capability compared to Li_2FeSiO_4/C without doping.

3.4.2 Cyclic Voltammetery

To further investigate the enhancement in electrochemical performance of Li_2FeSiO_4/C-ST-600 compared to Li_2FeSiO_4/C-SG-600, we conducted the cyclic voltammetry and electrochemical impedance spectroscopy measurements. The I-V plots for Li_2FeSiO_4/C-ST-600 and Li_2FeSiO_4/C-SG-600^oC samples at different rates in the range of 0.1-10 mV/s are shown in Figs. 3.7 (a), and (b). The I-V plots for Li_2FeSiO_4/C-SG-600 and Li_2FeSiO_4/C-ST-600 at a scan rate of 0.1 mV/s are compared in Fig. 3.7c. The first oxidation peak seen at ~3.1 V in Li_2FeSiO_4/C-ST-600 corresponds to the first electron transfer in the electrochemical reaction, in which Fe^{2+} is oxidized to Fe^{3+}. The second oxidation peak observed at ~4.2 V corresponds to the second electron transfer, in which anion redox process and capacitive effect of nano-size cathode occur. However, at the same scan rate, for Li_2FeSiO_4/C-SG-600 sample the first oxidation peak is seen at 3 V and the second oxidation peak is hardly visible. Further, it may be noted that the peak is sharper and more intense for Li_2FeSiO_4/C-ST-600 sample compared to Li_2FeSiO_4/C-SG-600, indicating faster kinetics for the former sample.

The Li diffusion coefficients for Li_2FeSiO_4/C-ST-600 and Li_2FeSiO_4/C-SG-600 are calculated using the Randles-Sevcik equation (Eq. (2.13) which describes the effect of scan rate on the peak current. A plot of the peak current versus square root of scan rate for Li_2FeSiO_4/C-ST-600 and Li_2FeSiO_4/C-SG-600 is shown in Fig. 3.7 (d) and the calculated lithium diffusion coefficients using Eq. (2.13) for Li_2FeSiO_4/C-ST-600 and Li_2FeSiO_4/C-SG-600 are 1.2×10^{-11} cm^2/s and 9.2×10^{-12} cm^2/s, respectively.

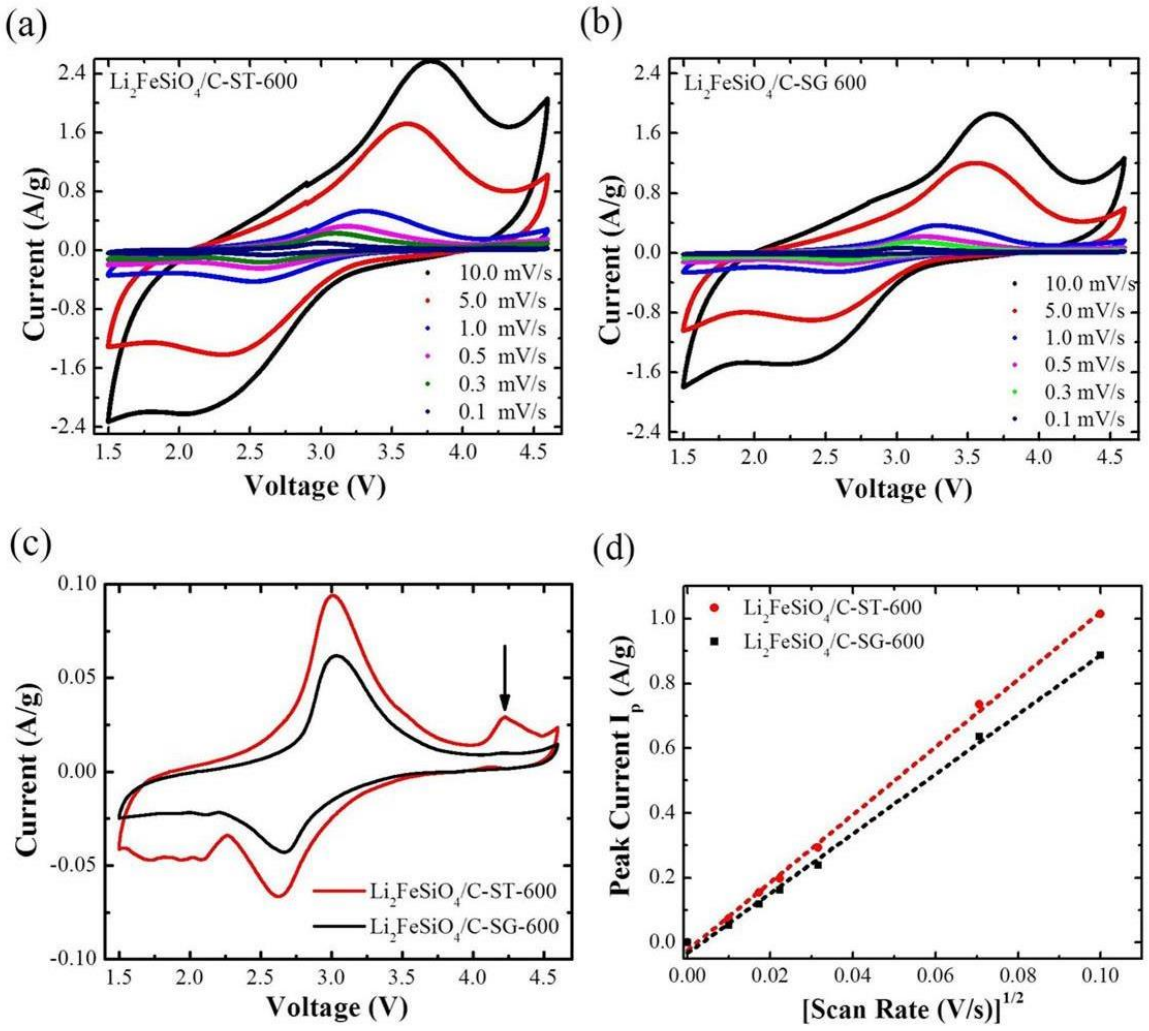

Fig. 3.7 I-V plots of (a) Li_2FeSiO_4/C (ST-600^{o}C-9h), (b) Li_2FeSiO_4/C (SG-600^{o}C-9h) at different scan rates, (c) A comparison of I-V plots of Li_2FeSiO_4/C-ST-600 and Li_2FeSiO_4/C-SG-600 samples at 0.1 mV/s scan rate. The arrow points to the second oxidation peak corresponding to the second electron transfer, and (d) Randles-sevcik plots of the normalized peak current (I_p) as a function of square root of scan rate.

3.4.3 Electrochemical impedance spectroscopy

Figure 3.8 (a) shows the Nyquist plots of the coin cells prepared with Li_2FeSiO_4/C-ST-600 and Li_2FeSiO_4/C-SG-600 samples. The impedance spectra show a typical depressed semicircle in the high frequency region and a straight line in the low frequency region for the freshly prepared coin cells. In the Nyquist plot, the intercept on the Z' axis in high frequency region corresponds to the ohmic resistance (R_s) which is the resistance between the working electrode and the counter/reference electrode, mainly the electrolyte resistance. The inclined line in the low frequency region is related to the lithium ion diffusion in the cathode material which is a typical of Warburg behavior. The other intercept of depressed semicircle corresponds to the charge transfer resistance, R_{ct}.

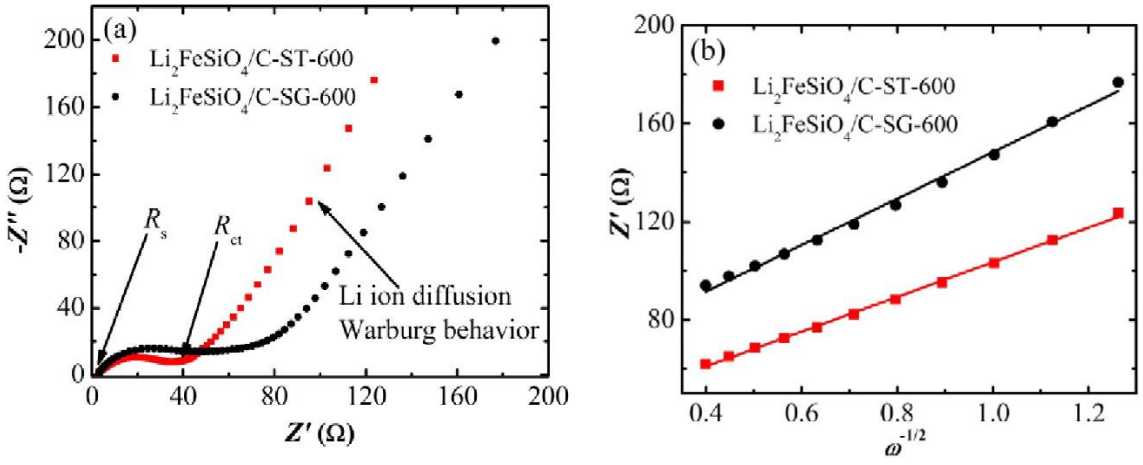

Fig. 3.8 (a) Nyquist plots and (b) graph of Z' v. $\omega^{-1/2}$ in the low frequency range for the coin cell of $Li_2FeSiO4$/C-ST-600 and Li_2FeSiO_4/C-SG-600 samples.

In the low frequency region, the frequency dependence of the real part of the impedance (Z') is linearly related to the square root of angular frequency and the plots Z' versus $\omega^{-1/2}$ yield slope (σ) which is related to the lithium ion diffusion coefficient can be calculated using Eq. (2.11) [88]. Figure 3.8 (b) compares the linear plots of Z' versus $\omega^{-1/2}$ for the two samples. From the intercept, we found a lower value of R_{ct} ~ 30 Ω for Li_2FeSiO_4/C-ST-600 compared to ~ 53 Ω for

Li_2FeSiO_4/C-SG-600, and the corresponding values of Li-ion diffusion coefficient are 5.5×10^{-14} $cm^2\cdot s^{-1}$ and 3.1×10^{-14} $cm^2\cdot s^{-1}$. The former sample, which has a higher diffusion coefficient and lower charge transfer resistance, showed enhanced electrochemical performance, which we attribute to its reduced particle size and high porosity. The observed values of the Li-ion diffusion coefficient determined here is an order of magnitude higher than that recently reported values by Qu *et. al.* [88] for undoped and Mg-doped Li_2FeSiO_4/C composites.

In the nanocomposites investigated in this work, the porous structures are formed due to solvothermal treatment, and the high temperature calcination of the samples with polymer P123. The high temperature heating causes the release of gases from the sample-polymer mixture because of the decomposition of the organic polymer matrix. This evolution of gases creates porous structure, and forms thin carbon coating around Li_2FeSiO_4 nanoparticles. The carbon coating of Li_2FeSiO_4 particles hinders their agglomeration leading to smaller grains and provides an effective conducting path for electron thus facilitating a faster electron and Li^+ ion transport due to decreased lithium ion diffusion length. Further, nano-sized mesoporous structure of the composites increases the contact area between the electrolyte and the cathode resulting in improved insertion/extraction of Li^+ during the charge/discharge cycles leading to enhanced electrochemical performance of the composites. We note that the Li_2FeSiO_4/C-ST-600 nanocomposite has a smaller average particle size (~15 nm), larger BET surface area (99 $m^2\cdot g^{-1}$) and porosity (6.3 nm), compared to that of Li_2FeSiO_4/C-SG-600 (~ 20 nm, 56 $m^2\cdot g^{-1}$ and 5.9 nm, respectively). The Li_2FeSiO_4/C samples prepared by solvothermal method in this study show improved specific capacity and rate performance compared to several studies reported in the literature [78, 79, 87, 90, 94, 96, 138, 151] which can be attributed to the combined effect of

large surface area, smaller particle size, large porosity and effective carbon coating of the crystallites.

3.5 Conclusions

In summary, we have synthesized nanoparticles of porous Li_2FeSiO_4/C composites by sol-gel and solvothermal methods using tri-block copolymer (P123) as both carbon source and surfactant and compared their structural, morphological and electrochemical properties. The heating of the Li_2FeSiO_4- polymer (P123) composite at high temperature creates porous Li_2FeSiO_4 /C cathode materials with uniform carbon coating which improves the electron mobility leading to improved electrochemical properties. At room temperature, 600 ^oC heated (9 h) Li_2FeSiO_4/C-prepared by solvothermal method showed improved discharge capacity of ~276 $mAh \cdot g^{-1}$ at C/30 rate, cycled between 1.5 and 4.6 V compared to Li_2FeSiO_4/C synthesized by sol-gel method. At 1C rate, Li_2FeSiO_4/C-ST-600 showed better stability over 100 cycles compared to Li_2FeSiO_4/C-SG-600. The enhanced electrochemical properties shown by the solvothermally synthesized Li_2FeSiO_4/C nanocomposites are attributed to the smaller particle size, large surface area and large porosity leading to an increased contact area between the electrolyte and electrode. This shortened the lithium ion diffusion path length enhancing the electrochemical performance of Li_2FeSiO_4/C-ST nanoparticles. Based on the above results, we conclude that preparation of Li_2FeSiO_4/C by solvothermal method seems be an effective way to improve its electrochemical performances of Li_2FeSiO_4.

CHAPTER 4 Mg DOPED Li_2FeSiO_4/C NANO-COMPOSITES SYNTHESIZED BY SOLVOTHERMAL METHOD FOR LITHIUM ION BATTERIES

In this Chapter, the effects of the Mg doping on structural and electrochemical performance of Li_2FeSiO_4/C nanocomposites are presented in the results of our investigations. A series of porous $Li_2Fe_{1-x}Mg_xSiO_4$/C (x = 0, 0.01, 0.02, 0.04, labeled as LFS/C, 1Mg-LFS/C, 2Mg-LFS and 4Mg-LFS/C, respectively) nanocomposites have been synthesized via a solvothermal method using pluronic P123 polymer as in situ carbon source. Structure, morphology and electrochemical performance of these composites were investigated using a number of techniques. The results show that 1Mg-LFS/C exhibits the best rate capability and cycle stability (94% retention after 100 charge-discharge cycles at 1C) and also delivered the highest initial discharge capacity of 278 $mAh{\cdot}g^{-1}$ (~84% of the theoretical capacity), despite having same percentage of carbon content (~ 15%) in all the Mg doped LFS/C composites. The electrochemical properties of 1Mg-LFS/C composite studied in this work is found to be much better compared to other Mg doped Li_2FeSiO_4 studies reported in the literature.

4.1 Introduction

In the Chapter 3, the improved electrochemical performance of Li_2FeSiO_4 was demonstrated with carbon coating using pluronic P123 polymer. It was shown that in situ carbon coating of particles prevents the growth of larger particles during calcination, and thereby improves the electrochemical performance due to increased conductivity and shortened Li^+ diffusion path length. Doping with supervalent cations is another effective way to improve the electronic conductivity in polyanion cathode materials. Mg doping in phosphates based cathode materials such as $LiFePO_4$ and $Li_3V_2(PO_4)_3$ is found to improve their electrochemical performance due to

shorter Li^+ diffusion path length and decreased charge-transfer resistance during the lithiation-delithiation process [152-156]. Expecting a similar behavior, Mg doped LFS have been studied by some research groups [87, 88]. However, Mg-doped (x=0.03) Li_2FeSiO_4/C composites synthesized using sol-gel method have not shown distinct improvements in specific capacity (153 $mAh{\cdot}g^{-1}$) at a discharge rate of C/16 but showed better performance at a higher of 2C, compared to un-doped material [87]. Qu *et. al.* [88] have shown that Mg-doped (x=0.02) Li_2FeSiO_4/C synthesized by sol-gel method can deliver discharge capacity of 190 $mAh{\cdot}g^{-1}$ at 0.1C rate, and it retains 96% of its capacity after 100 charge-discharge cycles. They attributed the observed improvement to decreased charge-transfer resistance and increased Li-ion diffusion coefficient in Li_2FeSiO_4/C brought about by Mg doping. In both studies the authors showed that Mg doping stabilizes the crystal structure which results in higher cycle stability compared to un-doped material.

The above mentioned reports by various authors show the electrochemical performance of Li_2FeSiO_4 based materials depends on many parameters that can be controlled by synthesis method, such as, carbon coating and by Mg doping. Considering this, we have synthesized a series of *in situ* carbon coated, porous $Li_2Fe_{1-x}Mg_xSiO_4$/C (x = 0, 0.01, 0.02, 0.04) nanocomposites by a solvothermal method. This method produces very fine nanoparticles (< 20 nm) of $Li_2Fe_{0.99}Mg_{0.01}SiO_4$/C with significantly improved electrochemical performance compared to other preparations reported in the literature [87, 88].

4.2 Material synthesis

Li_2FeSiO_4/C and Mg doped Li_2FeSiO_4/C were synthesized by a solvothermal method. All chemicals used in the synthesis were procured from Sigma-Aldrich and were used without further purification. In a typical synthesis of Li_2FeSiO_4/C by the solvothermal method, lithium

acetate (1.0202 g), ferric nitrate (2.02 g), silicon acetate (1.32 g), and P123 (1 g) were dissolved separately in ~20 ml of absolute ethanol and then transferred to a beaker to form precursor solution. The precursor solution was sealed in a Teflon lined stainless steel autoclave and held in a 140 ^{o}C heated oven for 24 hours, which was then cooled to room temperature. The intermediate product was poured into a beaker and excess solvent was evaporated by heating at 100 ^{o}C on a hot plate to obtain the dried powder which was subsequently finely ground and heated under argon flow at 600 ^{o}C temperature for 9 hours. Magnesium chloride was used as the Mg precursor to prepare $Li_2Fe_{1-x}Mg_xSiO_4/C$ (x = 0.01, 0.02 and 0.04) composites. A required amounts of magnesium chloride to maintain the desired ratio of Fe:Mg were dissolved in ferric nitrate at the beginning of the synthesis process, while keeping the other synthesis conditions same. In what follows, the $Li_2Mg_xFe_{1-x}SiO_4/C$ composites with x = 0.00, 0.01, 0.02 and 0.04 will be referred as LFS/C, 1Mg-LFS/C, 2Mg- LFS/C, and 4Mg-LFS/C, respectively.

4.3 Results and discussion

4.3.1 XRD analysis and Carbon determination

Figure 4.1 shows the Rietveld refined XRD patterns of undoped and Mg-doped LFS/C composites. The XRD patterns of Mg-doped samples are similar to that of the undoped sample, and all the diffraction peaks are in good agreement with the monoclinic structure with P 2_1/n space group [48, 157]. Broadening of the XRD peaks, specifically for LFS/C and 1Mg-LFS/C, clearly indicates the nanocrystalline nature of these composites. However, increase in Mg concentration in LFS (2Mg-LFS/C and 4Mg-LFS/C) leads to an increase in crystallinity and particle size (Fig. 4.1). This is evident from XRD peak at $2\theta \approx 33^{o}$, which is very broad in LFS/C and becomes narrower and sharper, and finally emerges as doublet in 4Mg-LFS/C (Fig. 4.1 inset). The average particle size, calculated using Scherrer equation were 15 nm, 18 nm, 35 nm and 60 nm for LFS/C, 1Mg-LFS/C, 2Mg-LFS/C and 4Mg-LFS/C, respectively.

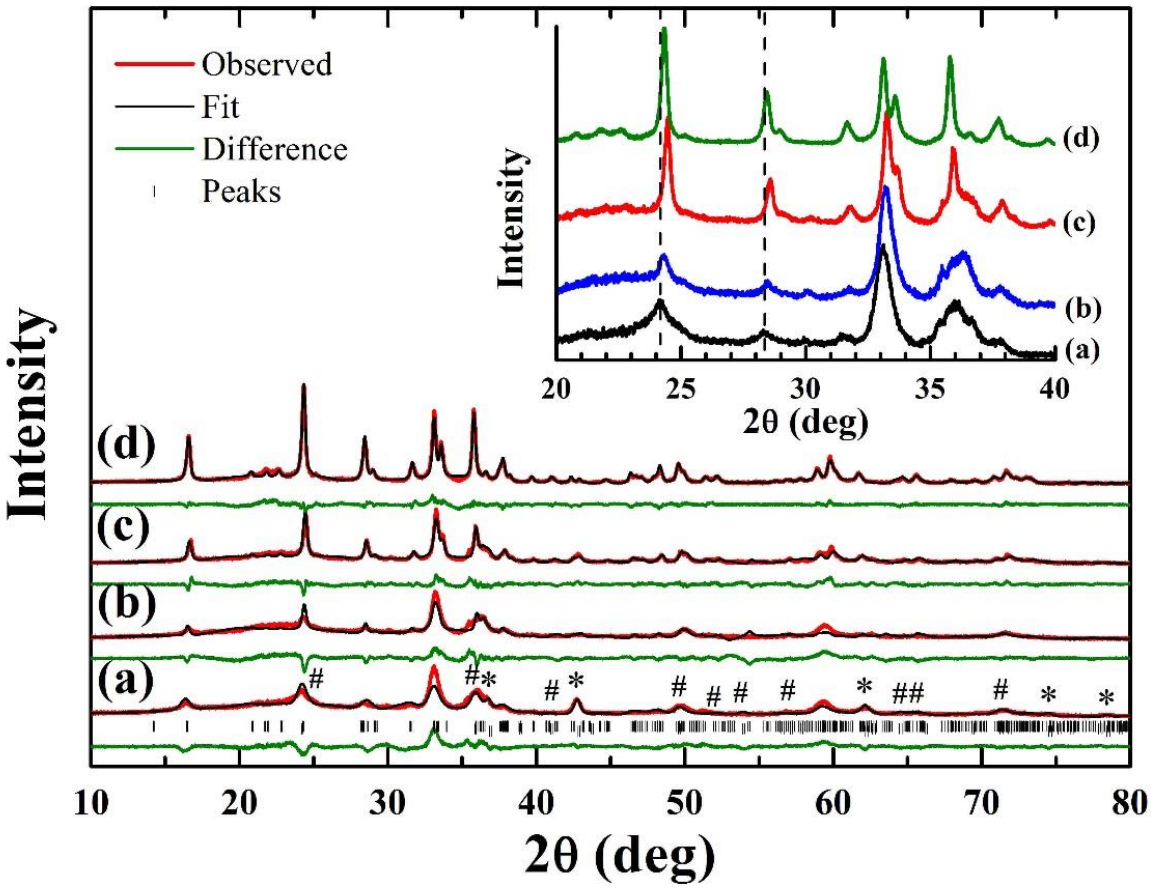

Fig. 4.1 XRD patterns and Rietveld refinement profiles of (a) LFS/C, (b) 1Mg-LFS/C, (c) 2Mg-LFS/C and (d) 4Mg-LFS/C. In (a) the α-Fe_2O_3 and FeO impurity peaks marked with symbols # and *. The inset shows the enlarged region of 2θ= 20^o to 2θ = 40^o emphasizing the peak shifts and line narrowing upon Mg doping.

Incorporation of Mg into Li_2FeSiO_4 lattice is confirmed by the observed shift in XRD peaks (Fig. 4.1 inset) and decrease in unit cell volume of Mg doped LFS/C compared to undoped LFS/C (Table 4.1), as the ionic radius of Mg^{2+} is smaller than that of Li^+ and Fe^{2+} ions. This is in agreement with other observations reported in the literature and confirms the incorporation of Mg into Fe^{2+} site [88]. Rietveld refinement of the XRD pattern also shows the presence of some impurity phases FeO and α-Fe_2O_3 (see labeled peaks on trace (a) in Fig. 4.1), which decrease and disappear in 4% Mg doped sample. As Li_2FeSiO_4 and several impurity phases, such as FeO, α-Fe_2O_3, Li_2FeO_3, and $LiFe(Si_2O_6)$ have overlapping peaks [158], which poses a challenge in

uniquely identifying the peaks and the amount of impurity phase in LFS/C, especially due to peak broadening in these nanocrystalline (crystallite size ≈15 nm) samples. The observed increase in the crystallite size with increasing amount of Mg doping is also consistent with other reported studies in the literature [158], and our observations suggest that Mg acts as a flux for the growth of impurity free Li_2FeSiO_4 crystal without affecting the monoclinic structure. Our Rietveld analysis of 4Mg-LFS/C composite does not show any impurity phase, and the reliability factor R_{wp} of 1.71% is achieved with just a single phase fit. No diffraction peaks corresponding to carbon are found in the XRD patterns of these samples, which implies pyrolytic carbon generated from P123 is amorphous nature in nature. The average carbon content as determined by CHN analyses is about ~15 % in all the samples.

Table 4.1 Lattice parameters of $Li_2Fe_{1-x}Mg_xSiO_4/C$ (x = 0, 0.01, 0.02, 0.04) samples

Sample	**a/Å**	**b/Å**	**c/Å**	V/Å^3	β/^{o}	**Average Particle size**
LFS/C (x = 0)	8.27262	4.99238	8.20031	335.092	98.340	15 nm
1Mg-LFS/C (x = 0.01)	8.25562	4.98659	8.21031	333.956	98.869	18 nm
2Mg- LFS/C (x = 0.02)	8.21406	4.99541	8.21542	331.673	99.204	35 nm
4Mg-LFS/C (x = 0.04)	8.23075	5.01185	8.22326	334.927	99.125	60 nm

4.3.2 XPS analysis and Conductivity measurement

X-ray photoelectron spectroscopy (XPS) spectrum obtained for 1Mg-LFS/C composite is shown in Fig. 4.2(a), which shows the presence of elements C, Li, Fe, Si and O. Figure 4.2(b) and its inset shows the Fe2p and Mg2p XPS spectra of 1Mg-LFS/C. Peaks with binding energies (BE) at 709. 9 eV and 723.5 eV of Fe2p which are characteristic of Fe^{2+} state of Fe in 1Mg-LFS/C that could be assigned to Fe $2p_{3/2}$ and Fe $2p_{1/2}$ [76]. This confirms of the existence of only

Fe^{2+} state in Mg doped LFS/C composites. Mg2p peak in 1Mg-LFS/C appears as weak signal (inset in Fig. 4.2(b)) due to the lower concentration of Mg in 1Mg-LFS/C.

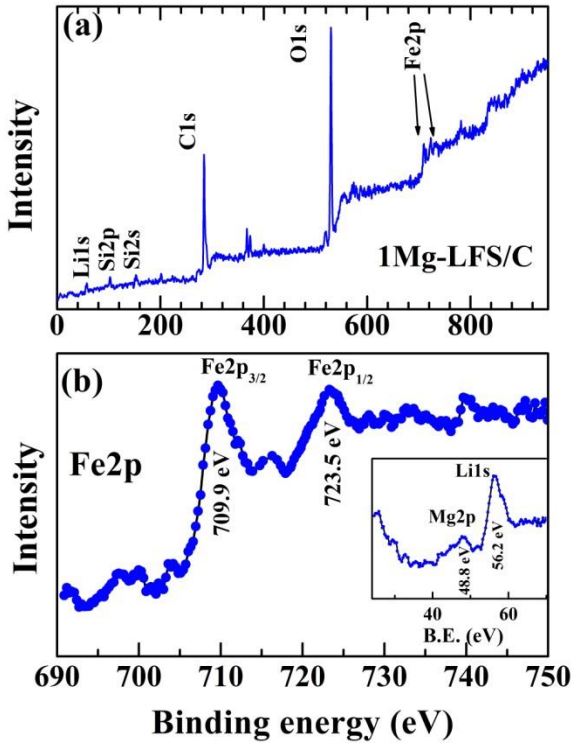

Fig. 4.2 XPS spectrum of (a) 1Mg-LFS/C, and (b) 1Mg-LFS/C enlarged to show Fe2p region. The inset (b) shows Mg2p peak in 1Mg-LFS/C.

The room temperature conductivities of the composites were measured by van der Pauw method on the compressed pallets at 5 MPa pressure and the conductivity of the composites are (Table 4.2): LFS/C (3.2×10^{-4} $S\cdot cm^{-1}$), 1Mg-LFS/C (2.9×10^{-3} $S\cdot cm^{-1}$), 2Mg-LFS/C (1.2×10^{-2} $S\cdot cm^{-1}$) and 4Mg-LFS/C (1.3×10^{-2} $S\cdot cm^{-1}$). The electrical conductivity of LFS without carbon coating is $\sim10^{-14}$ $S\cdot cm^{-1}$ [145]. It is clear from our measurements that the presence of carbon significantly enhances the conductivity of LFS/C composite and Mg doping further increases the electronic conductivity by one to two orders of magnitude, which is in agreement with other studies reported in the literature [87].

4.3.3 Morphology and microstructure

Figures 4.3 (a-d) shows the SEM images of (a) LFS/C, (b) 1Mg-LFS/C, (c) 2Mg-LFS/C, and (d) 4Mg-LFS/C. No significant difference in morphology could be discerned after Mg doping. All the samples are micron-sized agglomerates, which are composed of nano-sized particles with nearly uniform spherical size. EDX elemental mappings (Fig. 4.4(b-d)) show a uniform distribution of Fe, Si and Mg elements in 1Mg-LFS/C.

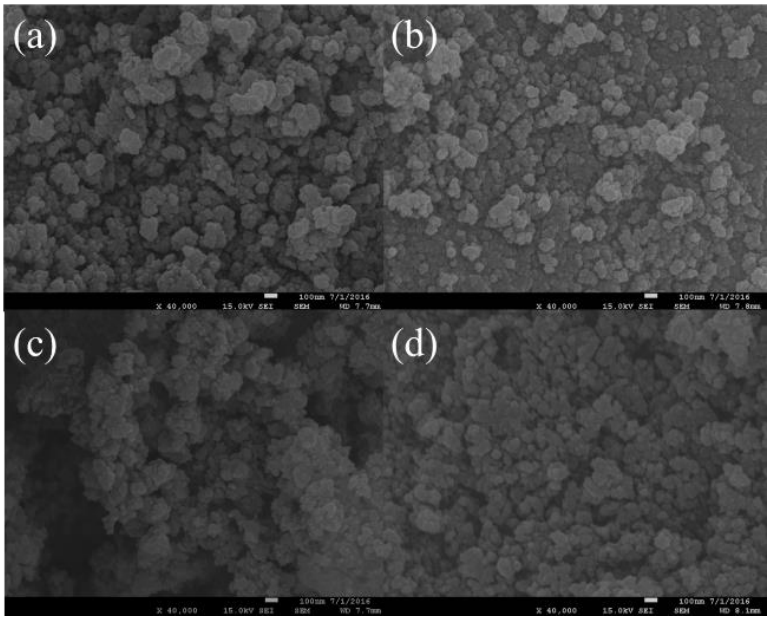

Fig. 4.3 SEM images of (a) LFS/C, (b) 1Mg-LFS/C, (c) 2Mg-LFS/C, and (d) 4Mg-LFS/C.

The structure and morphology of Mg doped LFS/C samples were further confirmed by TEM (Fig. 4.5(a), (b), (e) and (f)). From TEM images it is evident that the size of LFS/C is the smallest, which increases with increasing amount of Mg doping, in agreement with XRD results. Figures 4.5 (c) and (d) show HRTEM and EDX spectra of 1Mg-LFS/C, showing the crystalline nature and presence of Mg. From the inset of Fig. 4.5(f), it is obvious that the Mg doped LFS/C composite is composed of nanoparticles embedded in amorphous carbon network.

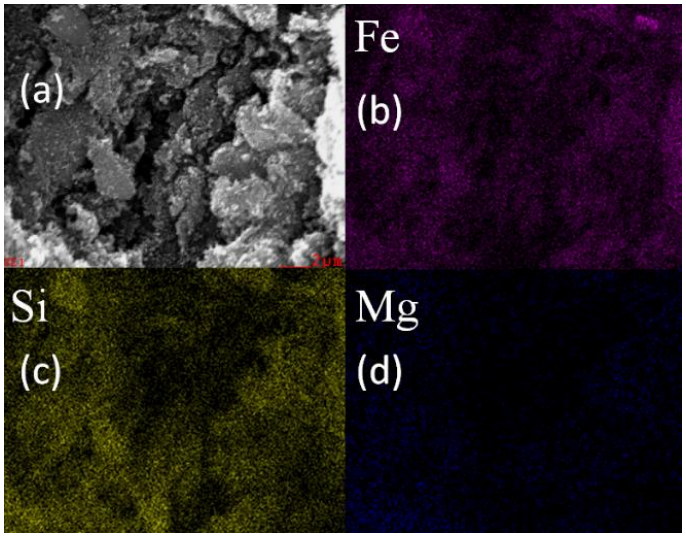

Fig. 4.4 (a) SEM image of 1Mg-LFS/C, and its elemental mapping showing uniform distribution of (b) Fe, (c) Si, and (d) Mg.

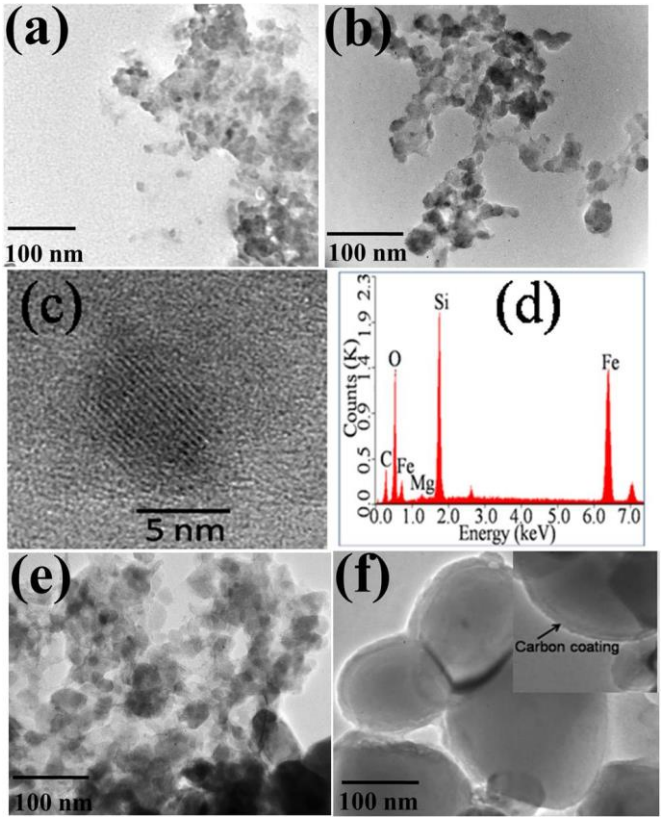

Fig. 4.5 TEM image of (a) LFS/C, (b) 1Mg-LFS/C, and HRTEM image of (c) 1Mg-LFS/C (d) EDS spectrum of 1Mg-LFS/C, (e) TEM image of 2Mg-LFS/C and (f) TEM image of 4Mg-LFS/C and the inset shows a carbon coated particle.

4.3.4 Surface area and porosity

Figure 4.6 shows the nitrogen adsorption-desorption isotherms recorded at 77 K to measure specific surface area of the samples. Among the samples, the 1Mg-LFS/C shows the largest surface area of 106 $m^2 \cdot g^{-1}$ compared to 99 $m^2 \cdot g^{-1}$, 89 $m^2 \cdot g^{-1}$ and 89 $m^2 \cdot g^{-1}$ shown by LFS/C, 2Mg-LFS/C and 4Mg-LFS/C, respectively. The average pore size, measured using the analysis of desorption curve of N_2 isotherms, was 7.0 nm, 5.6 nm, 6.9 nm and 3.2 nm for LFS/C, 1Mg-LFS/C, 2Mg-LFS/C, and 4Mg-LFS/C, respectively and 4Mg-LFS/C showed the broad pore size distribution among all the samples (inset Fig. 4.6).

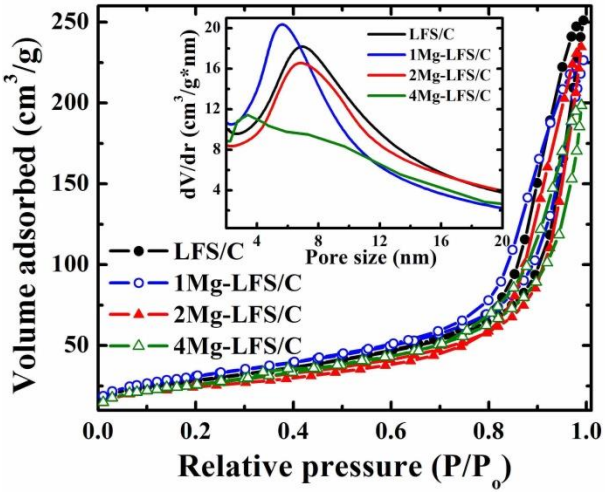

Fig. 4.6 N_2 adsorption/desorption isotherms of LFS/C, 1Mg-LFS/C, 2Mg-LFS/C and 4Mg-LFS/C. The inset shows their pore size distributions.

4.4 Electrochemical results

4.4.1 Galvanostatic charge/discharge

The charge/discharge profiles were investigated in the potential window of 1.5-4.6 V vs. Li/Li^+ at various rates. Typical charge/discharge profiles for first five cycles obtained for 1Mg-LFS/C at C/30 rate are shown in Fig. 4.7(a). The charge profile of first cycle exhibits two voltage plateaus; the first one appearing at ~3.2 V corresponds to the Fe^{2+}/Fe^{3+} redox couple and the

second one at ~4.3 V can be attributed to Fe^{3+}/Fe^{4+} redox couple. The initial discharge capacity of ~ 278 $mAh{\cdot}g^{-1}$ obtained for 1Mg-LFS/C in the first cycle is ≈ 84% of the theoretical capacity, very similar to that undoped LFS/C (~ 276 $mAh{\cdot}g^{-1}$) discussed in chapter-3. It is clear from the charge/discharge curves in Fig. 4.7(a) that the first plateau in the second cycle appear at a lower voltage compared to the plateaus observed in the first charge/discharge cycle. This observation can be attributed to a Li/Fe anti-site exchange process during the initial charging [144]. We noted that although both LFS/C and 1Mg-LFS/C samples have a very similar first cycle discharge capacity, a comparison of their second cycle of charge/discharge profiles (see Fig. 4.7(b)) shows a higher discharge capacity ~ 268 $mAh{\cdot}g^{-1}$ for 1Mg-LFS/C compared to ~ 256 $mAh{\cdot}g^{-1}$ for LFS/C. Clearly, Mg doping seems to lessen the fading of capacity due to one order of magnitude increase in its electrical conductivity.

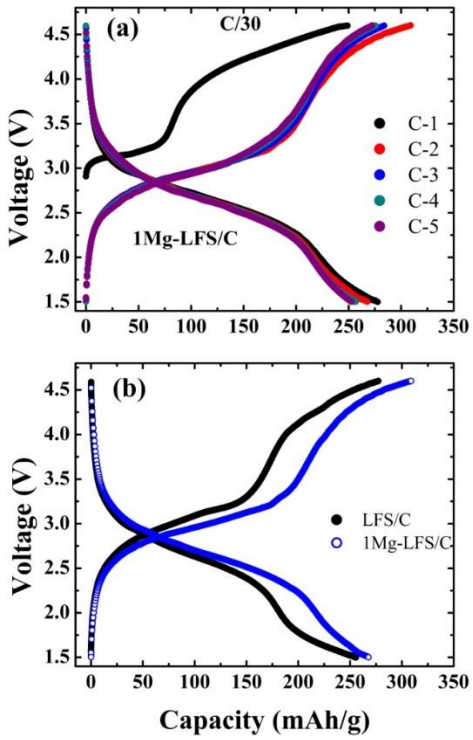

Fig. 4.7 Charge discharge profile of 1Mg-LFS/C (a) for the first 5 cycles, and (b) comparison of 2nd cycle of charge discharge profiles of LFS/C and 1Mg-LFS/C at C/30.

The rate capability of LFS/C and Mg doped LFS/C composites at different rates are shown in Fig. 4.8(a). We observe that 1Mg-LFS/C composite shows better cyclic performance, at each rate, compared to other composites. The cyclic stability curves for LFS/C and 1Mg-LFS/C at 1C rate are shown in the inset of Fig. 4.8(a). Both the composites exhibit the stable cycle life over 100 cycles, and Mg doping does not alter cycle stability of its capacity. In addition, on increasing the doping concentration of Mg > 1%, the discharge capacity decreases. This decrease in capacity in higher concentration of Mg doped composites may be attributed to the decreased surface area arising from increased particle size and crystallinity in these composites.

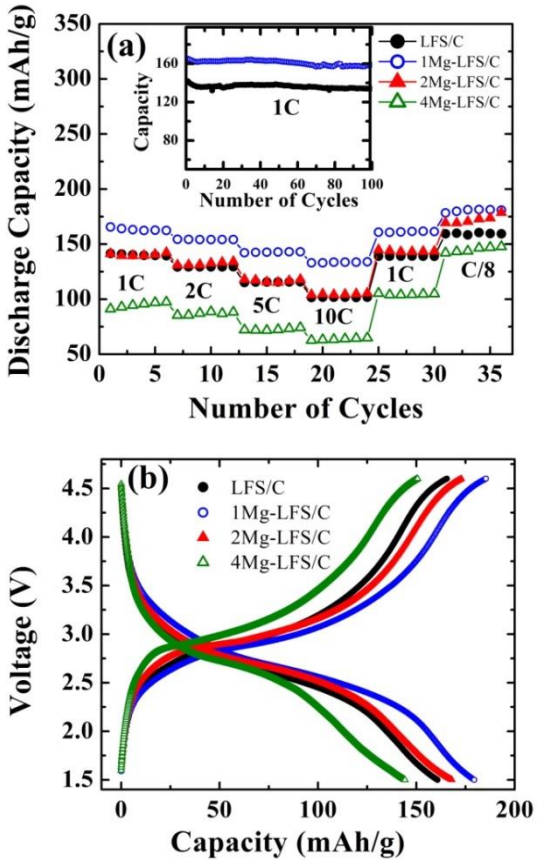

Fig. 4.8 (a) Rate capability of LFS/C and Mg doped LFS/C at different rates. The inset in (a) shows the cyclic stability curves for LFS/C and 1Mg-LFS/C at 1C and (b) Charge/discharge profiles of LFS/C and Mg doped LFS/C at C/8 rate.

Figure 4.8(b) compares the charge/discharge curves at C/8 rate, after rate capability studies. It can be seen that 1Mg-LFS/C exhibits the highest discharge capacity of 181 $mAh \cdot g^{-1}$ while 4Mg-LFS/C delivers the lowest average capacity of 145 $mAh \cdot g^{-1}$. These results demonstrate that an optimum amount of Mg-incorporation into LFS/C cathode material (1% Mg in our case) can lead to improved electrochemical performance of the material. It is interesting to note that the discharge capacities at various rates for LFS/C, synthesized by our method are better than that of LFS/C synthesized by the ultrasonic-assisted sol–gel method by Qu *et. al.,* [88] and comparable to their results of Mg-doped Li_2FeSiO_4/C at low rates (C/10). However, at higher rates, for example at 1C, 1Mg-LFS/C sample showed a discharge capacity of ~ 160 $mAh \cdot g^{-1}$, 14% improvement over the value of ~ 140 $mAh \cdot g^{-1}$ observed for their Mg doped LFS/C. We attribute this to much reduced particle size (< 20 nm) in our 1Mg-LFS composite with similar carbon content.

4.4.2 Cyclic voltammetry

Cyclic voltammetry measurements were conducted on LFS/C and 1Mg-LFS/C to further investigate the electrochemical performance. The I-V plots for LFS/C and 1Mg-LFS/C at a scan rate of 0.1 mV/s are compared in Fig. 4.9. The first oxidation peak seen at ~3.04 V in LFS/C corresponds to the first electron transfer in the electrochemical reaction, in which Fe^{2+} is oxidized to Fe^{3+}. However, at the same scan rate, for 1Mg-LFS/C sample the first oxidation peak is seen at 3.09 V and the second oxidation peak is not visible in both the cases. Further, it may be noted that the peak height is larger for 1Mg-LFS/C sample compared to LFS/C, indicating fast kinetics for the 1Mg-LFS/C sample.

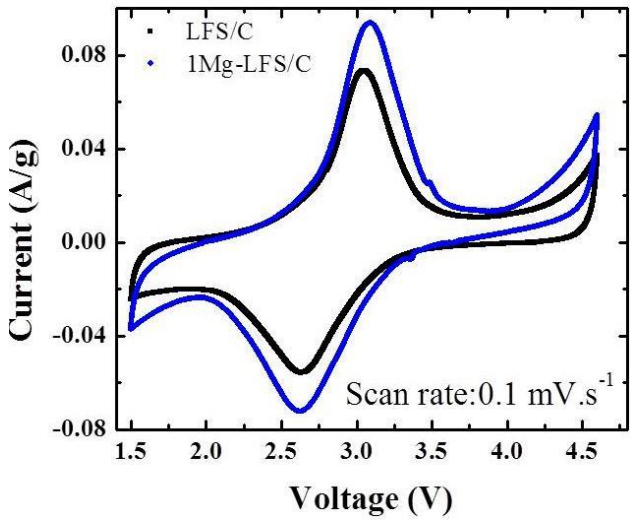

Fig. 4.9 I-V plots of LFS/C and 1Mg-LFS/C at a scan rate of 0.1 mV.s^{-1}.

4.4.3 Electrochemical impedance spectroscopy

Figures 4.10 (a) and (b) show the Nyquist plots, and graphs of Z' vs. $\omega^{-1/2}$ in the low frequency range for LFS/C, 1Mg-LFS/C, 2Mg-LFS/C and 4Mg-LFS/C samples. The spectra show a depressed semicircle in the high frequency region and an inclined straight line in the low frequency region, which is a typical characteristic of an electrochemical cell. The intercept on the Z' axis in high frequency region corresponds to the electrolyte resistance in the Nyquist plot. The inclined line in the low frequency line is related to the lithium ion diffusion in the cathode material which is a typical of Warburg behavior. The semicircle intercept corresponds to the charge transfer resistance, R_{ct}. We can clearly see from the Fig. 4.10(a) that 1Mg-LFS/C shows the lowest charge transfer resistance value of $R_{ct} \approx 27$ Ω, and the highest for 4Mg-LFS/C ($R_{ct} \approx$ 77 Ω) with LFS/C and 2Mg-LFS/C samples showing very similar R_{ct} values ~ 33 Ω. The R_{ct} values for all the samples are listed in Table 4.2.

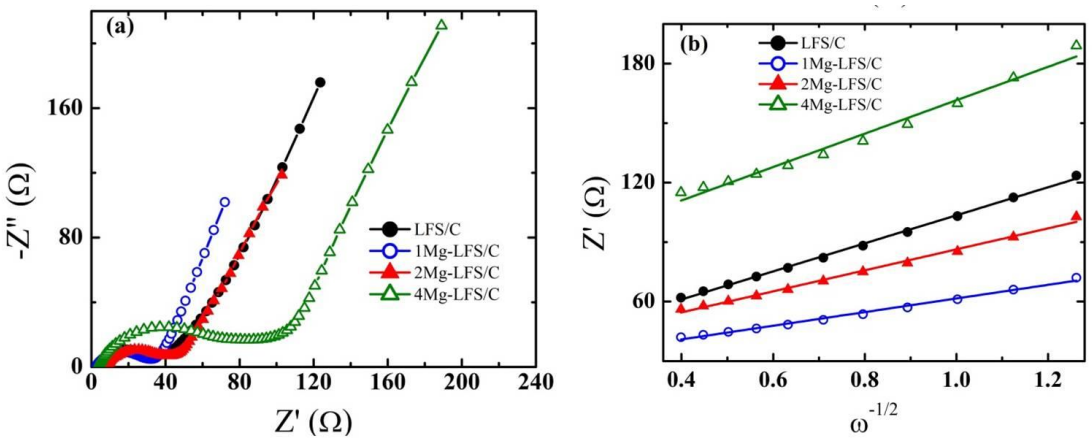

Fig. 4.10 (a) Nyquist plots of LFS/C, 1Mg-LFS/C, 2Mg-LFS/C and 4Mg-LFS/C samples, (b) plots of Z' vs. $\omega^{-1/2}$ in the low frequency region.

Table 4.2 Electrochemical impedance parameters and the exchange current density of the $Li_2Fe_{1-x}Mg_xSiO_4/C$ (x = 0, 0.01, 0.02, 0.04) samples

Sample	**Conductivity ($S \cdot cm^{-1}$)**	**R_{ct} (Ω)**	**σ ($\Omega.s^{1/2}$)**	**D_{Li} ($cm^2 \cdot s^{-1}$)**	**I_o ($mA \cdot g^{-1}$)**	**Diffusion Length (nm)**
LFS/C	3.2×10^{-4}	32.8	70	6.7×10^{-14}	78.8	49
1Mg-LFS/C	2.9×10^{-3}	27.0	34	2.0×10^{-13}	95.7	93
2Mg- LFS/C	1.2×10^{-2}	33.4	53	9.8×10^{-14}	77.4	60
4Mg-LFS/C	1.3×10^{-2}	77	84	3.0×10^{-14}	33.6	38

Figure 4.10(b) shows plots of Z' versus $\omega^{-1/2}$ for LFS/C Mg doped LFS/C samples, yields a straight line with slope σ, and the lithium ion diffusion coefficient can be calculated using Eq. (2.11). Table 4.2 lists the Li-ion diffusion coefficient calculated using Eq. (2.11) and the values of charge transfer resistances are found from the intercept on y axis. The values of charge transfer resistance and diffusion coefficient found here are in good agreement with reported values with increasing Cd incorporation into Li_2FeSiO_4/C by Zhang *et. al. [91]* . The 1Mg-LFS/C sample which shows the highest diffusion coefficient compared to other samples also has

the lowest charge transfer resistance, which is consistent with the enhanced electrochemical performance exhibited by this sample compared to other samples studied in this work. We have also calculated the exchange current density, $I_o = RT/nR_{ct}F$, given by [159] and the characteristic diffusion length, $L_{\max,\mathrm{Li}} = \sqrt{\tau D_{\mathrm{Li}}}$, where τ is the diffusion time constant [160]. At higher C-rate (faster charging/discharging), the characteristic diffusion length decreases with diffusion time constant (taken as the discharging time), and the particle size comparable to the characteristic diffusion length are indicative of better electrochemical performance at higher charge/discharge rates. The estimated characteristic diffusion lengths listed in Table 4.2 which are calculated using a discharging time for 10C rate. The higher Li-ion diffusion coefficient (faster kinetics of the cell), and higher exchange current density (higher catalytic activity) are associated with enhanced electrochemical performance of the material. Clearly, 1Mg-LFS/C has these desirable parameters. The diffusion length in 4Mg-LFC/C is smaller than the particle size indicating the full particle is not utilized in charge/discharge process thus showing a decreased capacity at all charging/discharging rates compared to other composites studied in this work.

In our investigation of Mg doped Li_2FeSiO_4/C, we find that 1% Mg doped Li_2FeSiO_4/C (1Mg-LFS/C) shows enhanced electrochemical performance. This can be attributed to combined factors, like, large surface area (106 $m^2 \cdot g^{-1}$) due to nanosized particles (< 20 nm) coated with porous carbon with enhanced electrical conductivity leading to lower charge transfer resistance (R_{ct} ~ 27.0 Ω) and enhanced diffusion coefficient (2.0 $\times 10^{-13}$ $cm^2 \cdot s^{-1}$), and thus large exchange current density with optimal carbon coating brought about by P123 polymer in 1Mg-LFS/C. It may be noted that during the synthesis, the heating of Li_2FeSiO_4 precursors with P123 produces a thin coating of carbon around the LFS particles increasing the electronic conductivity, and Mg doping reduces the impurity phases in the composites leading to improved ionic conductivity.

Further, heating in the presence of polymer also leads to porous carbon with large surface area and provides an increased contact area between the electrolyte and cathode facilitating fast lithium insertion/extraction during the charge/discharge cycling. Additionally, nano-size particles reduce the lithium diffusion path length and thus, improve the electrochemical performance of the composites. In addition, from the XRD results it is evident that with increase in Mg concentration the impurity component in the samples decreases at the cost of increased particle size. Hence, it may be argued that 1Mg-LFS/C sample may have all favorable factors for better electrochemical performance. The decrease in capacity with increasing Mg concentration in LFS/C may be attributed to reduction in the surface area due to increased particle size, higher charge transfer resistance, and lower Li-ion diffusivity.

4.5 Conclusions

In summary, we have synthesized a series of porous Mg doped $Li_2Fe_{1-x}Mg_xSiO_4/C$ (x = 0, 0.01, 0.02, 0.04) nanocomposites by a solvo-thermal method using tri-block copolymer as carbon source and surfactant, and compared their structural and electrochemical properties with un-doped Li_2FeSiO_4/C using different characterization techniques. Mg doping is found to favor the growth of impurity free Li_2FeSiO_4 with monoclinic structure. Among the composites studied in this work, $Li_2Fe_{0.99}Mg_{0.01}SiO_4$ showed the best electrochemical performance, which we attribute to its lower charge transfer resistance and enhanced Li-ion diffusion coefficient due to its smaller particle size (< 20 nm) with large surface area, reduced impurity phases, and increased electronic conductivity compared to undoped Li_2FeSiO_4/C.

CHAPTER 5 IMPROVED ELECTROCHEMICAL PERFORMANCE OF Li_2FeSiO_4/CNF/rGO NANO COMPOSITE FOR ADVANCED LITHIUM ION BATTERIES

In this Chapter, the method to enhance the electronic conductivity of Li_2FeSiO_4 by introducing reduced graphene oxide (rGO) and carbon nano-fibers (CNF) during the synthesis of Li_2FeSiO_4 nanocomposites is described. We have synthesized Li_2FeSiO_4/CNF and Li_2FeSiO_4/CNF/rGO nano-composites by solvothermal method and investigated their structural and electrochemical properties. A comparison of their electrochemical properties shows that Li_2FeSiO_4/CNF/rGO has better electrochemical performance compared to Li_2FeSiO_4/CNF nano-composite. Both the composites show excellent cycle stability, exhibiting very stable cycling performance at 1C rate for 200 cycles with retention of 90% of their initial discharge capacity.

5.1 Introduction

Carbon based nano-materials play an important role in the development and design of energy storage and conversion devices [161, 162] and their composites with electrode materials are used in lithium ion batteries to improve the electrochemical performance. The conducting carbon coating, using the surfactant or polymer during material synthesis, is one of the effective ways to enhance the electronic conductivity and hence the electrochemical performance in Li_2FeSiO_4 [60, 67, 70, 71]. The carbon coating facilitate the electron transfer between adjacent particles by creating pathway between them leading to reduction in impedance for mass and electron transfer between the grain boundaries [64]. However, carbon coating from the surfactants or polymer during calcination at higher temperatures affects the morphology and increases the possibility of formation of impurities in the final product [45]. Alternative methods, such as, addition of conducting nano-carbon materials, like nanotubes, carbon nanofibers, graphene/reduced graphene oxide, have been used to enhance the conductivity of Li_2FeSiO_4 without introducing

the impurities [64, 65, 72-76, 79-82]. Such composites have shown improved electrochemical performance of Li_2FeSiO_4 cathode. Carbon nanotubes or carbon nanofibers with their unique properties like high surface area (100 to 1000 $m^2 \cdot g^{-1}$) [163] , high electronic conductivity, and chemically stable 1D structure have been considered as potential conducting fillers with flexibility to deposit the Li_2FeSiO_4 nanoparticles on their surface [74]. In a similar way, graphene with 2D layer structure with one atomic thickness of carbon, very high surface area, (2600 $m^2 \cdot g^{-1}$), high electronic conductivity, and high mechanical strength [163] has been incorporated as electrical conducting filler for Li_2FeSiO_4 cathode matrix [65, 79, 82]. Graphene contains sp^2 hybridized carbon atoms arranged in a honeycomb ring, which is the building block of other carbonaceous materials (graphite, fullerene, carbon nanotubes) [164]. The reduced graphene oxide is obtained by chemical route via reducing the insulating graphene oxide nanosheets with hydrazine, $NaBH_4$, microwave and laser irradiation [165]. In addition to enhancing electronic conductivity of cathode materials, CNF and rGO incorporation reduces the crystallite size of materials which helps to shorten the Li-ion diffusion path length and improves the electrochemical performance due to better utilization of the active material. Furthermore, CNF and rGO, due to their excellent mechanical property, provide the structural stability and improved cyclability to cathode materials.

In the present work, we used carbon nanofibers and reduced graphene oxide as conductive fillers in Li_2FeSiO_4 material to improve the conductivity and therefore, enhance the electrochemical performance of Li_2FeSiO_4. Reduced graphene oxide has large surface area compared to CNF, increases the contact area with electrolyte and acts as mini current collector in cathode matrix, whereas CNF helps increase conductivity only. We synthesized ternary Li_2FeSiO_4/CNF/rGO nano-composite to take advantage of desirable properties of both CNF and

rGO and present a comparison of its performance with Li_2FeSiO_4/CNF nano-composite. The structural properties of the nanocomposites were investigated by x-ray diffraction, scanning electron microscopy, transmission electron microscope, and BET analysis technique, and the electrochemical properties were investigated by galvanostatic charge-discharge and electrochemical impedance spectroscopy (EIS).

5.2 Material synthesis

5.2.1 Reduction of GO

The graphene oxide is chemically converted to reduced graphene oxide, following the method of Li *et. al.* [166], with some modifications. The graphene oxide containing 0.5% solid content dispersed in water was purchased from the Angstrom Materials. In a typical preparation, NH_4OH solution is slowly added to graphene oxide dispersion (1.0 mg/ml) under constant stirring while maintaining the PH of solution ~10. Hydrazine hydride was then added to solution, drop-wise, maintaining the weight ratio of graphene oxide to hydrazine hydride to 10:7. The resulting solution was kept on a hot plate at 100 ^oC for one hour under constant stirring. The reduced graphene oxide solution was filtered and washed several times with DI water and ethanol. The filtered product was dispersed again in ethanol and sonicated for 4 hours before using in solvothermal synthesis of Li_2FeSiO_4/CNF/rGO.

5.2.2 Li_2FeSiO_4/CNF/rGO synthesis

The Li_2FeSiO_4/CNF and Li_2FeSiO_4/CNF/rGO nanocomposites were prepared by solvothermal method. All chemicals used in the synthesis were procured from Sigma-Aldrich and were used without any further purification. In a typical synthesis of Li_2FeSiO_4/CNF by solvothermal method, lithium acetate (1.0202 g), ferric nitrate (2.02 g), and silicon acetate (1.32 g), were dissolved separately in ~20 ml of absolute ethanol taken in separate beakers and then

transferred to a beaker containing 80 mg of CNF dispersed in ~20 ml ethanol and stirred for 30 minutes, and the precursor solution was sealed in Teflon lined stainless steel autoclave and heated at 140 ^{o}C for 24 hour after which it was cooled to room temperature. The intermediate product was poured into a beaker and excess solvent was evaporated by heating at 100 ^{o}C on a hot plate to obtain dried powder, which was finely ground and heated under argon flow at 600^{o}C for four hours. In preparing Li_2FeSiO_4/CNF/rGO, the above mentioned synthesis protocol was used and Li_2FeSiO_4/CNF/rGO was prepared with ratio 1:1 of CNF/rGO 40 mg each. Hereafter, these samples will be referred as LFS/CNF and LFS/CNF/rGO.

5.3 Results and discussions

5.3.1 Structural Analysis (XRD)

The XRD patterns of LFS/CNF and LFS/CNF/rGO are shown in the Fig. 5.1. The broad of the XRD peaks clearly indicates the nano-crystalline nature of the composites. The crystal structure of all the composites was further investigated by Rietveld refinement using GSAS software implemented with EXPGUI interface. The Rietveld refinement of the XRD data for the composites is shown in Fig. 5.2 and the calculated lattice parameters are summarized in Table. 5.1. It is clear that the lattice parameters of the composites are very similar and confirm that addition of different carbon sources does not affect the crystal structure of Li_2FeSiO_4. The XRD patterns of both the composites are indexed to monoclinic $P2_1/n$ phase, which is in agreement with previously reported Li_2FeSiO_4 structure [48, 157]. The peak at ~ 26.4^{o} seen in the LFS/CNF and LFS/CNF/rGO nanocomposites belongs to CNF.

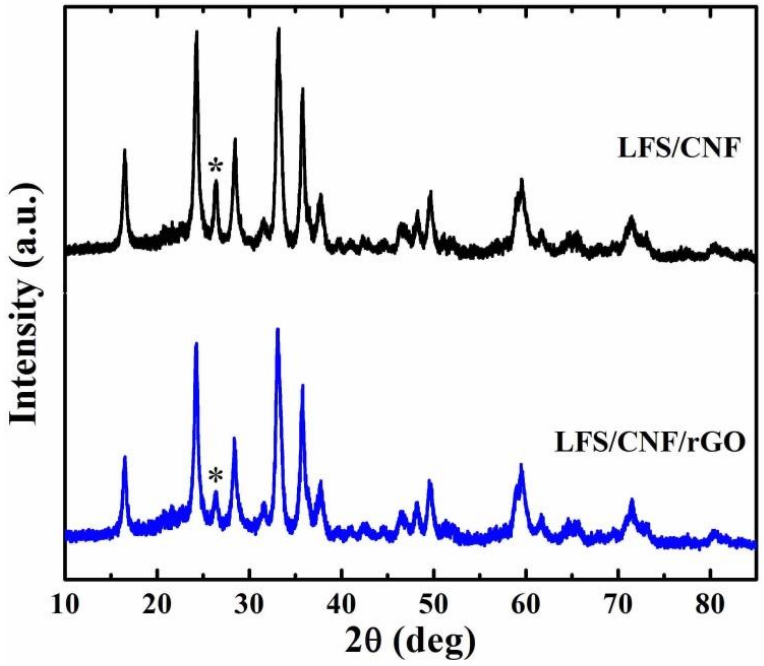

Fig. 5.1 XRD pattern of LFS/CNF and LFS/CNF/rGO nano-composites. The carbon peak in LFS/CNF and LFS/CNF/rGO is marked with asterisk.

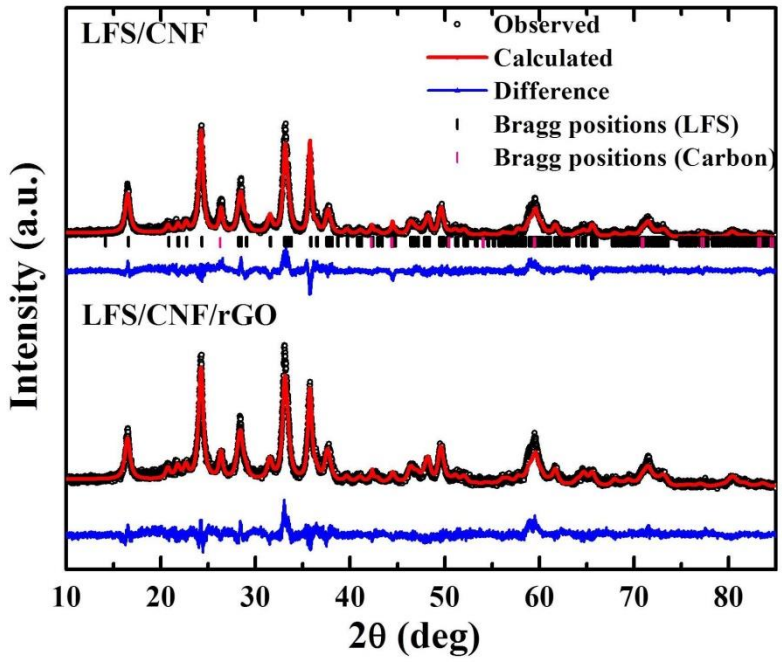

Fig. 5.2 Rietveld refinement patterns of XRD data for LFS/CNF and LFS/CNF/rGO Composites.

Table 5.1 Calculated lattice parameters for LFS/CNF and LFS/CNF/rGO nano-composites

Sample	a/Å	b/Å	c/Å	β/^{o}	Volume/Å^{3}	Particle size (nm)
LFS/CNF	8.2280	5.0121	8.2541	98.91	336.287	22.94
LFS/CNF/RGO	8.2285	5.0103	8.2460	98.93	335.884	21.66

5.3.2 Carbon content determination and conductivity measurements

The carbon contents of the nanocomposites were determined by CHN analysis and average carbon content is found to be ~16% and ~17% in LFS/CNF and LFS/CNF/rGO nano-composites. The residual carbon from the precursor acetate salts forms a thin coating around the nanoparticles and provides better inter-connection between the Li_2FeSiO_4 nanoparticles and rGO/CNF leading to further increase the conductivity of the composites. The room temperature conductivity of the composites were measured by van der Pauw method using pallets compressed at 5 MPa and the measured conductivity of LFS/CNF and LFS/CNF/rGO are ~1.2 $S{\cdot}cm^{-1}$, and ~8.1×10^{-1} $S{\cdot}cm^{-1}$. The conductivity of the nanocomposites are several orders of magnitude higher than the bulk Li_2FeSiO_4 (~10^{-14} $S{\cdot}cm^{-1}$) [145]. The reduction of conductivity in LFS/CNF composite shows that CNFs are uniformly distributed in cathode matrix. The insulated GO is converted into rGO during the reduction with hydrazine hydrate and CNF further enhances the conductivity of the LFS/CNF/rGO composite, which forms a 3D conducting network between rGO and CNF to facilitate the electron transport.

5.3.3 Specific surface area and pore size

To study the porous nature of nanocomposites samples, N_2 adsorption–desorption isotherms were recorded at 77 K. The N_2 adsorption/desorption isotherms are shown in Fig. 5.3. The measured BET surface area for LFS/CNF and LFS/CNF/rGO samples was ~62 $m^2{\cdot}g^{-1}$ and ~88 $m^2{\cdot}g^{-1}$ and the average pore size, measured using the analysis of desorption curve of N_2

isotherms, was 5.3 nm for both the composites. The LFS/CNF showed the broad pore size distribution as compare with LFS/CNF/rGO (inset Fig. 5.3).

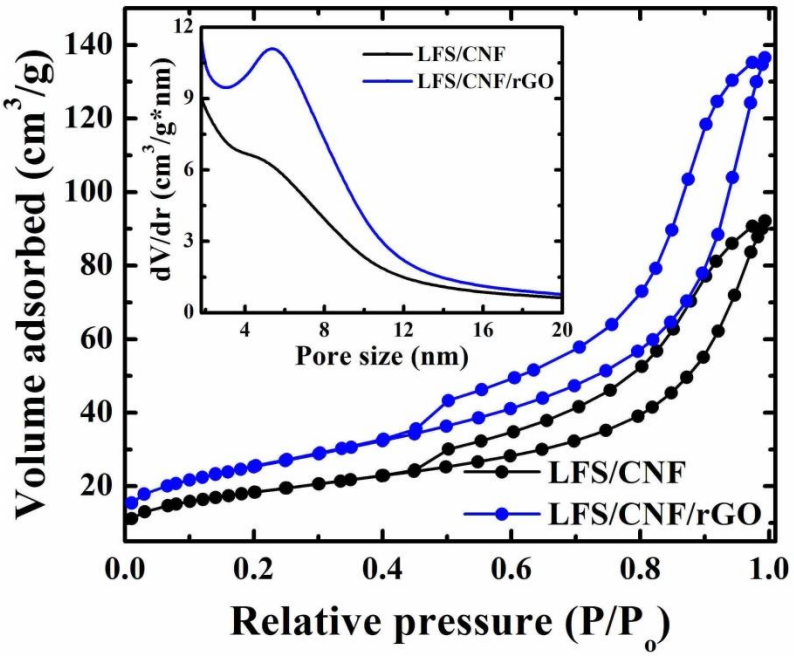

Fig. 5.3 N_2 adsorption/desorption isotherms of LFS/CNF and LFS/CNF/rGO. The inset shows their pore size distributions.

5.3.4 Morphology and Microstructure

The SEM images of LFS/CNF and LFS/CNF/rGO nano-composites are shown in the Fig. 5.4(a, b). The images show the large agglomeration of small nanoparticles, having the uniform and spherical in shape. It is clear from the SEM images of LFS/CNF and LFS/CNF/rGO composites that CNF is embedded in the materials matrix with some particles grown on the surface of CNF. The rGO nano-sheets are not visible in LFS/CNF/rGO nano-composites. Fig. 5.4(c) exhibits the TEM image of LFS/CNF/rGO nano-composite, showing that LFS nanoparticles are attached to CNF.

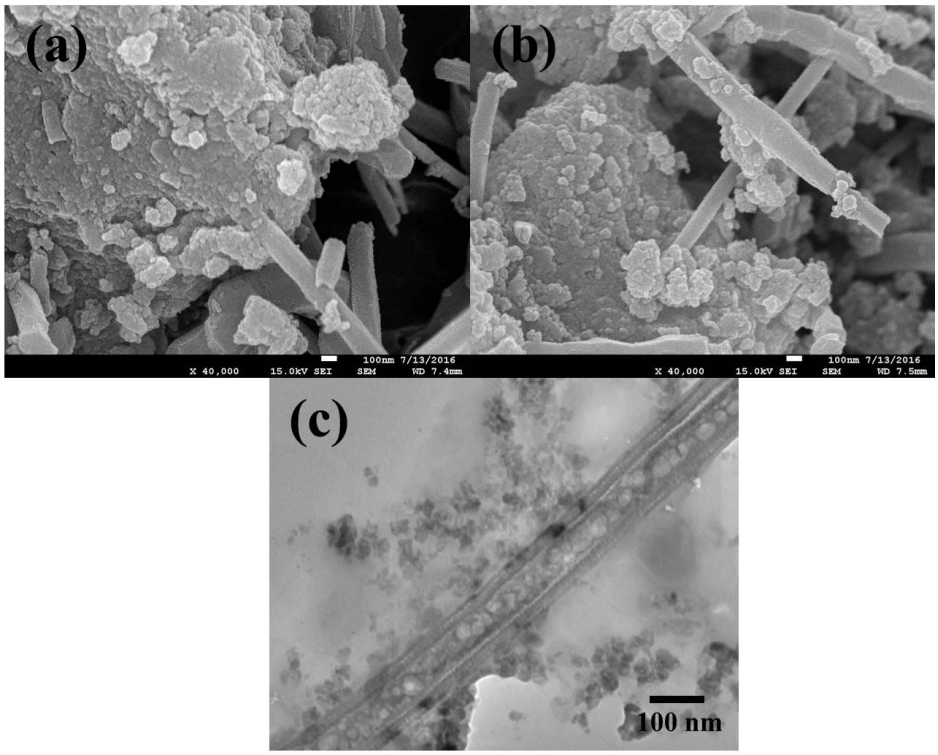

Fig. 5.4 SEM images of (a) LFS/CNF, (b) LFS/rGO nano-composites, and TEM image of (c) LFS/CNF/rGO nano-composite.

5.4 Electro-chemical characterization

5.4.1 Galvanostatic charge/discharge

A typical charge/discharge profiles in the potential window of 1.5-4.6 V vs Li/Li^+ obtained at a rate of C/20 for LFS/CNF and LFS/CNF/rGO is shown in Figs. 5.5(a, b) for first two cycles. All the composites have a very flat first plateaus at ~3.2 V, which corresponds to the Fe^{2+}/Fe^{3+} redox couple and second plateau at ~4.3 V can be attributed to Fe^{3+}/Fe^{4+} redox couple.

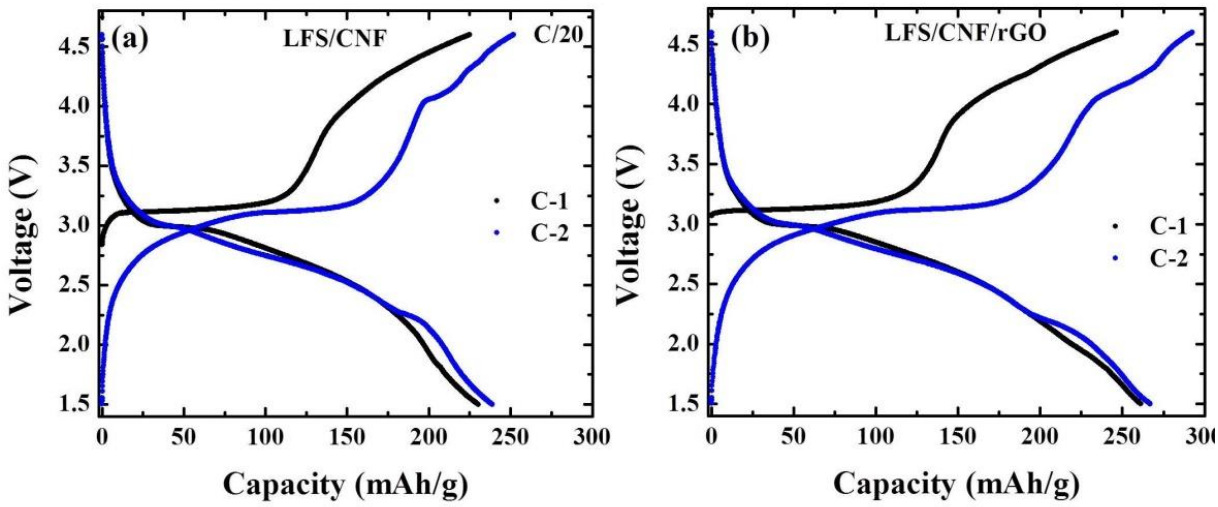

Fig. 5.5 Charge/discharge curves of (a) LFS/CNF and (b) LFS/CNF/rGO.

It is clear from the charge/discharge curves that the first and second plateaus in the second cycle appear at a lower voltage compared to the plateaus observed in the first charge/discharge cycle. This observation can be attributed to a Li/Fe antisite exchange process during the initial charging [144]. The initial discharge capacities of LFS/CNF and LFS/CNF/rGO are about ~230, and 260 $mAh \cdot g^{-1}$, which are 70% and 78% of the theoretical capacity, respectively. In the second cycle, the discharge capacity is increased slightly from the first cycle in all the composites. The LFS/CNF/rGO shows better electrochemical performance compared to LFS/CNF nanocomposites.

The cycling performance of LFS/CNF and LFS/CNF/rGO nanocomposites samples at different rates is shown in Fig. 5.6(a). The LFS/CNF sample delivered an average discharge capacity of 147, 132, 121, 116, and 138 $mAh \cdot g^{-1}$ at 1C, 2C, 4C, 8C, and 1C, respectively, whereas, the LFS/CNF/rGO sample delivered a higher average discharge capacity of 160, 147, 139, 135, and 156 $mAh \cdot g^{-1}$ at the same rates. It is worth noting that discharge capacity depreciation is 21 and 16 % respectively for LFS/CNF and LFS/CNF/rGO as the discharge rate

increases from 1C to 8C. After a continuous charge/discharge at high rates, the LFS/CNF and LFS/CNF/rGO retain discharge capacity about ~94 and ~98%, at 1C rate. The cycling stability curves measured at 1C for first 200 cycles are shown in Fig. 5.6(b) for LFS/CNF and LFS/CNF/rGO. It is clearly seen from the curves that both the composites exhibit excellent stable cycle life, retaining ~90% of its initial discharge capacity even after 200 cycles at 1C rate. Figs. 5.6(c, d) show the charge discharge curves for LFS/CNF and LFS/CNF/rGO at high C-rates (1C, 2C, 4C, and 8C).

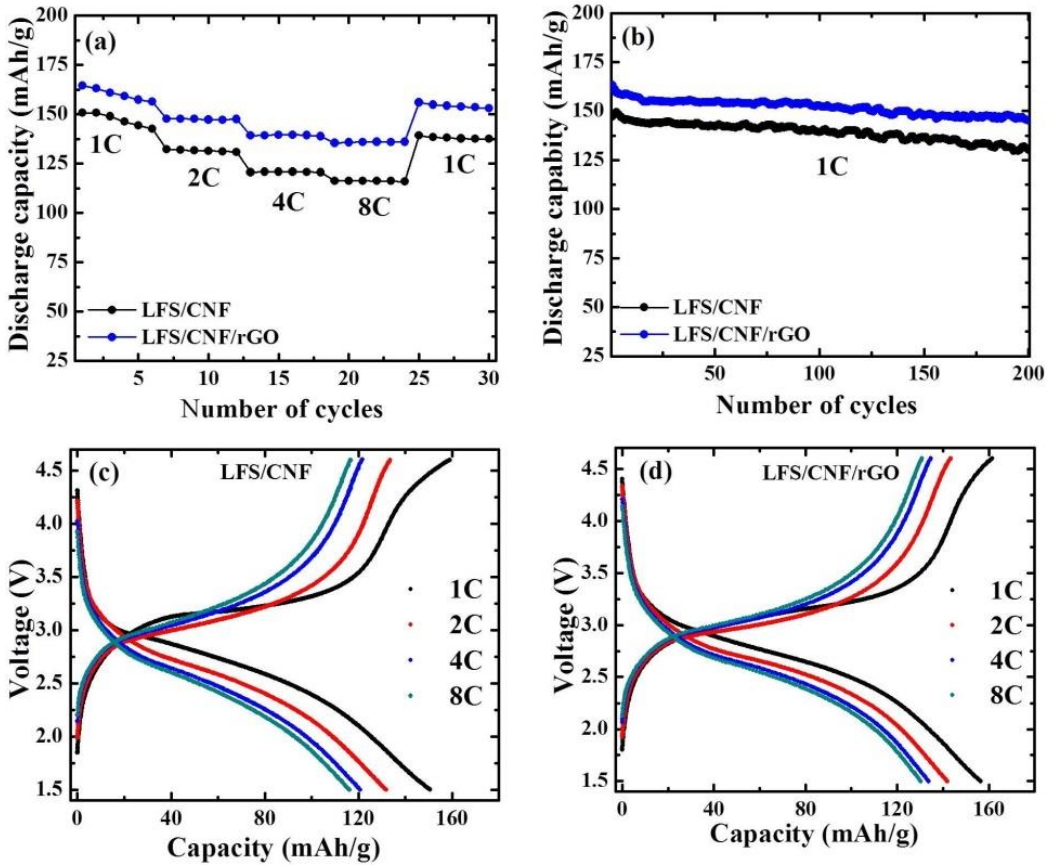

Fig. 5.6 (a) Rate capability of LFS/CNF and LFS/CNF/rGO at different rates, (b) Cyclic stability curves for LFS/CNF and LFS/CNF/rGO at 1C, Charge/discharge profiles of (c) LFS/CNF, and (d) LFS/CNF/rGO at different rates.

The discharge capacities for both the composites decrease with increasing the C-rates due to polarization of electrode. The results show that LFS/CNF/rGO composite has better rate performance than LFS/CNF.

5.4.2 Electrochemical impedance spectroscopy (EIS)

In order to investigate the effect of addition of CNF and CNF/rGO on electrochemical properties of Li_2FeSiO_4, we conducted EIS measurements on LFS/CNF and LFS/CNF/rGO nanocomposites. The Nyquist plots (Fig. 5.7a) of the freshly prepared coin cells of LFS/CNF and LFS/CNF/rGO samples show a typical depressed semicircle in the high frequency region and a straight line in the low frequency region. The intercept on the Z' axis in high frequency region corresponds to the ohmic resistance (R_s) which is mainly the electrolyte resistance. The inclined line in the low frequency region is related to the lithium-ion diffusion in the cathode material which is a typical of Warburg behavior. The other intercept of depressed semicircle corresponds to the charge transfer resistance, R_{ct}.

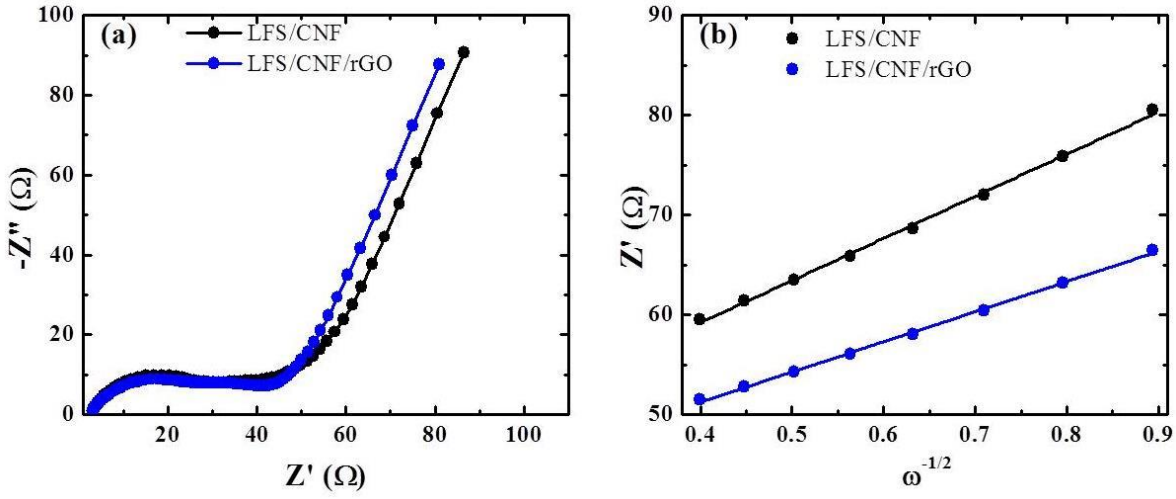

Fig. 5.7 (a) Nyquist plots and (b) graph of Z' v.$\omega^{-1/2}$ in the low frequency range for the coin cell of LFS/CNF and LFS/CNF/rGO.

The real part of impedance in the low frequency, Z' versus $\omega^{-1/2}$ yields a straight line with slope σ (Warburg coefficient) and the lithium ion diffusion coefficient can be calculated using Eq. (2.11) [88]. The linear plots of Z' versus $\omega^{-1/2}$ for all the samples are shown in Fig. 5.7(b). From the plots, we found the values of R_{ct} from intercepts and slope (σ) and the diffusion coefficient and other relevant parameters, which are summarized in the Table 5.2. LFS/CNF/rGO sample has higher diffusion coefficient (factor of 2) and lower charge transfer resistance compared to LFS/CNF. The lower charge transfer resistance and higher diffusion coefficient of LFS/CNF/rGO electrode, indicate better electron and lithium ion transport due to formation of 3D conducting network of CNF and rGO. We attribute the improved electrochemical performance of LFS/CNF/rGO, compared to LFS/CNF, to its enhanced electronic conductivity, high surface area, and factors described below.

Table 5.2 Electrochemical impedance parameters of the LFS/CNF and LFS/CNF/rGO nano-composites

Sample	R_{ct} **(Ω)**	σ **(Ω.s$^{1/2}$)**	D_{Li} **(cm^2 ·s^{-1})**	I_o **(mA· g^{-1})**	**Diffusion Length (nm)**
LFS/CNF	42.31	42.24	1.55×10^{-13}	60.7	84
LFS/CNF/rGO	39.16	30.21	3.03×10^{-13}	65.60	117

The improved electrochemical performances of the nanocomposites are due to the combined effect of the following factors. First, the nano-size of Li_2FeSiO_4 particles reduced the lithium ion diffusion path length, which provides the fast insertion/extraction of Li^+ ions. Second, good contact between Li_2FeSiO_4/C and rGO nanosheets and CNF gives low contact resistance and good adhesion between them, which provides the better stability and cyclability. In the nanocomposites studied in this work, perhaps a thin conducting carbon coating is formed with carbon from acetate salts used to synthesize Li_2FeSiO_4, CNF and rGO during solvothermal

treatment and high temperature annealing. This conducting coating over Li_2FeSiO_4 nanoparticles could further increase the conductivity of nanocomposites (~ 10^{-1} $S \cdot cm^{-1}$) by forming a 3D continuous conducting network between CNF and rGO in the cathode matrix, which facilitates the electron and lithium ion diffusion during charging and discharging process. In fact, Li_2FeSiO_4 nanoparticles prepared with without any carbon source shows an electrical conductivity ~ 5 x 10^{-5} $S \cdot cm^{-1}$, several orders of magnitude higher than the bulk Li_2FeSiO_4. It is interesting to note that although particle size and electronic conductivity are very similar for LFS/CNF and LFS/CNF/rGO composites, the latter exhibits enhanced electrochemical performance with higher exchange current density due to higher specific surface area providing good contact between the electrolyte and the cathode resulting in improved insertion/extraction of Li^+ during the charge/discharge cycles.

5.5 Conclusions

In summary, we have successfully synthesized the LFS/CNF and LFS/CNF/rGO composites by solvothermal method followed by calcination at 600 ^oC for 4 hours under continuous flow of argon gas. The LFS/CNF/rGO composite shows an initial discharge capacity of ~260 $mAh \cdot g^{-1}$ at C/20 rate, which is 78% of its theoretical capacity. Both the composite samples show improved rate capabilities at high rates and excellent stability at 1C for 200 cycles, with 90% retention of initial discharge capacity. The improved electrochemical performance of LFS/CNF/rGO is due to the fact that rGO and CNF form a 3D conducting network and having high surface area, which facilitates the kinetics of electron transport and Li^+ ion diffusion at nanoscale.

CHAPTER 6 SUMMARY AND FUTURE DIRECTION

Li_2FeSiO_4 has highly desirable properties as a cathode material for applications in lithium ion batteries: low cost (Iron and silicon ore are available in abundant in earth crest), high thermal and chemical stability (strong Si-O covalent bonding), non-toxic and environmental benignity, high cell voltage, high power density, and high theoretical specific capacity ~ 330 $mAh{\cdot}g^{-1}$ (possibility of two lithium ion intercalation per unit formula). These properties make it potential candidate for large scale applications. However, it suffers from low electronic conductivity and slow lithium diffusion. In this thesis, we developed the methods for increasing the electronic conductivity by various means, such as, carbon coating, metal doping and addition of carbon nanofibers (CNF) and reduced graphene oxide (rGO), which lead to enhanced electrochemical performance (specific capacity, rate capability, and stability). The results of the studies are summarized below.

In the first project, presented in Chapter 3, we demonstrated that electronic conductivity of Li_2FeSiO_4/C can be enhanced by several orders of magnitude higher than bulk Li_2FeSiO_4 by preparing the mesoporous Li_2FeSiO_4/C nanocomposites by two different synthesis methods (solgel, SG and solvothermal, ST) using P123 as a carbon source and structure directing agent. It was shown that heating of P123-Li_2FeSiO_4 at high temperature creates mesoporous structures and forms a uniform conducting carbon coating which facilitates the electron transport. The carbon coating also decreases the particle growth of Li_2FeSiO_4 during high temperature calcination, leading to nanoparticles with reduced lithium diffusion path length. The XRD and TEM results confirmed the formation of nanoparticles. The effect of annealing temperature on

particle growth and electrochemical properties showed the particle size increases with increasing annealing temperature leading to deterioration of electrochemical performance. The Li_2FeSiO_4/C-ST-600 ^oC nanocomposite sample exhibited a smaller average particle size, larger BET surface area and porosity and showed a discharge capacity of ~276 $mAh{\cdot}g^{-1}$ at C/30 rate, cycled between 1.5 and 4.6 V, with better stability and cyclability, compared to Li_2FeSiO_4/C-SG-600 ^oC which showed a discharge capacity of 235 $mAh{\cdot}g^{-1}$ at C/30 rate. We found that particle size, large surface area and large porosity are critical factors for improved electrochemical performance of Li_2FeSiO_4/C-ST-600 ^oC.

The second project involved a study of the effect of cation doping on the electrochemical properties of Li_2FeSiO_4. While carbon coating only increases the surface conductivity but not the lattice electronic conductivity, cation doping provides another effective approach to enhance the electronic conductivity resulting in improved electrochemical performance of the material. The effect of the Mg doping was investigated by preparing $Li_2Fe_{1-x}Mg_xSiO_4$/C (x=0, 0.1, 0.2, and 0.4) nano-composites by solvothermal method. We found the Mg doping in Li_2FeSiO_4 facilitates the synthesis of impurity free material with crystallite size increasing with increasing Mg concentration, as confirmed by XRD and TEM data. In spite of having the same amount of carbon in all the composites, the electronic conductivity increases with increasing doping concentration. We found that 1% Mg doped Li_2FeSiO_4/C with large surface area, small particle size, low charge transfer resistance and high lithium diffusion coefficient, showed the best electrochemical performance among all the composites and delivered a discharge capacity about ~278 $mAh{\cdot}g^{-1}$ at a rate of C/30 as well as better stability and cyclability compared to undoped Li_2FeSiO_4/C nano-composites prepared by the same method.

In the third project, presented in Chapter 5, we investigated the nanocomposites of Li_2FeSiO_4/CNF/rGO to explore their large surface area and high conductivity properties to enhance the electronic conductivity of the composites. Heating of polymers or surfactants at high temperatures to form in-situ carbon coating during synthesis of Li_2FeSiO_4 affects the morphology and has a higher chance of introducing impurities in the final product. The addition of highly conducting carbon nanotubes (CNTs), carbon nanofibers (CNFs), graphene, and reduced graphene oxide (rGO) during synthesis is an alternative method to enhance the electronic conductivity of composites without or less impurities formation. A comparative study of structural and electrochemical properties of Li_2FeSiO_4/CNF and Li_2FeSiO_4/CNF/rGO was undertaken, and the investigation shows that Li_2FeSiO_4/CNF/rGO has better discharge capacity, ~260 $mAh{\cdot}g^{-1}$ at C/20 rate (cycled between 1.5 to 4.6 V) compared to Li_2FeSiO_4/CNF. The improved performance of Li_2FeSiO_4/CNF/rGO is attributed to optimum surface area and conductivity due to 3D conducting network of CNF and rGO in the composite.

6.1 Future direction

Although, we successfully synthesized the nano-size Mg doped Li_2FeSiO_4/C with P123 as a carbon source with minor impurities and achieved ~84% of theoretical capacity Li_2FeSiO_4/C at low rate with improved rate capability and stability, we found that the carbon content in these composites to be ~15% by CHN analysis, which is somewhat a high amount of carbon in the cathode matrix. A high amount of carbon may block the pathway of electrolyte percolation and decrease the ionic conductivity. It will be interesting to synthesize Li_2FeSiO_4 with different carbon content and optimize the carbon content for the best electrochemical performance. The 1% Mg doped Li_2FeSiO_4/C showed the best electrochemical performance in our study. The role of Mg doping in Li_2FeSiO_4/C is not clear due to the presence of carbon. In order to further

investigate doping of effect, one can prepare the Mg doped Li_2FeSiO_4 using pure inorganic salts of lithium, iron, silicon and magnesium to avoid the residual carbon and analyze the XRD patterns (Rietveld refinement) to determine whether the Mg cations occupy either Li site, Fe site or both, and whether the unit cell expands or shrinks. The Hall measurement will be useful to determine the type of carriers (*n*-type or *p*-type), the carrier density, and the carrier mobility. It will be also be interesting to investigate the effect of doping of other cations (*i.e.* Nb, Zr, Cr, V, and Cd etc.) on the electrochemical performance of mesoporous Li_2FeSiO_4/C. In the third project, Li_2FeSiO_4/CNF/rGO showed improved electrochemical performance compared to Li_2FeSiO_4/CNF. We used the CNF and rGO ratio (1:1) with total carbon content of ~16%. It will be interesting to synthesize Li_2FeSiO_4 with reduced CNF and rGO content and optimize this ratio to achieve best electrochemical properties.

In this thesis, we have focused our work on Li_2FeSiO_4 of silicate family. It would be interesting to work on other transition metals such as manganese (Mn). The Li_2MnSiO_4 has attracted interest among the silicate family of cathodes because of its low cost and environmental friendliness and its higher cell voltage because of Mn^{2+}/ Mn^{3+} (4.2 V) couple rather than Fe^{2+}/Fe^{3+} (3.2 V) in Li_2FeSiO_4 [167, 168] and hence, can provide more power density. As Li_2MnSiO_4 also suffer from low electronic conductivity [169], we can use the same strategy of preparing Li_2MnSiO_4 by solvothermal method with P123 as surfactant as well cation doping to overcome this problem. Further, it would be interesting to partially substitute Fe^{2+} with Mn^{2+} in Li_2FeSiO_4; the substituted compound $Li_2Mn_xFe_{1-x}SiO_4$ could improve power density due to higher voltage of Mn^{2+}/Mn^{3+}.

As discussed in Chapter 1, morphology plays an important role in enhancing the electrochemical performance of Li_2FeSiO_4. J. Yang *et. al.* [81] synthesized Li_2FeSiO_4 nanorods

anchored on graphene using ascorbic acid and ethylene glycol by hydrothermal method and this composite delivered the discharge capacity of ~300 $mAh \cdot g^{-1}$ and improved stability and rate capability. D. Rangappa, *et. al.* [76] synthesized the nanosheets of Li_2FeSiO_4 by supercritical fluid method and achieved theoretical capacity at 45^o C at 0.02C rate for nanosheets of Li_2FeSiO_4 with MWCNT (5%) composite. It will be interesting to optimize the synthesize conditions to obtain nanosheets/nanorods of Li_2FeSiO_4 by hydrothermal/solvothermal method by changing the thermodynamic variables (i.e. reaction temperature, pH, and concentration of reactants) [9].

APPENDIX RIETVELD REFINEMENT PROCEDURE FOR GSAS

Availability of softwares and procedure

The GSAS can be downloaded from the following web links,

https://subversion.xray.aps.anl.gov/trac/EXPGUI/wiki/InstallWindows

http://www.ccp14.ac.uk/solution/gsas/

https://subversion.xray.aps.anl.gov/EXPGUI/trunk/doc/expgui.html

The Rietveld refinement examples, tutorials, and manual are also available on these web sites. Download the latest version of the software according to personal computer requirement (windows, Mac OS X, or Linux). After, then install on your computer with the option to save PC-GSAS and EXPGUI shortcut icons on desktop. To run the PC-GSAS, double click on its icon. You will see the following window. Click on setup-Expname-name the experiment name-open to save in any directory. Again click on setup-Expedt and follow the instructions on the screen as,

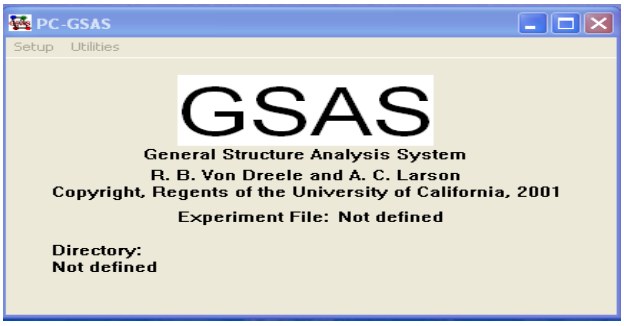

Do you wish to create it (Y/N)>Y, Enter

Enter the file name for this experiment>experiment name, Enter

EXPEDT data setup option < <?>, D, K, P, R, S, X> > X, Enter

Press any key to continue……, Enter

You will exit from the program.

Now double click on EXPGUI icon, you will see the following window

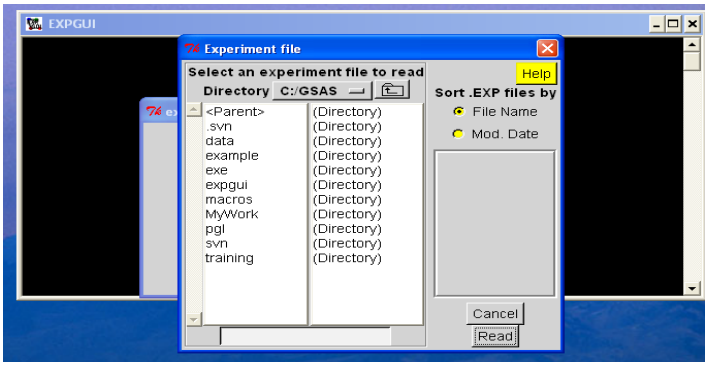

Now, go to directory where you saved the experiment name. Click the experiment name and click the read and it will take you to the following window.

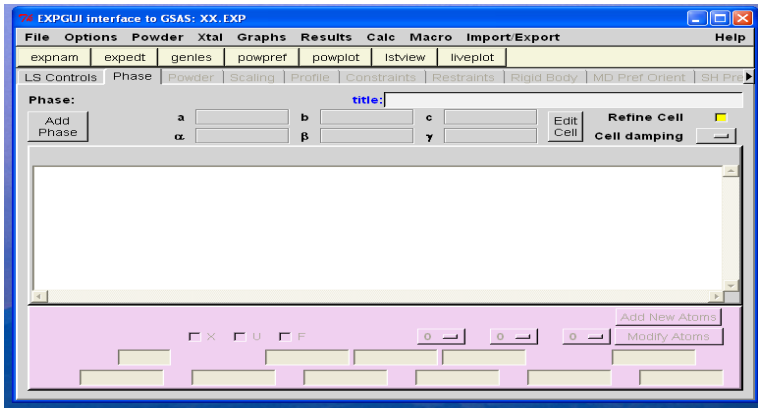

Now click add phase, go to import phase from, and use Crystallographic Information file (CIF). It will take you to the directory where you saved your experiment file. Now upload the CIF file for your powder X-ray data and follow the instructions as continue-continue-add atom. CIF contains the information about the lattice parameter and atomic position of crystal structure for any material. These files are available on following web sites;

https://icsd.fiz-karlsruhe.de/search/index.xhtml

http://serc.carleton.edu/research_education/crystallography/xldatabases.html

or lenience version of software available on ICSD website which could be downloaded on your personal computer.

The input file for GSAS

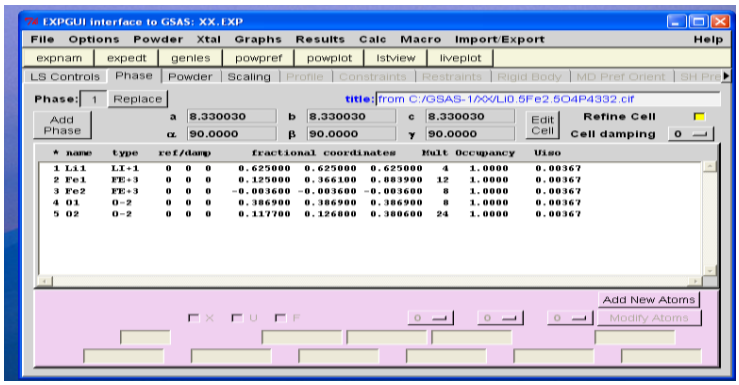

after uploading the CIF, go to powder and add new histrogram, you will get new window, showing to upload data file (x-ray data) and instrument parameter file (containing the information about the x-ray machine). First select file data and then select instrument parameter file and add these files. The GSAS EXPGUI accepts only GSAS format which can be converted by using different convertor softwares (ConvX and PowDLL Converter) free available on the following web sites.

http://www.ccp14.ac.uk/solution/powderdataconv/

http://www.ccp14.ac.uk/ccp/web-mirrors/convx/

To convert X-ray data file to GSAS format, first take your X-ray data in two colomn 2 theta and Intensity and save it ASCII format using notepad on your deginated directory and open any of convertor software and select your file and give the input file as ASCII 2theta, I format and outful file format as GSAS.

After adding the X-ray and instrument parameters files, you will see the folowing window.

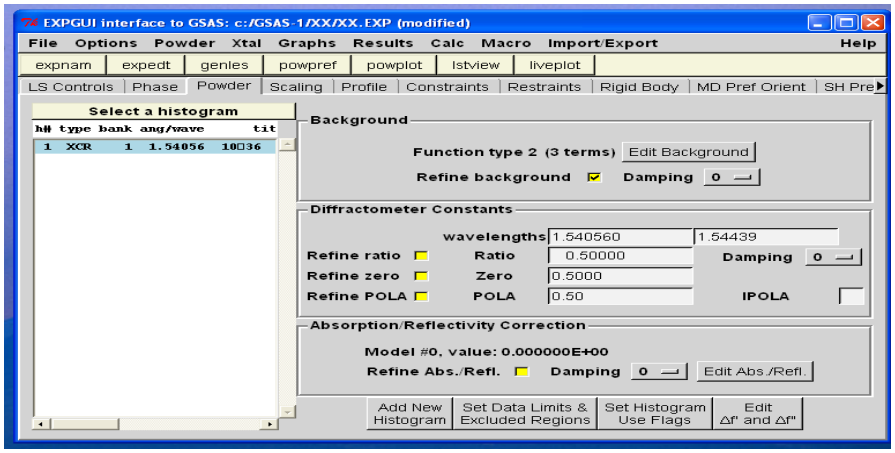

There are different functions to edit the background. Click on edit background and use the appropriate function and then click continue. Click on powpref in above window and press any key to continue and the action will modify the experiment file and asked for load new or continue with old. Click load new. Now click on genles and press any key to continue and load new.

Now click on liveplot to see the refinement graph having information about the observed X-ray pattern, calculated X-ray pattern, difference between them, background and Bragg's peak positions. Here is the image of the live plot,

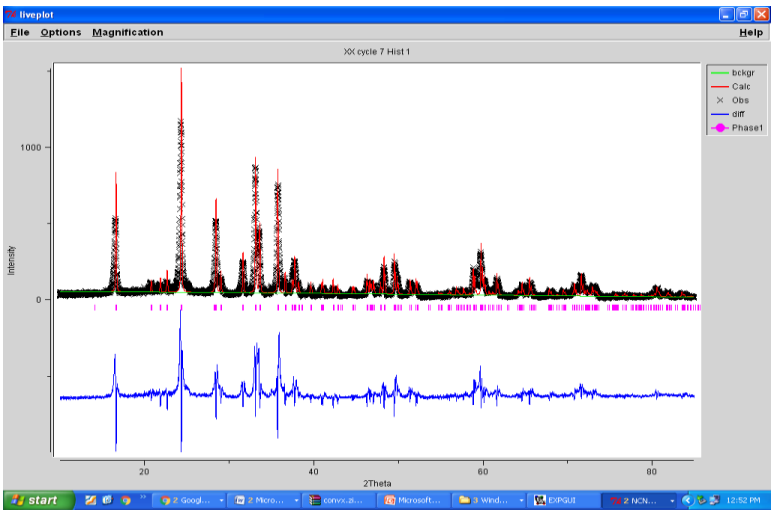

In order to further reduce the difference between the observed and calculated X-ray intensity, one have to optimize the profile, scaling, and phase parameters. The profile parameters can be changed by selecting one of GU, GV, GW, GP, LX, ptec, and shft etc using following window below and then click genles and minimize the reliability factors wR_p and R_p which determine the best fit of the X-ray data. These numbers may be decreased or increased, press any key to continue, if these numbers are decreased, use load new, if not use continue with old and use other parameters and repeat the process to get minimum wR_p and R_p values.

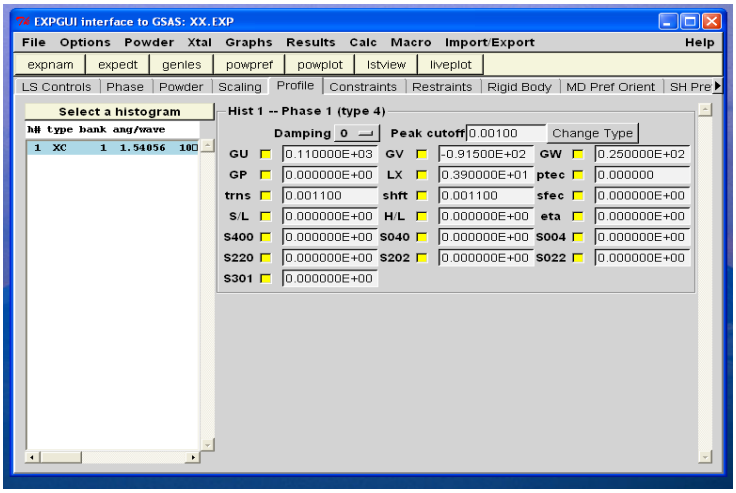

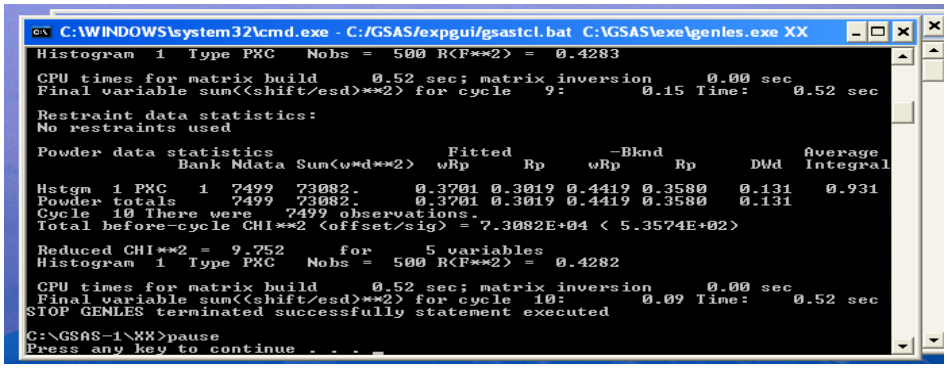

In the similar way, click phase and select the refine cell or any atom and select refine cell, X, U, F to optimize the lattice parameters, atom position (X), atomic displacement parameter (U), and atomic fraction (F) respectively and repeat the process (genles-press any key to continue,

load new/continue with old) to get the best fit for your X-ray data. In the same way click the scaling and select the phase 1 the refine and repeat the process (genles-press any key to continue, load new/continue with old)

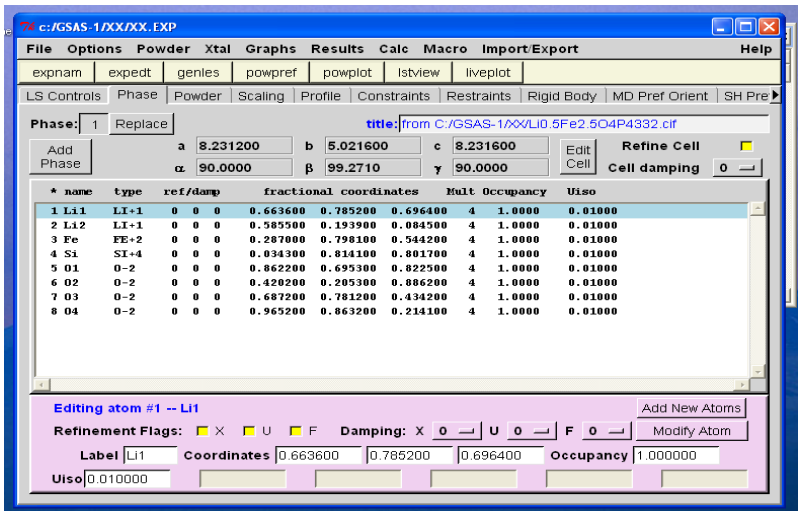

The more information about the functions and instructions are available on this website given below;

https://subversion.xray.aps.anl.gov/EXPGUI/trunk/doc/expgui.html.

REFERENCES

1. Xu, J., S. Dou, H. Liu, and L. Dai, Nano Energy, 2013. **2**(4): p. 439-442.
2. Goodenough, J.B. and K.-S. Park, J. Am. Chem. Soc., 2013. **135**(4): p. 1167-1176.
3. Scrosati, B. and J. Garche, J. Power Sources, 2010. **195**(9): p. 2419-2430.
4. Manthiram, A., J. Phys. Chem. Lett., 2011. **2**(3): p. 176-184.
5. Barghamadi, M., A. Kapoor, and C. Wen, J. Electrochem. Soc., 2013. **160**(8): p. A1256-A1263.
6. Wang, Y. and G. Cao, Adv. Mater., 2008. **20**(12): p. 2251-2269.
7. Tarascon, J.-M. and M. Armand, Nature, 2001. **414**(6861): p. 359-367.
8. Deng, D., Energy Sci. Eng., 2015. **3**(5): p. 385-418.
9. Gong, Z. and Y. Yang, Energy Environ. Sci., 2011. **4**(9): p. 3223-3242.
10. Doeff, M.M., *Battery cathodes*, in *Batteries for Sustainability*. 2013, Springer. p. 5-49.
11. Liu, R., J. Duay, and S.B. Lee, Chem. Commun., 2011. **47**(5): p. 1384-1404.
12. Ji, L., Z. Lin, M. Alcoutlabi, and X. Zhang, Energy Environ. Sci., 2011. **4**(8): p. 2682-2699.
13. Aydinol, M. and G. Ceder, J. Electrochem. Soc., 1997. **144**(11): p. 3832-3835.
14. Goodenough, J.B. and Y. Kim, Chem. Mater., 2009. **22**(3): p. 587-603.
15. Whittingham, M.S., Chem. Rev., 2004. **104**(10): p. 4271-4302.
16. Kim, W.-S. and W.-Y. Yoon, Electrochim. acta, 2004. **50**(2): p. 541-545.
17. Park, H.E., C.H. Hong, and W.Y. Yoon, J. Power Sources, 2008. **178**(2): p. 765-768.
18. Zhang, W.-J., J. Power Sources, 2011. **196**(1): p. 13-24.
19. Goriparti, S., E. Miele, F. De Angelis, E. Di Fabrizio, R.P. Zaccaria, and C. Capiglia, J. Power Sources, 2014. **257**: p. 421-443.
20. Theivanayagam, M.G. 2010.

21. Nytén, A. 2006, Acta Universitatis Upsaliensis.

22. Valøen, L.O. and J.N. Reimers, J. Electrochem. Soc., 2005. **152**(5): p. A882-A891.

23. Hu, M., X. Pang, and Z. Zhou, J. Power Sources, 2013. **237**: p. 229-242.

24. Li, Q., J. Chen, L. Fan, X. Kong, and Y. Lu, Green Energy & Environment, 2016. **1**(1): p. 18-42.

25. Galiński, M., A. Lewandowski, and I. Stępniak, Electrochim. Acta, 2006. **51**(26): p. 5567-5580.

26. Zheng, J., M. Tang, and Y.Y. Hu, Angew. Chem., 2016. **128**(40): p. 12726-12730.

27. Choi, J.-H., C.-H. Lee, J.-H. Yu, C.-H. Doh, and S.-M. Lee, J. Power Sources, 2015. **274**: p. 458-463.

28. Thackeray, M., J. Electrochem. Soc., 1995. **142**(8): p. 2558-2563.

29. Xu, B., D. Qian, Z. Wang, and Y.S. Meng, Mater. Sci. Eng., R, 2012. **73**(5): p. 51-65.

30. Meng, Y.S. and M.E. Arroyo-de Dompablo, Energy Environ. Sci., 2009. **2**(6): p. 589-609.

31. Kannan, A., L. Rabenberg, and A. Manthiram, Electrochem. Solid-State lett., 2003. **6**(1): p. A16-A18.

32. Manthiram, A., A.V. Murugan, A. Sarkar, and T. Muraliganth, Energy Environ. Sci., 2008. **1**(6): p. 621-638.

33. Nazri, G.-A. and G. Pistoia, *Lithium batteries: science and technology*. 2008: Springer Science & Business Media.

34. Ferg, E., R. Gummow, A. De Kock, and M. Thackeray, J. Electrochem. Soc., 1994. **141**(11): p. L147-L150.

35. Kim, D.K., P. Muralidharan, H.-W. Lee, R. Ruffo, Y. Yang, C.K. Chan, H. Peng, R.A. Huggins, and Y. Cui, Nano Lett., 2008. **8**(11): p. 3948-3952.

36. Goodenough, J.B., J. Solid State Electrochem., 2012. **16**(6): p. 2019-2029.

37. Goodenough, J.B., Acc. Chem. Res., 2012. **46(**5): p. 1053-1061.

38. Croguennec, L. and M.R. Palacin, J. Am. Chem. Soc., 2015. **137**(9): p. 3140-3156.

39. Vajeeston, P. and H. Fjellvåg, arXiv preprint arXiv:1611.04350, 2016.

40. Padhi, A.K., K. Nanjundaswamy, and J.B. Goodenough, J. Electrochem. Soc., 1997. **144**(4): p. 1188-1194.

41. Chung, S.-Y., J.T. Bloking, and Y.-M. Chiang, Nat. Mater., 2002. **1**(2): p. 123-128.

42. Andersson, A.S., J.O. Thomas, B. Kalska, and L. Häggström, Electrochem. Solid-State Lett., 2000. **3(**2): p. 66-68.

43. Arroyo-de Dompablo, M., M. Armand, J. Tarascon, and U. Amador, Electrochem. Commun., 2006. **8**(8): p. 1292-1298.

44. y de Dompablo, M.A., J. Gallardo-Amores, J. Garcia-Martinez, E. Moran, J.-M. Tarascon, and M. Armand, Solid State Ionics, 2008. **179**(27): p. 1758-1762.

45. Girish, H.-N. and G.-Q. Shao, RSC Adv., 2015. **5**(119): p. 98666-98686.

46. Bao, L., W. Gao, Y. Su, Z. Wang, N. Li, S. Chen, and F. Wu, Chin. Sci. Bull., 2013. **58**(6): p. 575-584.

47. Aravindan, V., K. Karthikeyan, K. Kang, W. Yoon, W. Kim, and Y. Lee, J. Mater. Chem., 2011. **21**(8): p. 2470-2475.

48. Nishimura, S.-i., S. Hayase, R. Kanno, M. Yashima, N. Nakayama, and A. Yamada, J. Am. Chem. Soc., 2008. **130**(40): p. 13212-13213.

49. Saracibar, A., A. Van der Ven, and M. Arroyo-de Dompablo, Chem. Mater., 2012. **24**(3): p. 495-503.

50. Park, M., X. Zhang, M. Chung, G.B. Less, and A.M. Sastry, J. Power Sources, 2010. **195**(24): p. 7904-7929.

51. Moskon, J., R. Dominko, R. Cerc-Korosec, M. Gaberscek, and J. Jamnik, J. Power Sources, 2007. **174**(2): p. 683-688.

52. Bazzi, K., B. Mandal, M. Nazri, V. Naik, V. Garg, A. Oliveira, P. Vaishnava, G. Nazri, and R. Naik, J. Power Sources, 2014. **265**: p. 67-74.

53. Wang, J. and X. Sun, Energy Environ. Sci., 2012. **5**(1): p. 5163-5185.

54. Gong, Z., Y. Li, G. He, J. Li, and Y. Yang, Electrochem. Solid-State Lett., 2008. **11**(5): p. A60-A63.

55. Guo, H.-J., K.-x. Xiang, C. Xuan, X.-h. Li, Z.-x. Wang, and L.-m. Li, T. Nonferr. Metal Soc., 2009. **19**(1): p. 166-169.

56. Armstrong, A.R., N. Kuganathan, M.S. Islam, and P.G. Bruce, J. Am. Chem. Soc., 2011. **133**(33): p. 13031-13035.

57. Yan, Z., S. Cai, X. Zhou, Y. Zhao, and L. Miao, J. Electrochem. Soc., 2012. **159**(6): p. A894-A898.

58. Nytén, A., M. Stjerndahl, H. Rensmo, H. Siegbahn, M. Armand, T. Gustafsson, K. Edström, and J.O. Thomas, J. Mater. Chem., 2006. **16**(34): p. 3483-3488.

59. Ensling, D., M. Stjerndahl, A. Nytén, T. Gustafsson, and J.O. Thomas, J. Mater. Chem., 2009. **19**(1): p. 82-88.

60. Wu, X., X. Jiang, Q. Huo, and Y. Zhang, Electrochim. Acta, 2012. **80**: p. 50-55.

61. Wu, X., X. Wang, and Y. Zhang, ACS Appl. Mater. Inter., 2013. **5**(7): p. 2510-2516.

62. Li, D., R. Xie, M. Tian, S. Ma, L. Gou, X. Fan, Y. Shi, and L. Hao, J. Mater. Chem. A, 2014. **2**(12): p. 4375-4383.

63. Hao, H., J. Zhang, X. Liu, T. Huang, and A. Yu, Int. J. Electrochem. Sci., 2013. **8**: p. 10976-10986.

64. Singh, S. and S. Mitra, Electrochim. Acta, 2014. **123**: p. 378-386.

65. Zhu, H., X. Wu, L. Zan, and Y. Zhang, ACS Appl. Mater. Inter., 2014. **6**(14): p. 11724-11733.

66. Devaraju, M., T. Tomai, and I. Honma, Electrochim. Acta, 2013. **109**: p. 75-81.

67. Li, M., L.-L. Zhang, X.-L. Yang, Y.-H. Huang, H.-B. Sun, S.-B. Ni, and H.-C. Tao, J. Solid State Electrochem., 2015. **19**(2): p. 415-421.

68. Deng, C., S. Zhang, B. Fu, S. Yang, and L. Ma, Mater. Chem. Phys., 2010. **120**(1): p. 14-17.

69. Dominko, R., D. Conte, D. Hanzel, M. Gaberscek, and J. Jamnik, J. Power Sources, 2008. **178**(2): p. 842-847.

70. Lv, D., W. Wen, X. Huang, J. Bai, J. Mi, S. Wu, and Y. Yang, J. Mater. Chem., 2011. **21**(26): p. 9506-9512.

71. Yang, J., X. Kang, L. Hu, X. Gong, and S. Mu, J. Mater. Chem. A, 2014. **2**(19): p. 6870-6878.

72. Zhou, H., F. Lou, P.E. Vullum, M.-A. Einarsrud, D. Chen, and F. Vullum-Bruer, Nanotechnology, 2013. **24**(43): p. 435703.

73. Peng, G., L.-L. Zhang, X.-L. Yang, S. Duan, G. Liang, and Y.-H. Huang, J. Alloys Compd., 2013. **570**: p. 1-6.

74. Zhang, Z., X. Liu, L. Wang, Y. Wu, H. Zhao, B. Chen, and W. Xiong, Electrochim. Acta, 2015. **168**: p. 8-15.

75. Zhao, Y., J. Li, N. Wang, C. Wu, Y. Ding, and L. Guan, J. Mater. Chem., 2012. **22**(36): p. 18797-18800.

76. Rangappa, D., K.D. Murukanahally, T. Tomai, A. Unemoto, and I. Honma, Nano Lett., 2012. **12**(3): p. 1146-1151.

77. Wang, K., W. Ren, J. Yang, R. Tan, Y. Liu, and F. Pan, RSC Adv., 2016. **6**(53): p. 47723-47729.

78. Yang, J., X. Kang, L. Hu, X. Gong, D. He, T. Peng, and S. Mu, J. Alloys Compd., 2013. **572**: p. 158-162.

79. Zhang, L.-L., S. Duan, X.-L. Yang, G. Peng, G. Liang, Y.-H. Huang, Y. Jiang, S.-B. Ni, and M. Li, ACS Appl. Mater. Inter., 2013. **5**(23): p. 12304-12309.

80. Zhang, Z., X. Liu, Y. Wu, and H. Zhao, J. Solid State Electrochem., 2015. **19**(2): p. 469-475.

81. Yang, J., L. Hu, J. Zheng, D. He, L. Tian, S. Mu, and F. Pan, J. Mater. Chem. A, 2015. **3**(18): p. 9601-9608.

82. Zhu, H., X. Wu, L. Zan, and Y. Zhang, Electrochim. Acta, 2014. **117**: p. 34-40.

83. Julien, C., A. Mauger, A. Vijh, and K. Zaghib, *Lithium batteries*, in *Lithium Batteries*. 2016, Springer. p. 29-68.

84. Wu, X.L., L.Y. Jiang, F.F. Cao, Y.G. Guo, and L.J. Wan, Adv. Mater., 2009. **21**(25-26): p. 2710-2714.

85. Dusastre, V., *Materials for sustainable energy: a collection of peer-reviewed research and review articles from Nature Publishing Group*. 2011: World Scientific.

86. Aricò, A.S., P. Bruce, B. Scrosati, J.-M. Tarascon, and W. Van Schalkwijk, Nat. Mater., 2005. **4**(5): p. 366-377.

87. Zhang, S., C. Deng, B. Fu, S. Yang, and L. Ma, J. Electroanal. Chem., 2010. **644**(2): p. 150-154.

88. Qu, L., D. Luo, S. Fang, Y. Liu, L. Yang, S.-i. Hirano, and C.-C. Yang, J. Power Sources, 2016. **307**: p. 69-76.

89. Qiu, H., H. Yue, T. Zhang, Y. Ju, Y. Zhang, Z. Guo, C. Wang, G. Chen, Y. Wei, and D. Zhang, Electrochim. Acta, 2016. **188**: p. 636-644.

90. Zhang, S., C. Deng, B. Fu, S. Yang, and L. Ma, Electrochim. Acta, 2010. **55**(28): p. 8482-8489.

91. Zhang, L.-L., S. Duan, X.-L. Yang, G. Liang, Y.-H. Huang, X.-Z. Cao, J. Yang, S.-B. Ni, and M. Li, Scientific reports, 2014. **4**.

92. Chen, R., R. Heinzmann, S. Mangold, V.K. Chakravadhanula, H. Hahn, and S. Indris, J. Phys. Chem. C, 2013. **117**(2): p. 884-893.

93. Guo, H., X. Cao, X. Li, L. Li, X. Li, Z. Wang, W. Peng, and Q. Li, Electrochim. Acta, 2010. **55**(27): p. 8036-8042.

94. Deng, C., S. Zhang, S. Yang, B. Fu, and L. Ma, J. Power Sources, 2011. **196**(1): p. 386-392.

95. Li, L.-m., H.-j. Guo, X.-h. Li, Z.-x. Wang, W.-j. Peng, K.-x. Xiang, and X. Cao, J. Power Sources, 2009. **189**(1): p. 45-50.

96. Hao, H., J. Wang, J. Liu, T. Huang, and A. Yu, J. Power Sources, 2012. **210**: p. 397-401.

97. Fergus, J.W., J. Power Sources, 2010. **195**(4): p. 939-954.

98. Nytén, A., A. Abouimrane, M. Armand, T. Gustafsson, and J.O. Thomas, Electrochem. Commun., 2005. **7**(2): p. 156-160.

99. Zaghib, K., A.A. Salah, N. Ravet, A. Mauger, F. Gendron, and C. Julien, J. Power Sources, 2006. **160**(2): p. 1381-1386.

100. Nytén, A., S. Kamali, L. Häggström, T. Gustafsson, and J.O. Thomas, J. Mater. Chem., 2006. **16**(23): p. 2266-2272.

101. Zheng, Z., Y. Wang, A. Zhang, T. Zhang, F. Cheng, Z. Tao, and J. Chen, J. Power Sources, 2012. **198**: p. 229-235.

102. Qu, L., S. Fang, L. Yang, and S.-i. Hirano, J. Power Sources, 2012. **217**: p. 243-247.

103. Xu, Y., W. Shen, A. Zhang, H. Liu, and Z. Ma, J. Mater. Chem. A, 2014. **2**(32): p. 12982-12990.

104. Zhang, M., Q. Chen, Z. Xi, Y. Hou, and Q. Chen, J. Mater. Sci., 2012. **47**(5): p. 2328-2332.

105. Yabuuchi, N., Y. Yamakawa, K. Yoshii, and S. Komaba, Dalton Transactions, 2011. **40**(9): p. 1846-1848.

106. Muraliganth, T., K. Stroukoff, and A. Manthiram, Chem. Mater., 2010. **22**(20): p. 5754-5761.

107. Peng, Z.D., Y.B. Cao, G.R. Hu, K. Du, X.G. Gao, and Z.W. Xiao, Chin. Chem. Lett., 2009. **20**(8): p. 1000-1004.

108. Shao, B. and I. Taniguchi, J. Power Sources, 2012. **199**: p. 278-286.

109. Dahbi, M., S. Urbonaite, and T. Gustafsson, J. Power Sources, 2012. **205**: p. 456-462.

110. Zhou, H., M.-A. Einarsrud, and F. Vullum-Bruer, Solid State Ionics, 2012. **225**: p. 585-589.

111. Ohring, M., *Materials science of thin films*. 2001: Academic press.

112. Suryanarayana, C. and M.G. Norton, *X-ray diffraction: a practical approach*. 2013: Springer Science & Business Media.

113. Cao, G., *Nanostructures and nanomaterials: synthesis, properties and applications*. 2004: World Scientific.

114. Kittel, C., *Introduction to Solid State Physics* 7th ed. 1966: John Wiley &Sons.

115. Cullity, B.D. and J.W. Weymouth, Am. J. Phys., 1957. **25**(6): p. 394-395.

116. Ståhl, K. 2008, Denmark. Technical University of Denmark.

117. Will, G., *Powder diffraction: The Rietveld method and the two stage method to determine and refine crystal structures from powder diffraction data*. 2006: Springer Science & Business Media.

118. van der PAUYV, L., Philips Res. Rep, 1958. **13**: p. 1-9.

119. Sing, K.S. and S. Gregg, Adsorption, Surface Area and Porosity, 1982.

120. Mudiyanselage, A.H. 2015, Wayne State University.

121. Dhindsa, K.S., B.P. Mandal, K. Bazzi, M. Lin, M. Nazri, G. Nazri, V. Naik, V. Garg, A. Oliveira, and P. Vaishnava, Solid State Ionics, 2013. **253**: p. 94-100.

122. Delmas, C., H. Cognac-Auradou, J. Cocciantelli, M. Menetrier, and J. Doumerc, Solid State Ionics, 1994. **69**(3-4): p. 257-264.

123. Guilmard, M., C. Pouillerie, L. Croguennec, and C. Delmas, Solid State Ionics, 2003. **160**(1): p. 39-50.

124. Dokko, K., Q. Shi, I.C. Stefan, and D.A. Scherson, J. Phys. Chem. B, 2003. **107**(46): p. 12549-12554.

125. Dudney, N.J., Electrochem. Soc. Interface, 2008. **17**(3): p. 44.

126. Macdonald, D.D., Electrochim. Acta, 2006. **51**(8): p. 1376-1388.

127. Pyun, S.-I., H.-C. Shin, J.-W. Lee, and J.-Y. Go, *Electrochemistry of insertion materials for hydrogen and lithium*. 2012: Springer Science & Business Media.

128. Hong, L. and Z. Zhang, Russ. J. Electrochem., 2013. **49**(4): p. 386-390.

129. Reddy, M., S. Madhavi, G.S. Rao, and B. Chowdari, J. Power Sources, 2006. **162**(2): p. 1312-1321.

130. Liu, S., J. Xu, D. Li, Y. Hu, X. Liu, and K. Xie, J. Power Sources, 2013. **232**: p. 258-263.

131. Wang, G., L. Yang, Y. Chen, J. Wang, S. Bewlay, and H. Liu, Electrochim. Acta, 2005. **50**(24): p. 4649-4654.

132. Zhu, Y. and C. Wang, J. Phys. Chem. C, 2010. **115**(3): p. 823-832.

133. Masquelier, C. and L. Croguennec, Chem. Rev., 2013. **113**(8): p. 6552-6591.

134. Dominko, R., M. Bele, A. Kokalj, M. Gaberscek, and J. Jamnik, J. Power Sources, 2007. **174**(2): p. 457-461.

135. Islam, M.S., R. Dominko, C. Masquelier, C. Sirisopanaporn, A.R. Armstrong, and P.G. Bruce, J. Mater. Chem., 2011. **21**(27): p. 9811-9818.

136. Dominko, R., M. Bele, M. Gaberšček, A. Meden, M. Remškar, and J. Jamnik, Electrochem. Commun., 2006. **8**(2): p. 217-222.

137. Gao, H.y., Z. Hu, J.g. Yang, and J. Chen, Energy Technology, 2014. **2**(4): p. 355-361.

138. Zhang, Z., X. Liu, L. Wang, Y. Wu, H. Zhao, and B. Chen, Solid State Ionics, 2015. **276**: p. 33-39.

139. Qiu, H., H. Yue, T. Zhang, Y. Ju, Y. Zhang, Z. Guo, C. Wang, G. Chen, Y. Wei, and D. Zhang, Electrochim. Acta, 2016. **188**: p. 636-644.

140. Zhang, S., C. Deng, and S. Yang, Electrochem. Solid-State Lett., 2009. **12**(7): p. A136-A139.

141. Du, X., H. Zhao, Y. Lu, C. Gao, Q. Xia, and Z. Zhang, Electrochim. Acta, 2016. **188**: p. 744-751.

142. Bruce, P.G., B. Scrosati, and J.M. Tarascon, Angew. Chem. Int. Ed., 2008. **47**(16): p. 2930-2946.

143. Okubo, M., E. Hosono, J. Kim, M. Enomoto, N. Kojima, T. Kudo, H. Zhou, and I. Honma, J. Am. Chem. Soc., 2007. **129**(23): p. 7444-7452.

144. Sirisopanaporn, C., C. Masquelier, P.G. Bruce, A.R. Armstrong, and R. Dominko, J. Am. Chem. Soc., 2010. **133**(5): p. 1263-1265.

145. Dominko, R., J. Power Sources, 2008. **184**(2): p. 462-468.

146. Saubanère, M., E. McCalla, J.-M. Tarascon, and M.-L. Doublet, Energy Environ. Sci., 2016. **9**(3): p. 984-991.

147. Seo, D.-H., J. Lee, A. Urban, R. Malik, S. Kang, and G. Ceder, Nat. Chem., 2016.

148. Sathiya, M., G. Rousse, K. Ramesha, C. Laisa, H. Vezin, M.T. Sougrati, M.-L. Doublet, D. Foix, D. Gonbeau, and W. Walker, Nat. Mater., 2013. **12**(9): p. 827-835.

149. Sathiya, M., J.-B. Leriche, E. Salager, D. Gourier, J.-M. Tarascon, and H. Vezin, Nat. commun., 2015. **6**.

150. Rouxel, J., Chem. Eur. J., 1996. **2**(9): p. 1053-1059.

151. Zhang, L.-L., H.-B. Sun, X.-L. Yang, Y.-W. Wen, Y.-H. Huang, M. Li, G. Peng, H.-C. Tao, S.-B. Ni, and G. Liang, Electrochim. Acta, 2015. **152**: p. 496-504.

152. Wang, B., B. Xu, T. Liu, P. Liu, C. Guo, S. Wang, Q. Wang, Z. Xiong, D. Wang, and X. Zhao, Nanoscale, 2014. **6**(2): p. 986-995.

153. Ni, J., Y. Zhao, J. Chen, L. Gao, and L. Lu, Electrochem. Commun., 2014. **44**: p. 4-7.

154. Yang, M.-R. and W.-H. Ke, J. Electrochem. Soc., 2008. **155**(10): p. A729-A732.

155. Meethong, N., Y.H. Kao, S.A. Speakman, and Y.M. Chiang, Adv. Funct. Mater., 2009. **19**(7): p. 1060-1070.

156. Huang, J., L. Yang, K. Liu, and Y. Tang, J. Power Sources, 2010. **195**(15): p. 5013-5018.

157. Sirisopanaporn, C., A. Boulineau, D. Hanzel, R. Dominko, B. Budic, A.R. Armstrong, P.G. Bruce, and C. Masquelier, Inorg. Chem., 2010. **49**(16): p. 7446-7451.

158. Jaén, J.A., J. Iglesias, A. Muñoz, J.A. Tabares, and G.A. Pérez Alcázar, Croat. Chem. Acta, 2015. **88**(4): p. 1-7.

159. Bard, A. and L. Faulker, 2001. **2nd Ed**.

160. Dhindsa, K., A. Kumar, G. Nazri, V. Naik, V. Garg, A. Oliveira, P. Vaishnava, Z. Zhou, and R. Naik, J. Solid State Electrochem., 2016. **20**(8): p. 2275-2282.

161. Dai, L., D.W. Chang, J.B. Baek, and W. Lu, small, 2012. **8**(8): p. 1130-1166.

162. Candelaria, S.L., Y. Shao, W. Zhou, X. Li, J. Xiao, J.-G. Zhang, Y. Wang, J. Liu, J. Li, and G. Cao, Nano Energy, 2012. **1**(2): p. 195-220.

163. Bonaccorso, F., L. Colombo, G. Yu, M. Stoller, V. Tozzini, A.C. Ferrari, R.S. Ruoff, and V. Pellegrini, Science, 2015. **347**(6217): p. 1246501.

164. Raccichini, R., A. Varzi, S. Passerini, and B. Scrosati, Nat. Mater., 2015. **14**(3): p. 271-279.

165. Kamat, P.V., J. Phys. Chem. Lett., 2011. **2**(3): p. 242-251.

166. Li, D., M.B. Müller, S. Gilje, R.B. Kaner, and G.G. Wallace, Nat. Nanotechnol., 2008. **3**(2): p. 101-105.

167. Belharouak, I., A. Abouimrane, and K. Amine, J. Phys. Chem. C, 2009. **113**(48): p. 20733-20737.

168. Aravindan, V., S. Ravi, W. Kim, S.-Y. Lee, and Y. Lee, J. Colloid Interface Sci., 2011. **355**(2): p. 472-477.

169. Aravindan, V., K. Karthikeyan, J. Lee, S. Madhavi, and Y. Lee, J. Phys. D: Appl. Phys., 2011. **44**(15): p. 152001.

ABSTRACT

NANOSTRUCTURED LITHIUM IRON SILICATE/CARBON COMPOSITES AS CATHODE MATERIAL FOR NEXT GENERATION OF LITHIUM-ION BATTERIES

by

AJAY KUMAR

August 2017

Advisor: Dr. Ratna Naik

Major: Physics (Condensed Matter)

Degree: Doctor of Philosophy

Lithium iron silicate (Li_2FeSiO_4) has the potential as cathode material for next generation lithium ion batteries because of its high specific theoretical capacity (330 mA h g^{-1}), low cost, environmental benignity, and improved safety. However, its intrinsically poor electronic conductivity and slow lithium ion diffusion in the solid phase limits its applications. To address these issues, we studied mesoporous Li_2FeSiO_4/C composites synthesized by sol-gel (SG) and solvothermal (ST) methods using tri-block copolymer (P123) as carbon source and structure directing agent. The Li_2FeSiO_4/C (ST) composites show improved electrochemical performance compared to Li_2FeSiO_4/C (SG). At C/30 rate, Li_2FeSiO_4/C (ST) delivered the discharge capacity ~276 mA h g^{-1} when cycled between 1.5-4.6 V and shows better rate capability and stability at high rates. We attribute the improved electrochemical performance of Li_2FeSiO_4/C (ST) to its large surface area and reduced particle size. We also synthesized Mg-doped $Li_2Mg_xFe_{1-x}SiO_4$/C, (x= 0.0, 0.01, 0.02, and 0.04) nano-composites by ST method to further improve their electrochemical performance. $Li_2Mg_{0.01}Fe_{0.99}SiO_4$/C nanocomposites exhibited the best rate capability and cycle stability (94% retention after 100 charge-discharge cycles at 1C) and also

delivered the highest initial discharge capacity of 278 mA h g^{-1} (~84% of the theoretical capacity) at C/30 rate, which is attributed to its enhanced Li-ion diffusion coefficient and lower charge transfer resistance due to reduced impurity phases, increased electronic conductivity, and maintaining large surface area.

Motivated by outstanding electronic and mechanical properties as well as high specific surface area of carbon nano-fibers (CNF) and reduced graphene oxide (rGO), we also investigated the ternary Li_2FeSiO_4/CNF/rGO nano-compositesas possible cathode materials which showed high stability over 200 cycles and improved discharge capacity at high C-rates.

AUTOBIOGRAPHICAL STATEMENT

EDUCATION

Ph.D., Physics, Wayne State University, USA, (2017)
M.Tech., Energy Studies, Indian Institute of Technology Delhi (2007)
M.Sc., Physics, Indian Institute of Technology Roorkee (2004)
B.Sc., (Physics, Mathematics, Chemistry), Chaudhary Charan Singh University Meerut (2002)

PROFESSIONAL EXPERIENCE

Project scientist, Amorphous Silicon Solar Cell Plant, BHEL, Gurgaon, India and IIT Delhi, India (Nov 2007 to April 2009)

ACADEMIC EXPERIENCES

Research Assistant, Department of Physics & Astronomy, Wayne State University, Detroit, MI, USA (June, 2015 to continue), Department of Mechanical and Materials Engineering, Florida International University, Miami, Florida, USA (Aug, 2010 to Dec, 2010)

Teaching Assistant, Department of Physics & Astronomy, Wayne State University, Detroit, MI,USA (Aug, 2011 to May, 2015), Department of Mechanical and Materials Engineering, Florida International University, Miami, Florida, USA (Jan, 2011 to July, 2011 & Aug, 2009 to July, 2010)

PUBLICATIONS

1. "Improved electrochemical properties of solvothermally synthesized Li_2FeSiO_4/C nano-composites: A comparison between solvothermal and sol-gel methods", **Ajay Kumar**, O.D. Jayakumar, Vaman M. Naik, G.A. Nazri, Ratna Naik, ***Solid State Ionics*** 294 (2016) 15–20.
2. " Enhanced electrochemical performance of $LiFePO_4$/C nanocomposites due to in-situ formation of Fe_2P impurities", K. S. Dhindsa, **A. Kumar**, G. A. Nazri, V. M. Naik, V. K. Garg, A. C. Oliveira, P. P. Vaishnava, Z. X. Zhou, R. Naik, ***J Solid State Electrochem*** (2016) 20: 2275.
3. "Ferroic ordering and charge-spin-lattice order coupling in Gd doped Fe_3O_4 nanoparticles relaxor multiferroic system", Suvra S. Laha, Ehab Abdelhamid, Maheshika P. Arachchige, **Ajay Kumar**, Ambesh Dixit, ***J American Ceramic Society,*** (2017)
4. "Mg doped Li_2FeSiO_4/C nano-composites synthesized by solvothermal method for lithium ion batteries", **Ajay Kumar**, O.D. Jayakumar, Vaman M. Naik, G.A. Nazri, Ratna Naik, (**Manuscript is submitted to Dalton Transactions**)

NATIONAL CONFERENCES

1. Poster presentation at **MRS** fall meeting, Boston, USA, Nov. 29-Dec. 3, 2010.
2. Oral presentation at **APS** March meeting, Baltimore, MD, USA, Mar. 18-Mar. 22, 2013
3. Oral presentation at **APS** March meeting, Denver, Colorado, USA, Mar. 3-Mar-7, 2014
4. Poster presentation at **APS** March meeting, San Antonio, TX, USA, Mar. 2- Mar. 6, 2015
5. Oral presentation at **APS** March meeting, Baltimore, MD, USA, Mar. 14-Mar. 18, 2016
6. Poster presentation at **APS** March meeting, New Orleans, LA, USA, Mar. 13-Mar. 17, 2017